University of Southampton

Faculty of Engineering and Physical Sciences

School of Chemistry

Organic Inorganic Hybrid Thermoelectric Materials for Energy Harvesting Applications

by

Syed Zulfiqar Hussain Shah

ORCID ID [https://orcid.org/0009-0003-4644-8038]

Thesis for the degree of Doctor of Philosophy

December 2024

University of Southampton

Abstract

Faculty of Engineering and Physical Sciences

School of Chemistry

Doctor of Philosophy

Organic Inorganic Hybrid Thermoelectric Materials for Energy Harvesting Applications

by

Syed Zulfiqar Hussain Shah

Organic-inorganic hybrid thermoelectric composites have emerged as promising candidates for flexible thermoelectric devices due to their low cost, solution processability, and ease of large-scale fabrication. Nevertheless, hybrid composite materials have been scarcely used primarily due to the unavailability of robust, high-performance materials. Therefore, it is essential to develop new materials with attributes such as elevated carrier mobility, electrical conductivity, Seebeck coefficients, and low thermal conductivity.

This dissertation primarily describes to develop organic-inorganic hybrid thermoelectric composites, predominantly composed of tellurium nanowires (TeNWs) and the conducting polymer poly(3-hexylthiophene-2,5-diyl) (P3HT), thereby improving thermoelectric (TE) performance by manipulating charge transport at the interfaces between nanowires and P3HT. Various strategies such as oxidation control, doping, surface modification, extending the dimensions of nanowires, and utilizing high molecular weight polymers are presented in this dissertation to enhancing TE performance of these hybrid composites. Aqueous solution chemical (ASS) method was developed to synthesize TeNWs. TeNWs and tellurium oxide (TeO_2) nanowires were combined with P3HT to fabricate two hybrid composite systems, and dispersions were drop-casted on quartz substrates. Hybrid films were doped in $FeCl_3$-acetonitrile solution to investigate the doping level. A significant improvement was observed in the power factor (65 μW/m·K²) of the oxidation-controlled P3HT-TeNWs hybrid composites compared to TeO_2NW-P3HT (PF ~ 15 μW/mK²) at room temperature with an optimum doping of 0.06M and 0.03M, respectively (Chapter 3). We then modified the surface of TeNWs with sulfide linkers and encapsulated the synthesized S^{2-}-TeNWs in P3HT to fabricate hybrid composite materials. Intriguingly, the S^{2-}-TeNWs-P3HT hybrid composites demonstrated improved TE performance, with an electrical conductivity (σ) of 35 S/cm, a Seebeck coefficient (S) of 150 μV/K, resulting a PF of about 78 μW/m-K² at room temperature (Chapter 4). Finally, we scaled up ASS process to synthesize long TeNWs (~ 13 μm) and embedded them into P3HT with varying molecular weights (50-70 kDa and 80-143 kDa) to create hybrid composite systems (Chapter 5). The hybrid composite Te-P3HT (80-143 kDa) exhibited a significant improvement in PF of 303 ± 38 μW/mK², with σ of 91 S/cm, S of 183 μV/K, and a thermal conductivity (κ) of 0.25 W/m-K, leading to a ZT value of 0.36 ± 0.06 with an optimum doping of 0.02M $FeCl_3$. Theoretical modelling has confirmed the strong templating of P3HT on the TeNWs surface. This templating enhances the charge carrier concentration, leading to increased σ. Whilst the charge transport induces de-doping at interface, resulting in high S. Both σ and S collectively contributes to improve power factors of composite hybrid materials.

Disruptions to research because of COVID-19

This project was conducted during the COVID-19 pandemic lockdown, which caused some disruption in its progress. The PhD program was a joint effort between the University of Southampton and the Institute of Materials Research and Engineering (IMRE) at the Agency for Science, Technology and Research (A*STAR) in Singapore. In the first year, the work was planned to take place at Southampton, but due to restrictions, lab capacity was limited to 50%, and new students could not receive training on various experimental tools. As a result, progress was slow. However, significant efforts were made to design and optimize synthesis methods for nanostructure materials, including hybrid thermoelectric composites. With the help of senior colleagues who had access to other research labs of university, some thermoelectric transport properties and materials characterizations were completed.

The project was then scheduled to continue at IMRE in Singapore, where strict COVID-19 measures were in place. These measures required extensive paperwork and multiple processes to enter in Singapore and to get in IMRE, causing a delay of about 3 to 4 months in a row. Despite these challenges, the training on different state-of-the-art tools at IMRE was incredibly valuable. As a result, the project advanced quickly over the last 18 months, leading to significant experimental work being completed at IMRE before returning to the UK for the final year.

Table of Contents

Table of Tables

Table of Figures

Table of Figures

List of Accompanying Materials

Journal Articles

1. **Syed Zulfiqar Hussain Shah** *et al*. "Oxidation control to augment interfacial charge transport in Te-P3HT hybrid materials for High thermoelectric performance." *Adv. Sci.* **2024**. DOI: 10.1002/ADVS.202400802

2. **Syed Zulfiqar Hussain Shah** *et al*. "Thermoelectric properties enhancement of tellurium nanowires by surface passivation." *ACS Appl. Mater. & Interfaces*, **2024**. DOI: 10.1021/acsami.4c02469

3. **Syed Zulfiqar Hussain Shah** *et al*. "Enhanced charge transport at the interfaces in P3HT-Tellurium Nanowires Hybrid Materials for high thermoelectric performance." **2024**. (To be submitted)

Conference Presentations

- Virtual Conference on Thermoelectric (VCT) – May 2021
- 7th International Conference on Multifunctional, Hybrid and Nanomaterials- Italy- Oct. 2022
- 11th International Conference on Materials for Advanced Technologies, IUMRS-ICAM-CMAT- Singapore – Jun. 2023.
- EPSRC Thermoelectric UK – Southampton - Nov. 2023.

Research Thesis: Declaration of Authorship

Print name: Syed Zulfiqar Hussain Shah

Title of thesis: Organic Inorganic Hybrid Thermoelectric Materials for Energy Harvesting Applications

I declare that this thesis and the work presented in it are my own and has been generated by me as the result of my own original research.

I confirm that:

1. This work was done wholly or mainly while in candidature for a research degree at this University, and Institute of Materials Research and Engineering (IMRE), Agency for Science, Technology and Research (A*STAR) Singapore.
2. Where any part of this thesis has previously been submitted for a degree or any other qualification at this University or any other institution, this has been clearly stated.
3. Where I have consulted the published work of others, this is always clearly attributed.
4. Where I have quoted from the work of others, the source is always given. With the exception of such quotations, this thesis is entirely my own work.
5. I have acknowledged all main sources of help.
6. Where the thesis is based on work done by myself jointly with others, I have made clear exactly what was done by others and what I have contributed myself.
7. Parts of this work have been published as: -

   (A) "Oxidation control to augment interfacial charge transport in Te-P3HT hybrid materials for High thermoelectric performance" **Syed Zulfiqar Hussain Shah**, Ding Zhenyu, Zainul Aabdin, Weng Weei Tjiu, Jose Recatala-Gomez, Haiwen Dai, Yang Xiaoping**,** Repaka Durga Venkata Maheswar, Wu Gang, Kedar Hippalgaonkar, Pawan Kumar, Iris Nandhakumar, *Adv. Sci.* **2024**. DOI: 10.1002/ADVS.202400802.

   (B) "Thermoelectric properties enhancement of tellurium nanowires by surface passivation" **Syed Zulfiqar Hussain Shah**, Zainul Aabdin, Weng Weei Tjiu, Nong Wei, Jose Recatala-Gomez, Chellappan Vijila, Zhai Wenhao, Repaka Durga Venkata Maheswar, Wu Gang, Kedar Hippalgaonkar, Pawan Kumar, Iris Nandhakumar, *ACS Appl. Mater. & Interfaces*, **2024**. DOI: 10.1021/acsami.4c02469.

Signature: ..... Date: 24/09/2024

Acknowledgements

First and foremost, I would like to express my deepest gratitude to my supervisor, Dr. Iris Nandhakumar at the University of Southampton United Kingdom, and my advisors Dr. Kedar Hippalgaonkar, and Dr. Pawan Kumar at the Institute of Materials Research and Engineering (IMRE), Agency for Science, Technology and Research (A*STAR) Singapore, for their unwavering support, guidance, and patience throughout my PhD journey. Your expertise and insightful feedback have been invaluable, and your encouragement has been a constant source of motivation.

I am deeply grateful to the Department of Chemistry at Southampton University, where I spent the first and final years of my studies. The supportive environment in Chemistry Lab provided by Dr. Samuel Perry, Dr. Maria de Lourdes Gonzalez-Juarez, Dr. Aran Amin, and Dr. Joshua White have greatly contributed to smooth running of Lab work.

I would also like to extend my heartfelt thanks to the Institute of Materials Research and Engineering (IMRE), A*STAR, Singapore, where I spent the second and third years of my research. The access to state-of-the-art facilities and the collaborative atmosphere there played a crucial role in advancing my work. I am especially thankful to my colleagues at IMRE, A*STAR Singapore: Dr. Zainul Aabdin and Dr. Weng Weei Tjiu for their work with TEM, STEM, and EELS; Dr. Jose Recatala-Gomez for performing XPS and SEM; Dr. Haiwen Dai for preparing FIB samples for cross-sectional analysis; Dr. Repaka Durga Venkata Maheswar for conducting XRD and helping with ZEM3 measurements; and Dr. Vijila Chellappan for Raman spectroscopy. Your camaraderie, insightful discussions, and unwavering support made the challenging moments of this journey much more manageable and enjoyable.

I owe a huge debt of gratitude to my family and friends for their unconditional love, support, and belief in me. To my beloved wife, thank you for your endless patience, understanding, and encouragement during the challenging moments. Your presence in my life has been a source of strength and joy.

I would like to acknowledge the financial support provided by A*STAR Graduate Academy's ARAP programme for my research studies in IMRE, A*STAR Singapore and the Engineering and Physical Sciences Research Council (EPSRC) UK, which made this research possible.

To all those who have contributed to this thesis, directly or indirectly, I offer my deepest thanks.

Definitions and Abbreviations

TE.....Thermoelectric

TEG .....Thermoelectric generator

FTEG .....Flexible Thermoelectric generator

S.....Seebeck coefficient

ΔV .....Voltage difference

ΔT .....Temperature gradient

σ .....Electrical conductivity

κ.....Thermal conductivity

κ_l .....Lattice thermal conductivity.

κ_e .....Electrical thermal conductivity

PF.....Power factor

ZT.....Figure of merit

CHB.....Chlorobenzene

$CHCl_3$ .....Chloroform

ACN .....Acetonitrile

$FeCl_3$ .....Iron tri-chloride

CSA .....Camphor-sulfonic acid

TeNWs.....Tellurium nanowires

CB .....Conduction band

VB .....Valance band

WF .....Work Function

$E_{barrier}$ .....Interfacial potential barrier

HOMO .....Highest occupied molecular orbital

LUMO .....Lowest unoccupied molecular orbital

CNTs .....Carbon nanotubes

CP .....Conducting Polymer

P3HT..... Poly (3 hexylthiophene)

PANI ..... Polyaniline

PPy ..... Polypyrrole

PEDOT Poly-3,4-ethylene-dioxy-thiophene

PSS ..... Polystyrene sulfonate

PESA ..... Photoelectron Emission Spectroscopy in Air

UV-Vis ..... Ultraviolet Visible Spectroscopy

XPS ..... X-ray Photoelectron Spectroscopy

XRD ..... X-ray diffraction

EDS..... Energy Dispersive X-rays Spectroscopy

SEM ..... Scanning Electron Microscopy

STEM ..... Scanning Transmission Electron Microscopy

EELS..... Electron Energy Loss Spectroscopy

DF..... Dark Field

BF ..... Bright Field

Chapter 1 Introduction

1.1 Aims, Objectives and Project Motivations

The main aim of this project was to fabricate a new generation of organic-inorganic hybrid composite materials by combining low-dimensional (1D) nanowires and integrating them into conducting polymers and then to adopt different strategies to enhance their thermoelectric (TE) properties.

The specific objectives to reach this aim were, to develop and optimise a procedure for synthesizing Tellurium (Te) nanostructures. Once that was achieved the next stage was to optimise the integration of these nanowires with conducting polymers using a solution mixing process and then to produce uniform composite films. Fabricated films would be utilised to investigate how the thermoelectric properties of the films change with different nanowire-to-polymer weight ratios, identifying the optimal compositions. To improve the TE performance of composites and investigating the charge transport mechanism at the interfaces of organic-inorganic materials, we would first employ oxidation-control strategy during the synthesis of Te nanowires and composite fabrication by conducting all processes under nitrogen environment. To minimize air-exposure, thin film samples would be sealed in air-tight membrane boxes and transferred to a dry box with a dehumidifier before any characterisation. Doping of the composite films would be carried out inside the nitrogen filled glovebox, with O_2 <1ppm, and H_2O <1ppm. The TE properties of the hybrid composites will then be measured.

To further enhance TE performance of composites and address incompatibility issues between the organic and inorganic components, we would adopt a surface passivation strategy. This will involve modifying the surface of TeNWs using a sulfur linker through solution mixing process. The surface-modified nanowires will be used to fabricate hybrid composites, allowing us to investigate how sulfur passivation affects charge transportation and TE properties.

Lastly, to explore the uncleared role of nanowires dimension (length, diameter, aspect ratio) in composites materials, we will scale-up the synthesis process to grow longer nanowires and incorporate them into a conducting polymer to study the TE performance of the hybrid composite materials. Additionally, we will encapsulate TeNWs with higher molecular weight polymers to fabricate nanocomposites and explore their charge transport mechanisms and TE performance. None of the aforementioned strategies have been previously reported in the literature. These approaches will be employed in this project and evaluated to determine if they effectively achieve the project's objectives.

1.2 Project Motivations

Over the past two decades, increasing concerns about CO_2 emissions, global warming, and energy supply have driven a focus on alternative, clean power generation methods. The UK Climate Change Act (2008) mandates an 80% reduction in CO_2 emissions by 2050.[1] Recent estimates suggest that around 37% of greenhouse gas (GHG) emissions stem from the power generation sector, with an additional 17% from manufacturing industries. Machines, ranging from jet engines to microprocessors, generate heat, as do various manufacturing processes, including those in steel and food production.[2] Technology capable of recapturing this wasted heat could be crucial in tackling the energy crisis and mitigating global warming and climate change.

Conventional methods to convert heat energy typically use rotating 'Rankine cycle' machinery (e.g., pumps or turbines), which can be challenging to scale efficiently and require maintenance. In contrast, thermoelectric generators (TEGs) are solid-state devices that have ability to interconvert heat and electricity without moving parts, offering a simple, compact solution for power generation.

Recently, there has been increasing interest in eco-friendly, stable, and long-lasting self-powered wearable and medical implantable devices. This growing demand has led to significant attention on flexible thermoelectric materials and devices (FTEGs). In this concern, polymer-based thermoelectric materials are particularly appealing due to their natural flexibility, affordability, low toxicity, easy synthesis, environmental friendliness, stability, solution processability, and promising TE performance.[3] These properties make them ideal for FTEGs, which can be used in a wide range of practical applications, such as charging low-power wearable and portable electronics.[4] The rising need for lightweight, high-performance, and cost-effective products is driving the global conductive polymer market, which was valued at $3.46 billion in 2020 and is projected to reach $5.76 billion by 2027, with an annual growth rate of 8.3%.[5] Conducting polymers are widely used in combination with inorganic materials to fabricate organic-inorganic hybrid composites. These composites offer unique properties, such as improved mechanical strength, durability, high energy conversion efficiency, substantial power output, and stability at relatively high temperatures.[3,6] They play an important role in applications such as wearable and implantable flexible electronics, efficient heat management, and bioelectronics.[7,8,9]

However, the organic-inorganic hybrid TE materials have been scarcely used primarily due to the unavailability of robust high- performance materials, and hence there exist very few reports in the literature on hybrid composite materials. As depicted in Figure 1.1, organic-inorganic hybrid composite thermoelectric materials publications over time (2014 – 2024) has been analysed

through web of science, the highest index of 17 publications in year 2021 were found in different areas of research disciplines.

Figure 1.1. An analysis via web of science indicating the publications for organic-inorganic hybrid composite TE materials over time (2014-2024) in different areas of research disciplines.

Therefore, the key challenge is to develop high performing organic-inorganic TE materials that can provide high power output for flexible thermoelectric generators. In this context, the main materials planned for use in fabricating organic-inorganic hybrid composites in this project are tellurium and the conducting polymer P3HT, as they demonstrate high thermoelectric properties at room temperature and have significant potential for future FTEG applications.

1.3 Theory of Thermoelectrics

1.3.1 Discovery of Thermoelectric Devices

In 1821, Thomas Seebeck observed that when two dissimilar materials are in contact at different points and a temperature gradient is applied across their junction, it generates an electromotive force within the circuit connecting the two materials. This phenomenon is known as the thermoelectric effect or Seebeck effect. Conversely, in 1834, Peltier discovered the inverse of the Seebeck effect, wherein the flow of current through the junction of different materials could either absorb or release heat at that junction depending on the direction of the current flow. This phenomenon is referred to as the Peltier effect.[10] A thermoelectric device or thermoelectric generator (TEG), is a solid-state device that can convert heat into electricity and vice versa using the Seebeck and Peltier effects. It primarily consists of multiple thermoelectric pairs, each made up of a p-type semiconductor and an n-type semiconductor, which are connected in series to form a thermoelectric couple. Figure 1.2 shows the configuration of the n-type and p-type legs in a basic thermoelectric device, illustrating how it can be used for both power generation and cooling.

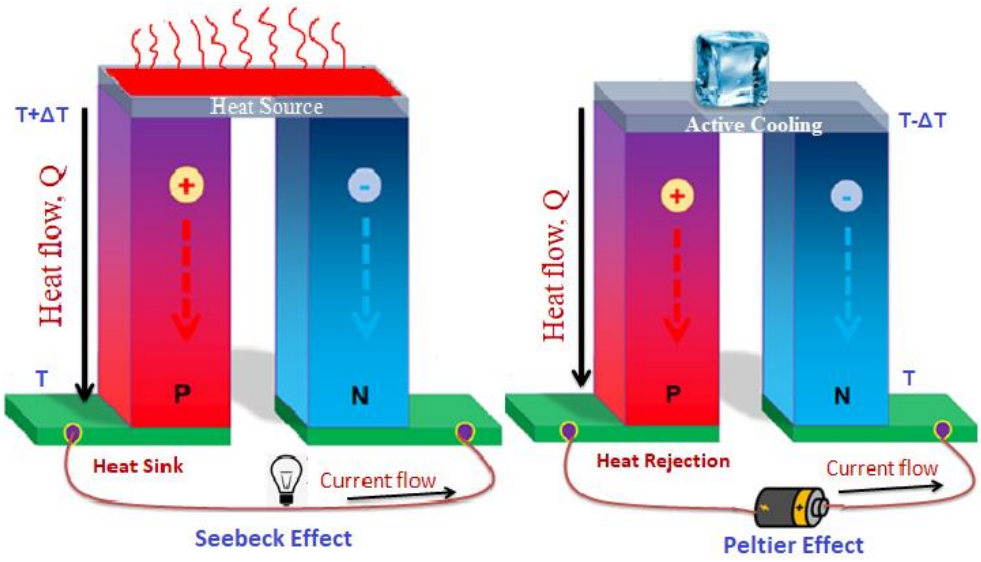

Figure 1.2. A simple TEG device showing p-type and n-type semiconductors connected in series and illustrating the Seebeck effect and Peltier effects.[11]

When there is a temperature difference across a thermoelectric couple connected to a circuit, the charge carriers (electrons and holes) move from the hot side to the cold side, generating a potential difference (ΔV) and electrical current. This is known as the Seebeck effect, which is how a TEG generates power. On the other hand, when a current is applied to the TEG, it creates a temperature difference, causing one side to absorb heat and the other to release it. This is known as the Peltier effect, which is used for cooling.[12]

1.3.2 Thermoelectric Properties

In 1911, Altenkirch derived the thermoelectric figure of merit (ZT) to assess the performance of TEG.[13,14] The mathematical expression for ZT is as follows:

$$ZT = \frac{S^2 \sigma T}{\kappa} \qquad \textit{Equation 1}$$

Here, S is the Seebeck coefficient (V/K), σ is the electrical conductivity (S/m), T is the absolute temperature (K), and κ is the thermal conductivity (W m^{-1} K^{-1}) of the thermoelectric (TE) materials that make up the TEG.

The ability of a TE material to generate a potential when applying a temperature gradient is known as Seebeck coefficient (S) or thermopower. Stated differently, the Seebeck coefficient quantifies the open circuit voltage across TE materials under the influence of a temperature gradient, and is mathematically written as:

$$V_{OC} = -S\Delta T \qquad \textit{Equation 2}$$

Where, ΔT is the temperature difference and V_{OC} is the open circuit voltage. In a scientific context, the Seebeck coefficient for a p-type material can be elucidated as follows: When a temperature gradient is imposed across the p-type TE material, the positively charged carriers (holes) within the material migrate from the region of higher temperature to that of lower temperature. This migration generates a negative open circuit voltage, which acts to counteract the movement of the holes, effectively pulling them back towards the warmer end. As per equation 2, this results in positive values for the Seebeck coefficient of the p-type TE material. Analogously, a similar rationale applies to n-type TE materials, where the Seebeck coefficient is negative due to the opposite direction of carrier movement.

The product of the square of the Seebeck coefficient (S) and the electrical conductivity (σ) is often cited in the literature as the power factor (PF), and is computed as:

$$PF = S^2 \sigma \qquad \textit{Equation 3}$$

The magnitude of the power factor (μW m^{-1} K^{-2}) signifies the material's capability for energy harvesting. However, the overall efficiency (η) of a TEG is determined as:

$$\eta = \frac{\Delta T}{T_h} \cdot \frac{\sqrt{1+ZT}-1}{\sqrt{1+ZT}+\frac{T_c}{T_h}} \qquad \text{Equation 4}$$

Where T_h and T_c represent the temperatures at the hot and cold ends of the material, respectively. Like all heat engines, the maximum efficiency of a TEG for generating power is limited by the Carnot

efficiency, which is given by $\Delta T/T_h$ (where ΔT is the temperature difference between the hot and cold ends). Determining the overall efficiency of a TEG is challenging because it varies depending on the external temperature of the environment and the temperature difference (ΔT) at any given moment.[15]

In equation 1, thermal conductivity (κ) of a material is the sum of both electronic thermal conductivity κ_e and lattice thermal conductivity κ_l as shown in equation 5:

$$\kappa = \kappa_e + \kappa_l \qquad \text{Equation } 5$$

The electronic thermal conductivity (κ_e) comes from the movement of free charge carriers (like electrons) in the material, while the lattice thermal conductivity (κ_l) is due to vibrations within the lattice of the material. The variables S, σ, and κ, are referred to as thermoelectric transport properties of a TE material. Achieving optimal TE performance is a challenging endeavour due to the interrelationships between these transport parameters. The relationship between TE parameters are described by Wiedemann-Franz Law and the Mott's equation: [16]

$$S = \frac{8\pi^2 k_B^2}{3eh^2} m^* T \left(\frac{\pi}{3n}\right)^{2/3} \qquad \text{Equation 6}$$

$$\sigma = ne\mu \qquad \text{Equation 7}$$

$$k_e = L\sigma T \qquad \text{Equation 8}$$

Where κ_B is the Boltzmann constant, e is the electrical charge, h is the Planck's constant, m* is the carrier effective mass, n is the charge carrier concentration, μ is the carrier mobility, and L is the Lorentz number. According to equation 6, the Mott's relation shows that Seebeck coefficient is inversely proportional to the charge carrier concentration ($S \propto \frac{1}{n}$). Electrical conductivity (σ) depends on how many charge carriers (n) contribute to the electrical current along with their mobility (μ), as explained in equation 7. Finally, equation 8 presents the Wiedemann-Franz Law, which relates the electronic thermal conductivity (κ_e) to electrical conductivity, material's temperature (T), and the Lorentz factor for a material, which is typically 2.45×10^{-8} V^2K^{-2} for metals and 1.5×10^{-8} V^2K^{-2} for undoped semiconductors.[16] Consequently, to enhance ZT values, it is imperative to maintain a delicate balance between S, σ, and κ_e.[15,11,9] Figure 1.3 illustrates the correlation between transport parameters. The graph depicts the figure of merit (ZT) plotted against the carrier concentration of a TE material.

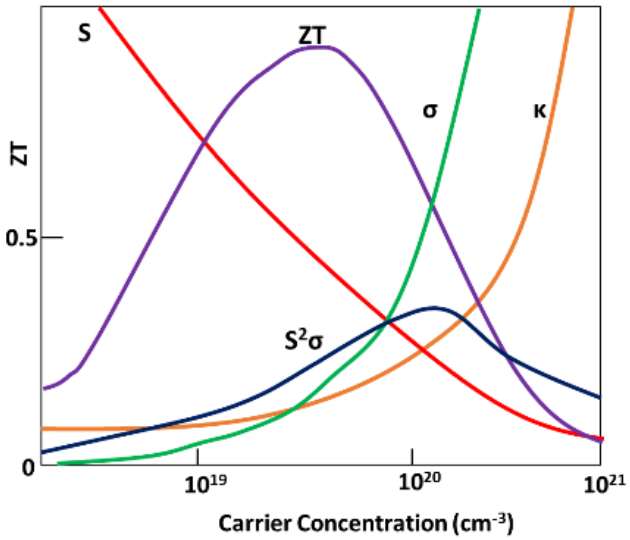

Figure 1.3. Relationship between the figure of merit and carrier concentration, incorporating data on Seebeck coefficient (S), electrical conductivity (σ), thermal conductivity (κ), power factor ($S^2\sigma$), and ZT values. Adopted from Elsheikh.[13]

As evidenced by the ZT versus carrier concentration plot, high charge carrier concentrations (10^{20} to 10^{21} carriers/cm^3) correspond to elevated electrical conductivity but diminished Seebeck coefficient, characteristic of metallic behaviour. Conversely, low charge carrier concentrations ($n < 10^{19}$) lead to decreased electrical conductivity but heigh Seebeck coefficient, resembling insulator properties. The peak in ZT occurs for heavily doped semiconductor materials with carrier concentration ranges of 10^{19} to 10^{20} (carriers/cm^3), where the material displays low thermal conductivity alongside elevated power-factor.

1.3.3 Flexible Thermoelectric Generators (FTEGs)

Current commercial TEGs face limitations in their applications due to their bulkiness, rigidity, and low efficiency.[17] This limits their use, especially when they need to be in contact with curved heat sources, which restricts their commercial applications in wearable electronics.[3] In contrast, flexible thermoelectric (FTE) materials and devices are promising because their ability to conform to curved surfaces allows for more effective heat harvesting. FTE materials can also be produced at much lower temperatures.[18] Compared to rigid devices, FTE devices are lightweight and can be easily attached to human skin, enabling the direct conversion of body heat into electricity without needing to recharge, while also minimizing heat loss during energy transfer.[19] These advantages make FTE devices a promising power source for wearable electronics. Figure 1.4 shows a typical FTE device, which consists of a substrate, TE legs, connecting electrodes, and bonding interfaces. In this FTE device, the substrate is both flexible and insulating, allowing the device to bend while ensuring that the carrier transport within the TE legs is not disrupted. The TE legs are designed as thin films

to maintain the flexibility of device. The electrodes connect the n-type and p-type TE legs in series, while the bonding interfaces help to stabilize the TE legs and electrodes.

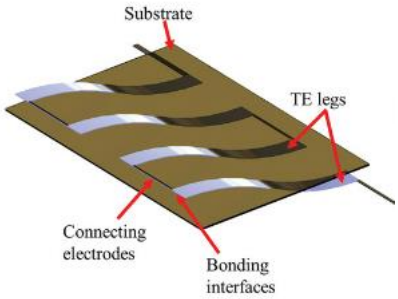

Figure 1.4. Schematic diagram of a typical module for FTE devices. Adopted from Ref.[3]

Table 1 . State-of-the-art high performing Flexible Thermoelectric devices, including those based on organic-inorganic composite materials. These devices demonstrate advancements in flexibility and thermoelectric efficiency for modern applications.

Types/Materials	ΔT (K)	Units (N)	Output Voltage (mV)	Output Power	Reference
(p) Sb_2Te_3/(n) Bi_2Te_3	20	50	171.6	10.5 µW	[20]
(p) Sb_2Te_3/(n) Bi_2Te_3	46.2	71	308.8	166 µW	[21]
(p) $Bi_{0.5}Sb_{1.5}Te_3$/(n) $Bi_{0.5}Te_{2.7}Se_{0.3}$	21.4	20	54.6	1700 µW	[17]
(p) Sb_2Te_3/(n) Bi_2Te_3	35	12	10	0.015 µW	[22]
(p) $Bi_{0.5}Sb_{1.5}Te_3$/(n) $Bi_2Te_{2.5}Se_{0.5}$	35	1	10.5	23 µW	[23]
(p) Bi_2Te_3/(n) Bi_2Te_3	50	52	37.2	0.18 µW	[24]
(p) Sb_2Te_3/(n) $Bi_2Te_{2.7}Se_{0.3}$	50	10	151	2.9 µW	[25]
(p) $Bi_{0.4}Sb_{1.6}Te_3$/(n) Ag_2Se	40	13	11.5	0.25 µW	[26]
(p) PANI/ (n) Ag_2Se	30	13	7.9	0.84 µW	[27]
(p) PEDOT: PSS	50	14	12	16.8 µW	[28]
(p) PEDOT: PSS/(n) Ni	65	144	260	46 µW	[29]
(p) PEDOT: PSS/CNT	10	14	4	36.3 nW	[30]
(p) Te-PEDOT: PSS/SWCNT	20	14	24	126 nW	[31]
(p) PEDOT: PSS-SWCNT/(n) PEI-SWCNT	50	6	28.2	220 nW	[32]
(p) P3HT/CNT	10	14	9.5	46 nW	[30]
(p) Te-PEDOT: PSS (H_2SO_4)	10	16	12.8	10.6 nW	[33]
(p) PEDOT: PSS/(n) fullerene-TiS_2	20	2	4.8	335 nW	[34]
(p) PEDOT: PSS/(n) $(PEDOT)_xV_2O_5$	20	4	14.5	0.34 nW	[35]

Nevertheless, FTEGs show low performance (see Table 1) therefore, current research on flexible thermoelectric generators (FTEGs) focuses on two main areas: developing high-performance FTE materials and designing high-output FTE devices. In terms of material development, one approach is to use conductive polymers, while another is to create organic-inorganic composite materials. Both approaches are detailed in the following sections.

1.4 State-of-the-art Conducting Polymers

Conducting polymers (CPs) constitute a distinctive class of polymers with the ability to conduct electricity. They feature an extended network of conjugated carbon–carbon double bonds, enabling the movement of charge carriers (electrons or holes) along their molecular chains (the charge transport mechanisms in CPs are discussed in Section 1.6). This arrangement of bond alternation results in the formation of a band gap, which is responsible for semiconducting properties in CPs.[7] Conducting polymers have garnered significant research interest for their potential applications in field-effect transistors,[36] gas sensors,[37] light-emitting diodes,[38] solar cells,[39] and thermoelectrics.[40] This interest stems from their controllable electrical and optical properties, solution processability, and exceptional mechanical flexibility,[41,42] which confer advantages over traditional inorganic semiconductors. In their undoped state, CPs typically function as insulators or semiconductors with a band gap exceeding 2 eV, resulting in limited electrical conductivity, typically ranging from 10^{-10} to 10^{-08} Scm^{-1} (e.g., polythiophene and polyacetylene). Achieving precise control over the electrical conductivity of CPs remains a challenge, largely influenced by factors such as carrier concentration and mobility. Nevertheless, CPs exhibit low thermal conductivity, typically falling within the range of 0.1-2 $Wm^{-1}K^{-1}$, which positions them as prime candidates for high-performance thermoelectric (TE) applications.[43]

Table 2 summarise the transport properties of some state-of-the-art conducting polymers, including polypyrrole (PPy),[44] polyaniline (PANI),[45] poly(3,4-ethylenedioxythiophene): polystyrene sulfonate (PEDOT: PSS),[46] and poly(3-hexylthiophene) (P3HT).[5] These CPs have strong potential for use in wearable FTEGs.

Table 2. A summary of the thermoelectric transport properties of conducting polymers.

Conducting Polymers	σ (S/cm)	S (μV/K)	PF (μW/m-K^2)	κ(W/m-K)	zT
PA [47]	11560	28.4	932	0.7	0.38
PANI [43]	7000	7	34.3	0.1 – 0.2	0.051
PPy [44]	100	12	1.44	0.1 – 0.2	0.002
PEDOT: PSS [48]	620	33.4	69.16	0.30	0.42
PEDOT: PSS [49]	1000	334.68	245.58	-	-
PEDOT: PSS (N_2H_5 treated) [50]	512.8	42.7	93.5	-	0.25
P3HT [F6TCNNQ doped] [51]	500	45	80	-	-
P3HT [$FeCl_3$ doped] [52]	128	85	20	-	-
P3HT [F4TCNNQ doped] [53]	160	60	56	-	-
P3HT [F4TCNNQ doped] [54]	22	60	3.0	-	-
P3HT [55]	320	269	62.4	-	0.1

To achieve the high TE performance of CPs, different strategies such as doping, pre- and post-treatments, and hybridization have been adopted. For instance, free-standing polypyrrole (PPy) films were created using an interfacial polymerization process and were doped with p-toluene sulfonic acid (PTSA) during synthesis. These films achieved a maximum power factor (PF) of about 0.42 μW/mK² at an optimal PTSA concentration of 0.45M.[44] Iodine-doped polyacetylene (PA) demonstrated a significant enhancement in electrical conductivity, reaching 11,560 S/cm, with a Seebeck coefficient of 28.4 μV/K. This resulted in a power factor (PF) of approximately 932 μW/mK² and a thermal conductivity of 0.7 W/m-K, leading to a figure of merit (zT) of 0.38 at room temperature. However, the material was found to be unstable when exposed to air.[47]

Among the various CPs, PEDOT is considered as the most suitable candidate for TE application due to its high electrical conductivity (~ 10^3 S/cm), commercial availability, flexibility, and excellent chemical and environmental stability. When doped with PSS, a solution processable polymer PEDOT:PSS has achieved a zT value of 0.42 at room temperature and has proven to be stable in air.[48] Combining PEDOT:PSS with another polymer, PANI-CSA (camphor-sulfonic acid), has been reported to enhance TE performance of the composite polymer. In this hybrid polymer, the increase

in electrical conductivity is attributed to the stretching of PEDOT layer due to the PANI-CSA chain and hole diffusion from the PANI-CSA to the PEDOT:PSS layer.[56]

In addition to PEDOT:PSS, P3HT is another widely studied polymer for thermoelectric applications due to its high intrinsic Seebeck coefficient and advantages such as solution processability, chemical stability, and thermal stability.[57] The electrical conductivity of P3HT can vary widely, from 10^{-8} to 10^{5} S/m, depending on the level of doping with appropriate dopants such as $HClO_4$, $FeCl_3$, or I_2.[58] For instance, P3HT doped in 1,3,4,5,7,8-hexafluoro-tetracyano -naphthoquinone dimethane (F6TCNNQ) has exhibited an electrical conductivity of 500 S/cm, a Seebeck coefficient of 45 µV/K, and a power factor of about 80 µW/mK² at room temperature.[51]

Although conductive polymers are promising for thermoelectric applications due to their low thermal conductivity, high electrical conductivity, ability to be shaped into various forms, and eco-friendly nature, their efficiency in converting heat to electricity is still limited. The reported values of the figure of merit (zT) for these CPs are not yet high enough for effective energy conversion. Therefore, it is crucial to find ways to further enhance the zT values using different approaches such as, embedding inorganic materials into CPs matrix to fabricate hybrid organic-inorganic composites, as detailed in following section.

1.5 Organic-inorganic Hybrid Composite Materials

To improve the thermoelectric performance of conducting polymers, combining them with inorganic thermoelectric (TE) materials has emerged as a promising approach. These hybrid composite materials often exhibit better TE properties than either component alone. A comprehensive literature review encompassing TE performance data of different organic-inorganic composite systems is detailed in Table 3, Section 3.1. Among various inorganic materials, tellurium (Te) has attracted significant attention as a promising p-type inorganic semiconductor. In bulk form, Te demonstrates strong p-type behaviour with a high Seebeck coefficient of 500 µV/K, electrical conductivity of 3.5 S/cm, thermal conductivity of 3.4 W/m-K, power factor of 86 µW/m-K², and a figure of merit (zT) of 0.008 at room temperature.[59] Tellurium (Te) has a trigonal crystal structure composed of chiral spiral chains of bonded atoms. These chains are held together by van der Waals forces, as shown in Figure 1.5.

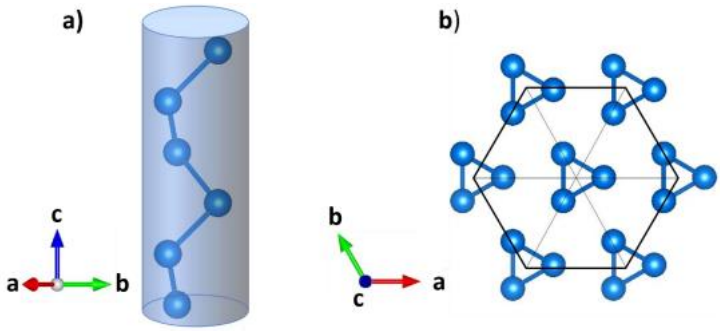

Figure 1.5. Crystal structure of tellurium. (a) Helical chains forming the one-dimensional building blocks of tellurium. (b) Arrangement of these helical chains in a hexagonal lattice. Figure adapted from Oliveira.[60]

The atomic chains run along the c axis and are arranged in a hexagonal pattern on the a–b plane. Due to this structural anisotropy, Te naturally grows along the c axis and tends to form low-dimensional nanostructures such as nanowires (NWs) and nanorods (NRs).[61] The low-dimensional Te-based nanomaterials offer several advantages, including controllable shapes and excellent charge transport properties, such as high electrical conductivity and Seebeck coefficient.[62,63] Conducting polymers, as mentioned in Section 1.4, have their own beneficial properties such as low thermal conductivity, ease of large-scale solution processing, and good flexibility. As a result, Te-based nanostructured materials are often combined with conducting polymers to leverage the strengths of both components.[64] For instance, Yang et al.,[65] synthesized tellurium nanowires (TeNWs) using a chemical solution method, with varying diameters ranging from 42 to 186 nm and lengths between 3 and 4 microns. These nanowires were then incorporated into PEDOT: PSS polymer to create composite materials. Analysis of the thermoelectric transport properties of these composites revealed that the electrical conductivity (σ) consistently increased from 11 to 43 Scm^{-1} as the nanowire diameter decreased from 186 to 42 nm, while the Seebeck coefficient (S) remained nearly constant at around 302 μVK^{-1} across all samples. This resulted in a collective enhancement of the power factor from 90 to 415 $\mu Wm^{-1}K^{-2}$. Notably, for the composite containing the smallest nanowires with a diameter of 42 nm, an electrical conductivity of 43 Scm^{-1}, a Seebeck coefficient of 311 $\mu V\text{-}K^{-1}$, and a low thermal conductivity (κ) of 0.68 $Wm^{-1}K^{-1}$ were attained, leading to a zT value of 0.18 at 300 K.

Coates et al.[66] synthesized TeNWs using an aqueous solution method and combined them with the conducting polymer PEDOT:PSS to investigate the thermoelectric properties of the resulting hybrid materials. In their process, they first dissolved ascorbic acid (a reducing agent) in deionized (DI) water, then added PEDOT: PSS and Na_2TeO_3 (the metal precursor) while stirring the mixture vigorously. The mixture was heated to 90°C and left overnight. Afterward, the mixture was centrifuged at 9000 rpm for 30 minutes. The supernatant was discarded, and the remaining

material was redispersed in DI water and centrifuged again. The final product was resuspended in DI water to create the PEDOT: PSS/TeNWs solution. To adjust the composition, additional PEDOT: PSS was added to the PEDOT: PSS/TeNWs solution. Films were made by drop-casting this solution onto quartz substrates to measure the transport properties. The hybrid films of TeNWs/PEDOT: PSS showed a Seebeck coefficient of 180 μV/K and a power factor of ~ 35 μW/m-K².

Recently, Sik Wan et al.[67] developed nanocomposite materials based on Bi_2Te_3 nanowires (NWs) combined with PEDOT:PSS. The Bi_2Te_3 NWs were synthesized using a conventional polyol process with ethylene glycol (EG) as a solvent, involving a two-step solution-phase reaction. Initially, TeNWs templates were created by dissolving polyvinylpyrrolidone (PVP), sodium hydroxide (NaOH), and tellurium dioxide (TeO_2) in EG at 130°C, followed by adding hydrazine hydrate at 170°C. Then, a bismuth precursor solution was prepared by dissolving bismuth nitrate in EG, which was added to the Te-NWs solution, along with more hydrazine, and stirred at 170°C. The resulting Bi_2Te_3 NWs were purified and then mixed with PEDOT: PSS. The mixture was spin-coated onto glass substrates and treated with polar solvent vapor annealing (PSVA) using dimethyl sulfoxide (DMSO) to enhance the material's properties. The resulting hybrid films, exhibited S ~ 45 μV/K, σ ~ 1000 S/cm, PF~ 205 μW/m-K², and a figure of merit (zT) of 0.2 at 300K.[67]

Similarly, other research groups have explored composites based on different conducting polymers (CPs) for thermoelectric applications. For example, Deng's group[68,69] conducted a series of studies on Te/PANI composites, while Li's group[70] reported Te/PPy composite films with a power factor of approximately 234 μW/m-K². Ming's group[57] incorporated Bi_2Te_3 nanowires (NWs) into P3HT using a solution mixing process and achieved a power factor of 14 μW/m-K² for the hybrid composite materials.

1.6 Strategies for Enhancing Thermoelectric Performance of Organic-inorganic Hybrid Composites

To improve thermoelectric performance in organic-inorganic hybrid composites, several strategies are used: Nanostructuring the inorganic component, doping the polymer to increase electrical conductivity, engineering interfaces between inorganic and organic components to enhance the Seebeck coefficient, and strongly aligning the polymer on the surface of the inorganic component. These approaches are detailed in the following section.

1.6.1 Nanostructuring of Inorganic Component

To decouple phono-electron effects, nanostructured materials are considered to play a key role in controlling S and κ. Dresselhaus *et.al,*[71] has performed theoretical calculations on low-dimensional structures, revealing that one-dimensional nanowires exhibit higher thermoelectric performance compared to their bulk form due to quantum confinement effects (where the movement of charge carriers is confined in only one (1D) or two dimensions (2D) and increase in phonon scattering at the interfaces which leads to reduce the thermal conductivity. They hypothesized that 1D nanowires of Bi_2Te_3 can achieve the zT = 14 with 5nm diameter of NWs, while 2D quantum well Bi_2Te_3 with the same diameter may have zT = 5. Such effects have been observed in SbTe NWs,[72] InAs NWs,[73] Bi NWs,[74] and Si NWs.[75] Therefore, low-dimensional materials have attracted a great deal of attention.

Nanowires are one-dimensional structures, characterized by diameters typically on the scale of 100 nm or less and lengths ranging from a few microns to tens of microns,[76] offering a high surface-to-volume ratio. In their single-crystalline form, they demonstrate enhanced charge transport properties, making them advantageous for various energy conversion applications such as sensors, solar cells, lasers, transistors, and thermoelectrics.[77,78,79,80]

Tellurium (Te) is a p-type semiconductor with a narrow bandgap of 0.33 eV at room temperature,[81] and it serves as a key component in many high-performance thermoelectric materials, including Bi_2Te_3,[82,83] Sb_2Te_3,[84] Ag_2Te,[85] $Cu_{1.75}Te$,[86] CdTe,[87] and PbTe.[88] As a result, extensive research has focused on doping and alloying Te with various materials to enhance the efficiency of thermoelectric materials.[89,90] Notably, recent advancements have been achieved in the synthesis of one-dimensional (1D) nanostructures of Te, such as nanorods and nanowires. These 1D nanostructures exhibit restricted carrier motion in two directions, leading to unique properties that differ from those of the bulk material with the same chemical composition.[91,92]

1D tellurium nanowires (TeNWs) have been extensively utilized in the development of thermoelectric devices, photoconductors, as well as high-resistivity and piezoelectric devices.[93,94,95,96] To date, a variety of TeNWs with diverse diameters and lengths have been synthesized using a wide range of methods, including solution-based and vapor-phase methods.[97,98,99] Common synthesis methods such as hydrothermal, solvothermal, aqueous chemical methods, microwave-assisted ionic liquid method and electrodeposition have been extensively explored for producing tellurium-based nanowires. For instance, Wang et al.[81] and Park et al.[93] employed a hydrothermal process to synthesize TeNWs with diameters ranging from 10 - 35 nm and 30 - 140 nm, respectively. Zhu et al.[98] synthesized TeNWs using a microwave-assisted ionic liquid method. They dissolved 24 mg of polyvinylpyrrolidone (PVP) in 0.5 mL of the ionic liquid

$BuPy^+[BF_4]^-$ under stirring at room temperature in a 10 mL tube. To this mixture (designated as solution A), two drops of a 3.67M $NaBH_4$ aqueous solution were added while maintaining room temperature. Separately, 6 mg of TeO_2 was added to 1 mL of $BuPy^+[BF_4]^-$ under continuous stirring at room temperature to form solution B. Solution A was then subjected to microwave heating at 180°C for 70 sec., after which solution B was gradually introduced at 180°C. The combined solution was maintained at 180°C for an additional 10 minutes before the microwave heating was stopped, allowing the solution to cool to room temperature. Zhu et al. observed that many of the synthesized nanowires exhibited diameters between 20 and 100 nm, with a smaller fraction displaying diameters between 100 and 500 nm. The lengths of the nanowires were found to extend to tens of microns. Silva et al.[100] reported the synthesis of single-crystalline TeNWs with varying aspect ratios through a surfactant-assisted approach, achieving diameters below 30 nm and tuneable lengths from 600 nm to 5 μm. Stavila et al.[101] utilized a low-temperature wet-chemical method to synthesize tellurium nanostructures, while Zhang et al. introduced a visible light-assisted solution-phase method for generating trigonal tellurium nanostructures.[102] However, there is limited exploration into manufacturing thin films based on ultra-fine tellurium nanowires for wearable thermoelectric devices.

The advancement of thermoelectric films based on nanowires, with improved electrical conductivity and high Seebeck coefficient, is highly desirable for wearable electronic applications.[103,34] In this regard, TeNWs exhibit intriguing characteristics as semiconductors, particularly in the context of thermoelectric applications, attributed to their high Seebeck coefficient.[93] For instance, Yee et al.,[104] highlighted Te's remarkable Seebeck coefficient values of 400 μV/K, while See et al.,[105] reported a slightly higher value of 408 μV/K. Wang et al., observed a Seebeck coefficient value of 551 μV/K at room temperature.[81]

It should be noted that the diameters of the tellurium nanowires reported in the literature (20-100 nm) and in this thesis (40-60 nm) are larger than the exciton Bohr radius of tellurium (1-5 nm). As a result, strong quantum confinement effects are unlikely, although weak size-dependent effects may still occur. Nevertheless, many research groups have recently used nanowires in combination with polymers to improve the performance of organic-inorganic hybrid composite materials. Detailed information about this approach can be found in Section 1.5.

1.6.2 Energy Filtering Effect

The energy filtering effect refers to the selective transport of charge carriers at the interface between organic and inorganic materials. At these interfaces, low-energy charge carriers are impeded, while high-energy charge carriers are permitted to pass. This process effectively raises

the average energy of the carriers, thereby increasing the Seebeck coefficient (S).[9] Nevertheless, to observe the effective energy filtering phenomenon, several parameters need to be considered: i) Ensure intimate contact between the polymer and nanomaterials to create well-defined organic-inorganic interfaces. ii) Match the work functions of the polymer and nanomaterials to enable the transfer of high-energy carriers across the interfaces. iii) Maintain an interfacial barrier height between 0.04 - 0.10 eV to selectively scatter low-energy carriers while allowing high-energy carriers to pass. iv) Use one-dimensional nanostructures to form effective potential barriers with a lower filler concentration compared to zero-dimensional nanomaterials.[106,107,108,109,105,110] Figure 1.6 is an example to demonstrate the energy filtering effect in p-type semiconductors. The band diagrams for $Bi_{0.5}Sb_{1.5}Te_3$ (BST) and PEDOT: PSS are shown, displaying their work function (ϕ), electron affinity (χ), ionization potential (ψ), and band gap (E_g).

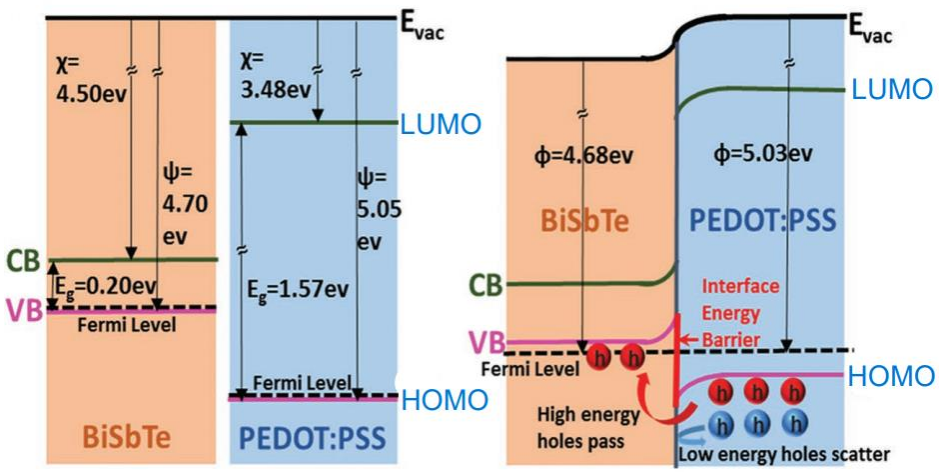

Figure 1.6. Band diagram of $Bi_{0.5}Sb_{1.5}Te_3$ and PEDOT: PSS , before contact (left) and after contact (right), illustrating band alignment and energy filtering effect. Work function (ϕ), electron affinity (χ), ionization potential (ψ), and energy gap (Eg) values for both organic and inorganic components are indicated. Adopted from Zhang.[109]

Before contact, BST and PEDOT: PSS exhibit distinct band structures. Upon forming the PEDOT: PSS-BST heterojunction, differences in their Fermi levels create an energetic mismatch at their interfaces. Consequently, energy barriers arise in the valence bands of BST nanomaterials and PEDOT: PSS, hindering the transmission of low-energy holes by scattering at the interface. Only high-energy holes can traverse the interface, leading to decreased carrier concentration (n) and increased Seebeck coefficient. Therefore, the establishment of a suitable interfacial energy barrier could result in an improved Seebeck coefficient and power factor of hybrid composite materials.

However, there are controversies around the energy filtering effect in hybrid composite materials which originate from difficulties in clearly proving its role and actual impact on thermoelectric performance. In practice, achieving effective energy filtering without significantly degrading

electrical conductivity is challenging.[111] It is demonstrated that energy filtering often results in increased scattering of all carriers, leading to a reduction in overall electrical conductivity, which diminishes the net TE performance.

Experimentally, it is difficult to directly measure the energy filtering in hybrid materials. An increase in the Seebeck coefficient alone is not enough to clearly prove the energy filtering effect because multiple electronic transport properties are interconnected. For instance, electrical conductivity depends on both the concentration and mobility of charge carriers, so it is important to separate these two factors when analysing the data. Without doing so, the source of the Seebeck enhancement cannot be accurately identified.[111] There are alternative explanations for the observed improvements in TE performance, such as grain boundary scattering, suppressing phonon transport, or quantum confinement effects, which can also enhance TE properties without invoking energy filtering.[14,112,111]

Additionally, the controversial aspect also arises from the fact that many experimental results are not reproducible across different research groups, raising concerns about whether observed improvements are due to energy filtering or experimental artifacts. Graham's research team[113] precisely manipulated the energy barrier between the transport states in P3HT and tellurium nanowires by adjusting the $FeCl_3$ concentration, tuning the barrier between 0.08 eV and 0.88 eV. Their study showed that the composite materials had higher power factors and increased Seebeck coefficients as the tellurium nanowire concentration increased. However, after comparing their results with theoretical models for parallel and series connected composites, they concluded that the improvement in Seebeck coefficients and power factors was unlikely due to the energy filtering effect. Although theoretical predictions of the energy filtering effect align with experimental results, the data can only be interpreted in a semi-quantitative manner. More precise measurements and additional experimental validation are required to fully understand the effects of charge carrier scattering.

1.6.3 Doping of Organic Component

The low electrical conductivity, a limitation of the organic component in hybrid materials, can be significantly enhanced by doping the organic polymer. To understand how doping occurs, a conducting polymer poly(3-hexylthiophene) P3HT is taken as an example. The pristine P3HT film is dipped into the dopant [Nitrosonium hexafluorophosphate] $NOPF_6$/acetonitrile solution. Figure 1.7 shows the molecular structure of P3HT before and after doping. [47]

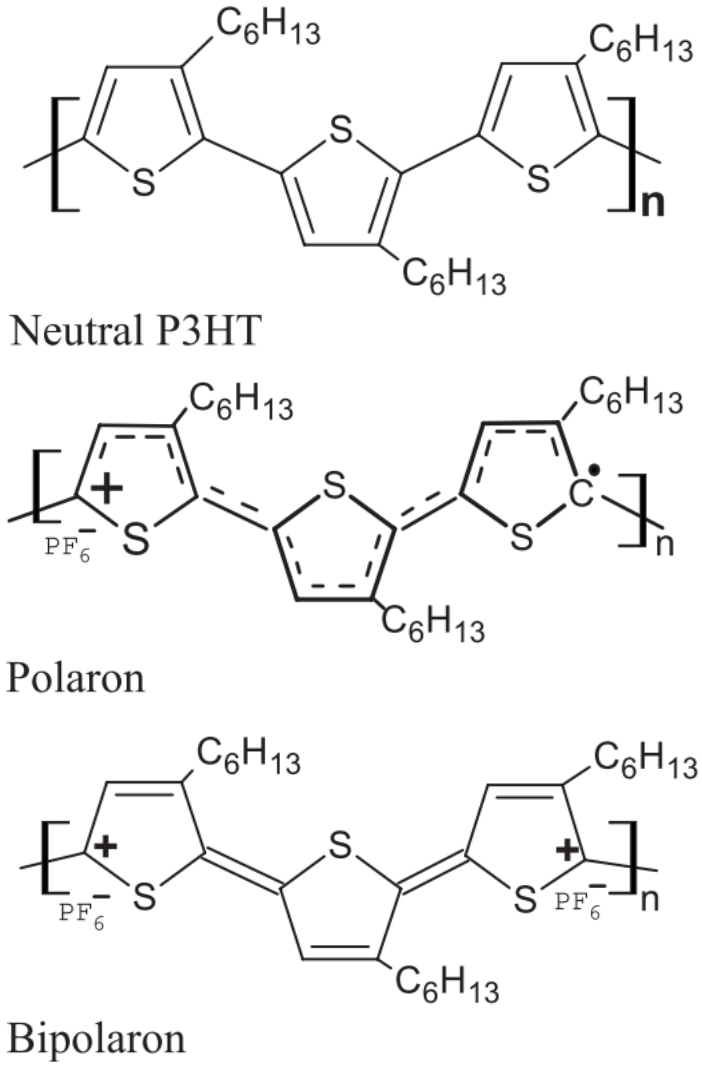

Figure 1.7. A chemical structural sketch of pristine P3HT polymer indicating polarons (singled-charged), and bipolaron (doubled-charged) with counter ions when doped in $NOPF_6$/ acetonitrile solution, the light doping gives rise to polarons while increase in dopant concentration render bipolarons.

Through acceptor doping (p-type doping), an ionic complex consisting of positively charged polymer chains and counter ions is formed. The counter ions are generated by reduction of acceptors. Doping of CPs generates charge carriers known as polarons and bipolarons. When a conducting polymer is doped, the removal of an electron from the polymer chain takes place (oxidation) and local charge appears on the polymer chain is known as polaron. In chemical terminology, a polaron is just a radical ion (spin ½) associated with local distortion (relaxation) of lattice. If a second electron is removed from the polymer chain, then the formation of bipolarons is obtained. A bipolaron is defined as a pair of like charges that should be bound to one another associated with a strong local distortion (relaxation) of lattice.[114] These charge carriers are collectively called as elementary excitations or self-localized excitations which move along the polymer chain and

induces geometrical changes. On doping the P3HT film, the chemical reaction of the doping is as follow:

$$\mathrm{NOPF_6} + P3HT \rightarrow \mathrm{NO} + P3HT^{+}(\mathrm{PF_6})^{-} \qquad \text{Equation 9}$$

According to equation 9, when a conducting polymer P3HT is doped with the oxidizing agent $NOPF_6$, the positive charge carriers and PF_6 counterions are generated. These counterions create a disordered environment through which the p-type charge carriers move. As doping levels increase, this disorder is reduced, and the counterions' localizing effects diminish. This leads to a significant increase in electrical conductivity while the Seebeck coefficient decreases.[115]

Doping is a common method used to tune the charge carrier's density in CPs.[116] This can be done in different ways, such as through electrochemical methods by oxidizing or reducing a polymer layer on an electrode,[117] or via redox doping using strong electron-accepting molecules. In p-type polymer semiconductors, effective doping involves a careful alignment of the polymer's highest occupied molecular orbital (HOMO) with respect to the lowest unoccupied molecular orbital (LUMO) of the dopant. For polymers with deep HOMO levels, it is essential to use dopants that have high electron affinity (EA).[118] Recently, Martin's group did a comparative study to explore on how the structure of P3HT affects its thermoelectric (TE) properties when doped with various dopants, such as 2,3,5,6-tetrafluoro-7,7,8,8-tetracyano quino-dimethane [F4TCNQ], 1,3,4,5,7,8-hexafluoro-tetracyano -naphtho-quino dimethane [F6TCNNQ], iron trichloride [$FeCl_3$], molybdenum dithiolene [Mo(tdf-$COCF_3$)$_3$], and tris(4-bromophenyl) ammoniumyl hexachloroantimonate (Magic blue -MB). The electron affinities (EA) (i.e. LUMO position) of different dopants and HOMO of P3HT along with their TE transport properties are shown in Figure. 1.8.

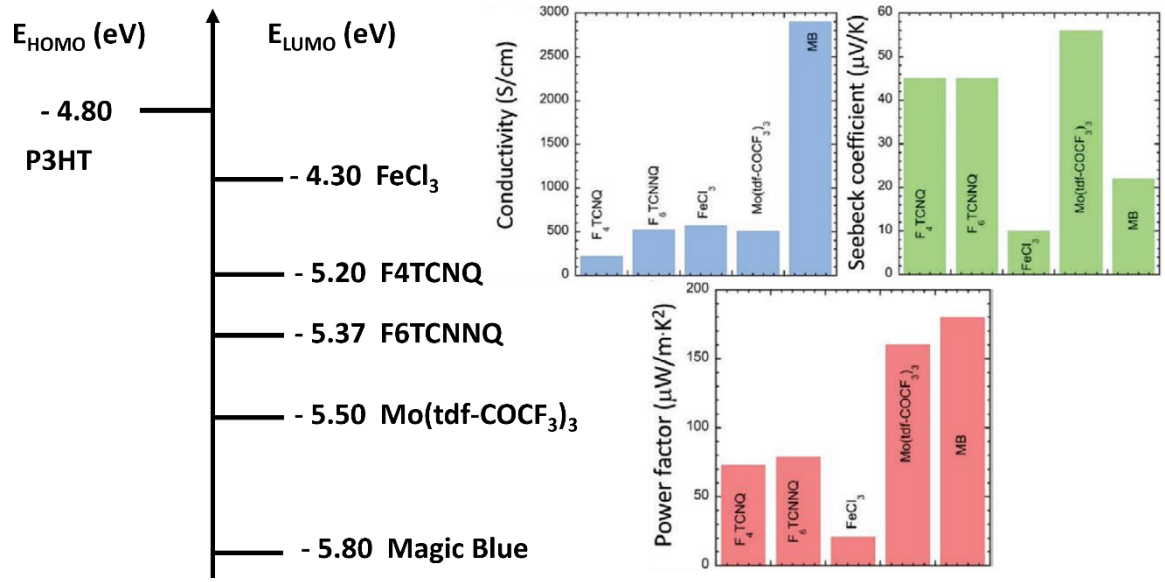

Figure 1.8. HOMO of P3HT and LUMO of dopants along with σ, S, and PF measured in the direction parallel to the polymer chains in rubbed thin films of P3HT doped with different dopants.[118]

As can be seen in Figure 1.8, the dopants differ in their electron affinities, which affect how well they dope different parts of the polymer, such as its crystalline and amorphous regions. For example, F4TCNQ and F6TCNNQ primarily dope the crystalline regions,[51] while $FeCl_3$ and Mo(tdf-$COCF_3)_3$ can dope both the crystalline and amorphous parts, leading to higher conductivity.[119] Non-oriented P3HT films doped with MB showed an electrical conductivity of 26 S/cm. However, when the P3HT films were aligned along the chains direction and doped with 0.2 g/l of MB, the conductivity increased significantly to about 2900 S/cm, with a maximum power factor of 170 ± 30 $\mu W/mK^2$.[118] It is demonstrated that the highest charge mobilities are observed when the dopant MB primarily doped the amorphous regions, leaving the crystalline structure largely unchanged. In this case, the nanocrystals of P3HT were doped at their interface with the surrounding amorphous areas. These findings suggest that targeting the amorphous regions in semicrystalline polymers can reduce polaron localization, improve charge mobility, and enhance TE performance.[118] Furthermore, the study highlights that aligning the polymer chains is crucial for improving the electrical conductivity of conducting polymers.

The author also conducted a comparative study on several conducting polymers, including poly[2,5-bis(3- alkylthiophen-2-yl) thieno [3,2-b]thiophene] PBTTT-based derivatives (PBTTT-C12, PBTTT-C14, PBTTT-8O), 3,3-didodecyl-2,2,5,2-terthiophene [PG2T-TT], and P3HT (M.Ws ranging 30 kDa to 143kDa), using various dopants such as $FeCl_3$, MB, F4TCNQ, and F6TCNNQ, to evaluate their thermoelectric (TE) performance in thin films (shown in Appendix D). Except for PBTTT-8O, all the polymers were non-oriented. The films were immersed in dopant solutions (acetonitrile) for 20 to 40 seconds, with molar concentrations ranging from 0.005M to 0.03M. Interestingly, the non-oriented films doped with $FeCl_3$ performed better than those doped with other dopants. The highest performance was observed in PBTTT-8O films aligned along the chain direction and doped with 0.005M $FeCl_3$, achieving an electrical conductivity of ~330 ± 6 S/cm, a Seebeck coefficient of ~ 170 ± 9 μV/K, and a power factor of ~ 948 ± 17 $\mu W/m\text{-}K^2$. This suggests that the combination of $FeCl_3$ as a dopant and proper alignment of polymer chains is key to achieving high TE performance, while non-oriented films show lower overall performance.

In case of organic-inorganic composites, doping assist to rationally engineer the band alignment (or so called interfacial potential barriers) between organic and inorganic components. Within composite materials, a transfer of charge from organic to inorganic components may occur as their chemical potentials align. Ionized organic components then provide carriers to the inorganic matrix,

reducing electron scattering.[9] In this way, an increase in charge carrier concentration via doping can enhance electrical conductivity in composite materials, it may also reduce the Seebeck coefficient. Furthermore, careful selection of dopants can not only enhance electrical conductivity but also influence the conduction type and morphology of the film. Consequently, optimizing the doping level is essential to attain maximum performance of composite materials.[47] Many research studies have documented performance enhancements in composite thermoelectric materials through doping.[113,120,121,122] For instance, Ming He *et al*. manipulated the $FeCl_3$ doping level from 8 wt% (light doping) to 32 wt% (heavy doping) to engineer the interface between P3HT and Bi_2Te_3 nanowires, achieving a noteworthy power factor of 14 μW $m^{-1}K^{-2}$ for P3HT- Bi_2Te_3 nanocomposites at room temperature.[57] Since the composites lack ionic impurities within the matrix of inorganic materials, therefore the surface doping can be a novel pathway to enhance the TE performance of organic-inorganic composites.

1.6.4 Templating Effect or Interfacial Ordering

The molecular chains in conducting polymers usually have random orientations, forming a coil-like structure. Carrier transport between these individual chains occurs through thermally assisted hopping, which leads to significantly lower electrical conductivity. Consequently, the associated Seebeck coefficient is also reduced compared to metallic band transport within the chains. Introducing a secondary phase can transform the coil structure into an extended linear arrangement through a templating effect, thereby enhancing electronic transport properties.[9]

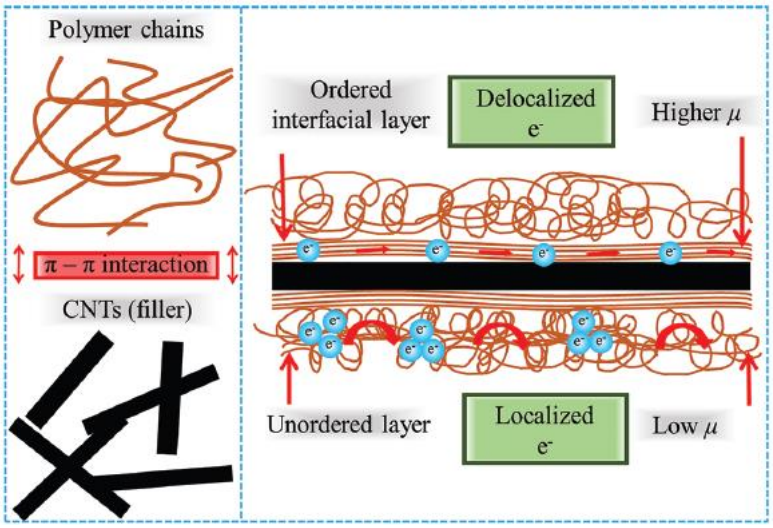

Figure 1.9. Schematic representations of the formation mechanisms of templating or interfacial ordering effect by combining conducting polymer PANI with CNTs, adapted from Ref.[3]

π–π interactions between polymer chains and the surface of fillers (such as CNTs, inorganic nanostructures) can lead to a more ordered arrangement of polymer chains near the interface,

known as the templating effect or interfacial ordering effect, which enhances both charge carriers' mobility (μ) and electrical conductivity (σ).[121,123] Figure 1.9 illustrates how an in situ polymerization method was used to promote this interfacial ordering. Normally, polymer chains are amorphous, causing carriers to become localized, resulting in low charge-carrier mobility.[123] Fillers such as carbon nanotubes (CNTs) interact with the π-bonds in polymers and serve as one dimensional template, guiding the polymer chains to grow in an ordered manner. This reduces barriers for charge hopping between and within polymer chains, leading to increased delocalization of carriers and resulting in higher mobility.[124,125]

Yao et al. used an in-situ polymerization method to create a composite of single-walled CNTs (SWCNTs) and polyaniline (PANI), achieving an electrical conductivity of 125 S/cm, a Seebeck coefficient of ~ 40 μV/K and a power factor of 20 $\mu W/mK^2$ at room temperature. These values are significantly higher than those of the individual materials, primarily due to the ordered molecular structure of the PANI chains along the SWCNT surfaces, which improved carriers' mobility.[123]

It is reported that interfacial ordering happens only between CNTs and the nearby polymer chains. However, the polymer chains farther from the CNT interface remain amorphous and show poor mobility. Yao et al. addressed this by treating PANI with a secondary dopant, m-cresol, before mixing it with SWCNT fillers to fabricate SWCNT/PANI composites. Along with improving the ordering at the interfaces, m-cresol helped to organize the polymer chains away from the interface, enhancing the overall structural order and improving mobility (μ). This resulted in a high power factor of up to 176 $\mu W/mK^2$ and a zT value of 0.12 at room temperature.[126]

However, in organic-inorganic composites, it remains unclear whether the transport properties are primarily influenced by the inorganic phase, the organic phase, or interfacial properties. To explore the charge transport (CT) mechanism of conducting polymers, Kang and Snyder developed a CT model based on the Boltzmann transport framework.[127] According to the Kang-Snyder model, the energy-dependent conductivity $\sigma_E(E,T)$ can be expressed as:

$$\sigma_E(E,T) = \sigma_{E_0}(T)\left(\frac{E-E_t}{k_B T}\right)^s \qquad \text{Equation 10}$$

Where E/K_BT is the reduced energy of the charge carriers (electrons or holes), E_t is the transport edge (energy) of charge carriers below which no electrons or holes exist or conductivity has no contribution even at finite temperature, 's' is the energy-dependent scattering parameter and 'σ_{E0}' is a temperature-dependent but energy-independent transport parameter to model the TE transport of conducting polymers over a large range of conductivities. k_B is the Boltzmann constant. The total conductivity is given by:

$$\sigma = \int_0^{\infty} \sigma_E(E,T)\left(-\frac{\partial f}{\partial E}\right) dE \qquad \text{Equation 11}$$

By inserting equation (10) into equation (11), and integrating by parts, the total conductivity can be expressed as:

$$\sigma = \sigma_{E_0}(T) \times sF_{s-1}(\eta) \qquad \text{Equation 12}$$

Where $\eta = \frac{E_F - E_t}{k_B T}$ is the reduced chemical potential and F is the Fermi integral. The corresponding Seebeck coefficient (S) can be expressed as:

$$S = \frac{k_B}{e}\left[\frac{(s+1)F_s(\eta)}{sF_{s-1}(\eta)} - \eta\right] \qquad \text{Equation 13}$$

The reduced chemical potential (η) is determined by using the experimental values of the Seebeck coefficient for a specific value of the energy dependent parameter *s*.

In Kang-Snyder charge transport (CT) model, TE transport of CPs is described using two key parameters: σ_{E0} and s. The parameter σ_{E0} determines the magnitude of conductivity, while s determines the curve shapes. However, it is challenging to accurately measure these parameters individually. Additionally, this model does not account for organic-inorganic hybrid materials, leaving a significant gap in the study of these material types that requires further research.

Recently, to explore the effect of templating and charge transportation in organic-inorganic composites, Kumar et al. employed the Kang and Snyder transport model, molecular dynamics simulations, and first-principles calculations on TeNWs-PEDOT:PSS hybrid systems.[128] Their findings indicated that the high thermoelectric performance in these hybrid systems could be attributed to interfacial interactions between the inorganic and organic components, which enhance both the Seebeck coefficient and carrier mobility. Experimentally, highly ordered morphologies of conducting polymers have been demonstrated through interfacial interactions with inorganic nanostructures, creating highly conductive pathways for charge carriers.[66,129] In this project, the Kang-Snyder CT model is extensively utilized to explore the charge transportation in organic-inorganic composites and templating effect on enhancing the thermoelectric (TE) performance of the fabricated hybrid materials.

Chapter 2 Experimental Methodology

This chapter describes the experimental methodology employed in this research work. It encompasses the procedures for synthesizing nanomaterials, modifying their surfaces, and incorporating them into conducting polymers to fabricate composite materials. Furthermore, it reviews the characterization techniques used to quantify the materials and their thermoelectric properties, alongside the theoretical principles underpinning these techniques.

2.1 Synthesis Method

2.1.1 Aqueous Solution Chemical Synthesis Methodology

The experimental setup for aqueous solution synthesis (ASS) is shown in Figure 2.1 and consists of a Schlenk line, a condenser, and a round bottom flask (RBF) containing the reaction mixture. The RBF is purged of oxygen by using a vacuum pump through the Schlenk line for 5-10 min, then the nitrogen gas flows into the Schlenk line and RBF for 3-5 min. This process is repeated three times to eliminate as much oxygen as possible before running the ASS. To accelerate the chemical reactions, processes such as heating, magnetic stirring, and the introduction of gases (argon or nitrogen) are employed during synthesis.[130] The precursor materials dissociate into ions, which subsequently react to form crystal nuclei, followed by crystal growth. By carefully tuning the temperature, the size of the synthesized nanostructured materials can be controlled. Consequently, a variety of low-dimensional materials, including nanowires, nanosheets, nanorods, quantum dots, and quantum wires, can be obtained via aqueous solution process for diverse applications in thermoelectric device design.[11] Due to the inexpensive precursor materials, the aqueous solution route is a more cost-effective synthesis method. To obtain a clean final product, post-treatments such as sedimentation, washing, and drying are applied to the as-synthesized product.

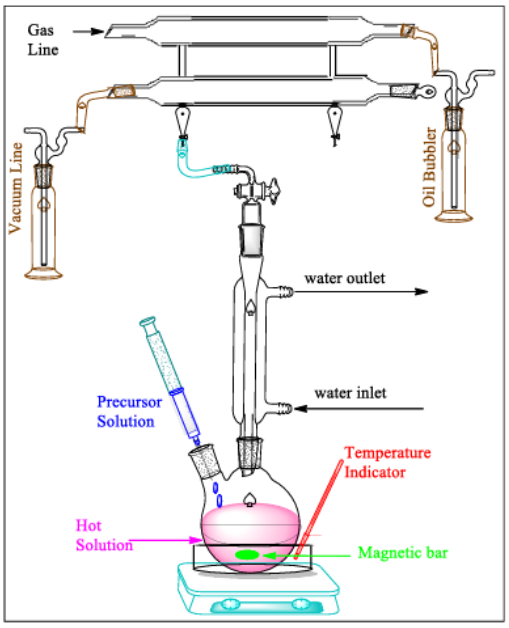

Figure 2.1. Schematic setup for the synthesis of nanostructured materials. The setup includes a round bottom flask (RBF) containing a magnetic stirring bar and precursor solution, placed on a hotplate to ensure homogeneous heating for the reaction. The RBF is connected to a condenser with water flow, and further attached to a Schlenk line to maintain an inert environment during the chemical reaction.

2.1.2 Synthesis of Tellurium Nanowires

The inorganic nanostructures of tellurium nanowires (TeNWs) were synthesized via an aqueous solution route following established literature protocols.[131] For the synthesis of Tellurium nanowires, the following reagents were employed: 20 mL ethylene glycol (EG anhydrous, Fisher Chemical, >99%) as the solvent, 0.2 g polyvinylpyrrolidone (PVP-K30, M.W~ 40,000, Fluka) as a growth-directing agent, 0.66 g potassium hydroxide (KOH, Fisher Chemical) to create the necessary basic environment for the reaction, 0.4778 g tellurium dioxide (TeO_2, Aldrich Chemical, 99+%) as the Tellurium precursor, and 1mL hydrazine hydrate (Sigma Aldrich, N_2H_4 50-60%) as the reducing agent. The schematic of the synthesis process is depicted in Figure 2.2.

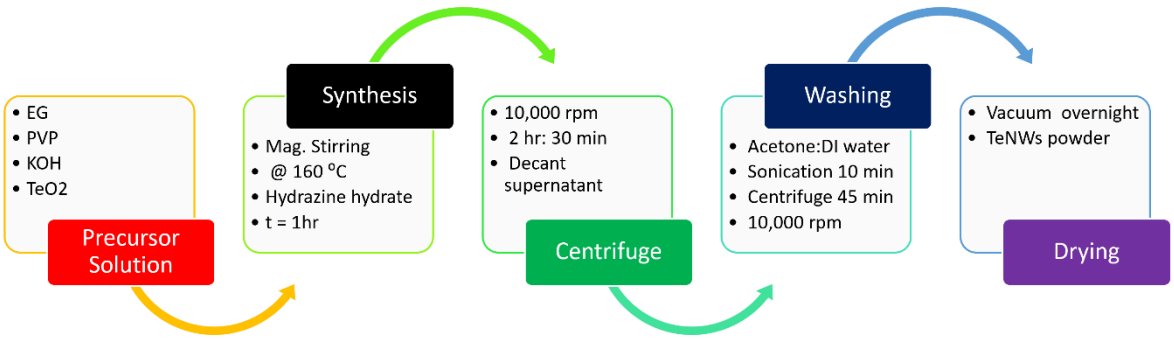

Figure 2.2. Schematic of aqueous solution process to synthesize Tellurium nanowires.

The PVP, KOH, and TeO_2 were dissolved in 20 mL of EG by continuous magnetic stirring. The tellurium solution was transferred into a round bottom flask (RBF), connected to a condenser with cold water circulating through it. A magnetic stirrer bar, operating at 600 rpm, was utilized to maintain uniformity of the reaction in the RBF. The solution temperature was gradually raised to 160°C using a hot plate and a silica oil bath. As the temperature increased, the solution colour transitioned from clear to dark yellow, and eventually to light black upon reaching 160°C, indicating the reduction of TeO_2 by EG. Following one hour at 160°C, hydrazine hydrate was introduced into the RBF and the reaction kept running further for one hour, resulting the light black solution to change into dark black, indicating a strengthening of the reduction reaction. To control the length of the nanowires or to grow longer ones, the reaction time was extended by 3 hours after adding hydrazine hydrate. With this reduction reaction, TeO_2 was reduced to form metallic Te seed particles.[94] As these seed particles grew, their growth was controlled by PVP (capping agent), leading to the formation of Te nanowires.[132] Upon completion of the reaction, the solution was cooled to room temperature and transferred into a glovebox. Subsequently, it was centrifuged at 10,000 rpm for 2 hours and 30 minutes. The resulting supernatant was decanted, leaving behind the nanowire precipitant. During post-synthesis, the nanowires underwent cleaning via dispersion (via bath sonication) in a cleaning solution composed of a 3:1 mixture of acetone and deionized water. This cleaning solution was selected because studies have shown that it effectively removes PVP.[133] These dispersions were then centrifuged at 10,000 rpm for 30 minutes, and the resulting supernatant was decanted. This cleaning process was repeated thrice to ensure the removal of any unbound residues. Finally, the nanowires were dried overnight under vacuum. To synthesize TeO_2 nanowires, the synthesis process was slightly modified: the precursor materials were dissolved in hydrated ethylene glycol (EG), and all steps were conducted in a fume hood environment instead of a glovebox.

2.1.3 Surface Modification of TeNWs with Linkers

For removing residual PVP and reducing surface oxidation on Te nanowires (TeNWs), surface modification of nanowires through suitable ligands is considered as an effective approach.[134] For the surface modification of as-synthesized TeNWs using S^{2-} linkers, equal amount of Te nanowires (TeNWs) and sodium sulfide (Na_2S) were dispersed in deionized (DI) water with continues magnetic stirring for 30 minutes. After stopping the reaction, the dispersions were centrifuged for 45 minutes at 10,000 rpm. On decanting the supernatant, the precipitated sulfur-capped nanowires were dispersed again in DI water (via 10 minutes bath sonication) and centrifuged for 30 minutes at 10,000 rpm. This cleaning process was repeated three times to ensure the removal of any unbound species. Finally, the nanowires were dried overnight under vacuum.

2.1.4 Mechanical Mixing to Fabricate Composite Materials

Among the various methods for preparing composite materials, in situ synthesis and solution casting are primarily used for organic-inorganic nanocomposites.[134] In situ synthesis, though more complex, effectively produces nanocomposites with well-dispersed inorganic materials within the polymer matrix. Conversely, solution casting (also known as mechanical mixing) is a simpler and more common process. It involves mixing polymers and inorganic nanostructured materials in solvents and shaping them into films or membranes using methods such as drop-casting, spin coating or screen printing. Solution casting offers easier control over the component ratio in organic-inorganic hybrid composites.[135] To integrate the polymer with nanowires for the fabrication of composite materials in this project, Poly(3-hexylthiophene) (P3HT) was dissolved in chloroform ($CHCl_3$) to prepare a polymer stock solution at a concentration of 10 mg/ml. This solution was magnetically stirred at 40°C on a hotplate for 45 minutes to achieve homogeneity. Subsequently, nanowires were added to the P3HT solution in varying ratios (10-90 weight %) and the mixture underwent power sonication in pulse mode (15 seconds ON, 5 seconds OFF) for 60 minutes to ensure a uniform dispersion of the composite materials. The final dispersion was then drop-cast onto rigid substrates (Si and quartz).

2.2 Thin Film Fabrication

2.2.1 Thin Film of Inorganic nanowires, polymers, and composites

For material characterisation and thermoelectric transport properties measurements, thin films were fabricated via drop casting onto quartz substrates (20 mm diameter, 7×7 mm², and 3×10 mm²) and silicon substrates (1×1 cm²). The nanowires were dispersed in a 3:2 isopropanol (IPA) to ethanol solution to form a homogeneous and stable suspension, followed by 30 minutes of sonication and 30 minutes of magnetic stirring. After drop casting the suspended nanowires, the films were allowed to dry at room temperature and then heated on a hotplate at 100°C overnight in a nitrogen-filled glovebox. Similarly, films of composite materials with varying nanowire-to-polymer ratios as detailed in section 2.1.4 were fabricated.

To create thin films of conducting polymers (e.g., P3HT of various molecular weights, PBTTT-C14, and PG2T-TT), 200 µL of polymer solution was spin-coated onto 2.5×2.5 cm^2 quartz substrates at 1000 rpm for 1 minute, followed by heating on a hotplate at 100°C for 10 minutes. Prior to drop casting or spin coating, all substrates were cleaned with acetone and IPA, each with 10 minutes of sonication, then quickly dried with nitrogen, and subjected to UV ozone treatment at 100°C for 10 minutes.

2.2.2 Doping of Composite Films and Conducting Polymer Films

To investigate the effects of doping on the thermoelectric properties of polymers and composite materials, $FeCl_3$, a p-type dopant, was utilized with varying molar concentrations (10 – 70mM). The dopant solution was prepared by dissolving $FeCl_3$ in acetonitrile, and the fabricated films were immersed in this solution until a colour change from bright golden to black, indicated successful doping. Subsequently, the films were dried inside a nitrogen-filled glovebox, before measuring their thermoelectric properties.

2.3 Characterization Techniques

2.3.1 X-ray Diffraction (XRD)

To analyse the crystal structure of crystalline materials, X-ray diffraction (XRD) is a highly effective and non-destructive technique that provides detailed information on the size, phase, and lattice parameters of a material. When a monochromatic beam of X-rays hits an orderly structure of a crystal, the X-ray photons are coherently scattered by the periodic distribution of atoms in the crystal, as shown in Figure 2.3. For constructive interference to happen, the difference in the path lengths of X-rays reflected by consecutive atomic planes must be an integral multiple of the incident wavelength of the X-rays. This relationship is known as Bragg's law, expressed in equation 14.

$$2dsin\theta = n\lambda \qquad \text{Equation 14}$$

where θ is the angle between the X-ray source and the crystal plane, λ is the X-ray wavelength, and d is the interatomic spacing as indicated in Figure 2.3.

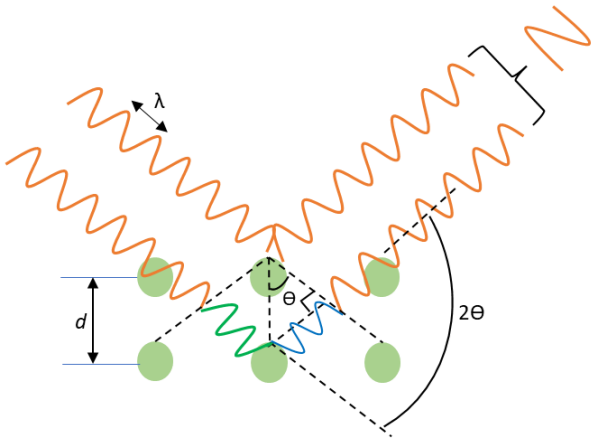

Figure 2.3. Illustration of Bragg's Law - This schematic diagram illustrates the concept of Bragg's Law, showing incident rays striking the crystal planes at specific angles. The rays reflect from different planes within the crystal, leading to constructive or destructive interference, which is the basis of the interference phenomenon.

The constructive interference of reflected rays from different planes produces characteristic peaks in an X-ray diffraction (XRD) spectrum. The resulting spectrum is then compared to reference spectra of chemical elements stored in the International Centre for Diffraction Data (ICDD) database to determine the sample's crystal structure. This analysis is facilitated by the powder X-ray diffraction profile analysis software (PDXL), which is integrated with the ICDD database. Additionally, another important parameter, the grain size of nanocrystals, can be measured from the most intense diffraction peaks in the spectrum using the Scherrer formula:[136]

$$D = \frac{0.9\lambda}{\beta cos\,(\theta)} \qquad \text{Equation 15}$$

In this equation, D represents the diameter of the nanoparticle, λ is the wavelength of the incident X-rays, β is the full width at half maximum (FWHM) of the diffraction peak, and θ is the Bragg's angle. Smaller grain sizes result in increased phonon scattering, which reduces thermal conductivity and enhances the thermoelectric figure of merit (ZT) values. In this study, X-ray diffraction patterns were obtained using a Bruker D8 Advanced X-ray powder diffractometer equipped with Cu Kα radiation (λ=1.54 Å) at room temperature. The instrument is in Kinesis Lab at IMRE-A*STAR, Singapore.

2.3.2 Scanning Electron Microscopy (SEM)

A scanning electron microscope (SEM) is a powerful and standard tool for imaging nanostructured materials and thin films, providing high-resolution images with fast processing times. A schematic of the SEM is shown in Figure 2.4.

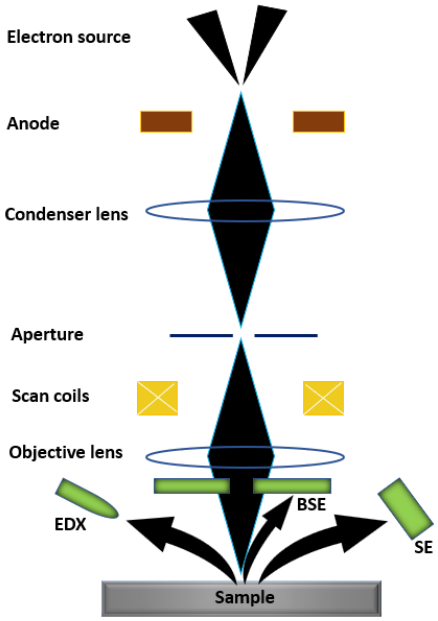

Figure 2.4. Schematic Diagram of Scanning Electron Microscope (SEM) - The electron beam passes through condensing and focusing lenses before impinging on the sample, generating multiple signals detected by various detectors. These include the Backscatter Electrons Detector (BSE), Secondary Electrons Detector (SE), and Energy Dispersive X-ray Photons Detector (EDX), each capturing different aspects of the sample's characteristics.

The SEM comprises an electron gun that generates an electron beam to scan the surface of a sample. When the electron beam interacts with the atoms of the specimen, it causes different electrical signals to be generated due to inelastic collisions.[137] These collisions involve the beam electrons interacting with the outermost electrons of the sample's atoms, leading to ionization.[138] Resulting signals from these interactions include X-ray Photons, emitted up to 10 µm into the sample; Backscattered Electrons (BSE), emitted up to a depth of 1 µm within the sample; Secondary Electrons (SE), produced up to 50 nm beneath the sample surface; and Auger Electrons, generated up to 1 nm beneath the sample surface.[139] In this thesis, SEM is performed using secondary electron imaging mode, which detects secondary electrons (SE). This is the most commonly used imaging method in SEM because it links the brightness of the image to different areas of the sample. To analyse thin films in this project, SEM imaging was performed using two microscopes: the Jeol FE-SEM JSM 7600F and the Jeol FE-SEM JSM 6700F. For acquiring high-magnification images, the Jeol FE-SEM JSM 7600F was specifically used. Both microscopes are in the Synthesis B2 lab at IMRE-A*STAR, Singapore.

2.3.3 Energy Dispersive X-ray Spectroscopy (EDS)

Energy dispersive X-ray spectroscopy (EDS) is an analytical technique used for the identification of the chemical composition in samples. Usually, EDS employs the electron beam emitted by a scanning electron microscope (SEM). When this electron beam, with energy usually between 15-30 kV, hits the innermost shell of an atom, electrons are dislodged from the inner shells, creating a vacancy as shown in Figure 2.5. Subsequently, an electron from a higher energy state fills this vacancy, a characteristic x-rays photon is emitted. The atomic number of the emitter can then be identified based on the energy of the spectral lines. Through this process, EDS enables the acquisition of compositional information. Additionally, EDS provides quantitative data, allowing for the determination of the atomic percentage of elements present in the sample. Typical EDS measurements carry an associated error margin of about 5%.[140] In this project, EDS spectra were collected using a Jeol FE-SEM JSM 7600F, equipped with an Oxford INCA EDS detector and INCA Software. The instrument is in the Synthesis B2 lab at IMRE-A*STAR, Singapore.

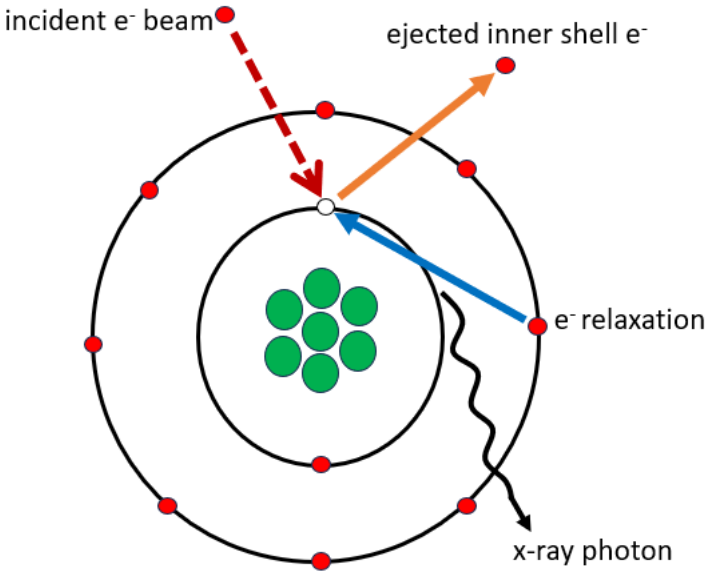

Figure 2.5. Schematic representation of the underlying physical principle behind EDX. Green circles indicate neutrons and protons in nucleus of the atom and red circles show the electrons.

2.3.4 Transmission Electron Microscopy (TEM)

Transmission Electron Microscopy (TEM) is a highly advanced electron microscope that uses a focused beam of electrons to create detailed and magnified images of specimens. As shown in Figure 2.6, TEM consists of three major systems: the Electron Gun, the Image-Producing System, and the Image-Recording System.[141]

The Electron Gun generates a stream of electrons using a heated tungsten filament (cathode), which emits electrons that pass through a control grid and an anode, accelerated by a high voltage. These electrons are directed onto the specimen by condenser lenses, which control the beam's focus and intensity.

The Image Producing System includes objective, intermediate, and projector lenses. As electrons pass through the specimen, they are focused by the magnetic lenses to form a highly magnified image. The objective lens, with a short focal length, creates an intermediate image, which is further magnified by the projector lenses.

The Image Recording System captures the resulting image on a fluorescent screen for viewing or digitally records it using a camera. The vacuum system ensures that the electron beam moves uninterrupted by air molecules, maintaining a clear image. The final image is typically monochromatic (black, white, or grey) and can be digitally stored in formats like JPEG or TIFF.

The image's brightness and contrast depend on the specimen's density. Dense areas scatter more electrons, creating darker regions, while thinner areas allow more electrons through, appearing brighter. This sequential process allows TEM to produce highly detailed images of specimens at the atomic or molecular level.[142]

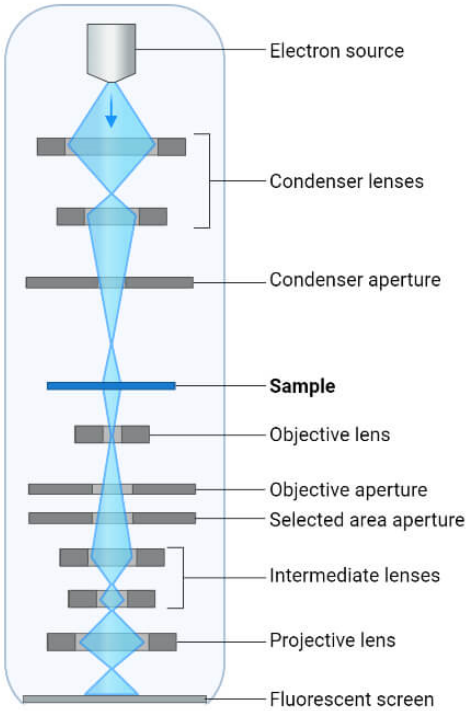

Figure 2.6. Schematic diagram of a TEM: illustrating the process where a finely focused beam of electrons is directed onto the sample by the condensing lenses. The transmitted electrons are focused and magnified by the objective lens, further magnified by the intermediate lenses, and finally projected onto a fluorescent screen by the projector lens.[141]

In this project, samples were prepared by drop-casting a 20 µL solution onto a standard 3 mm copper mesh grid with a continuous lacey carbon-coated film. The suspension solutions were prepared by mixing 50 µg of TeNWs into 1 mL of ACS-grade water and 50 µL solution of P3HT-TeNWs into 1mL of chlorobenzene. The mixtures were thoroughly vortexed for 2 minutes using a vortex mixer to ensure uniform dispersion of the nanowires. The grids were allowed to dry naturally for about 1 hour before being loaded into the TEM. The grid samples were placed on a standard low-background TEM double tilt holder. TEM images were acquired using Titan 80-300 keV and Tecnai G2 80-200 keV TEMs (Thermo Fisher Scientific, Waltham, MA, USA; formerly produced by FEI), equipped with a 4096×4096 pixel^2 OneView CMOS camera (Gatan, Inc., Pleasanton, CA, USA). The TEM images were processed using Digital Micrograph (DM) and the open-source ImageJ software to enhance contrast and brightness.

2.3.5 Scanning Transmission Electron Microscopy (STEM)

A Scanning Transmission Electron Microscope (STEM) is an advanced electron microscope that combines features of both Scanning Electron Microscopy (SEM) and Transmission Electron Microscopy (TEM). It is commonly used to study materials at the atomic scale, providing high-resolution images and detailed insights into the structure, composition, and properties of a sample. A STEM system, as illustrated in Figure 2.7, operates by generating a finely focused electron beam, typically less than 1 nm in diameter, using an electron gun. The beam is then focused through a series of electromagnetic lenses and scanned across the sample in a point-by-point raster pattern (like how SEM works).

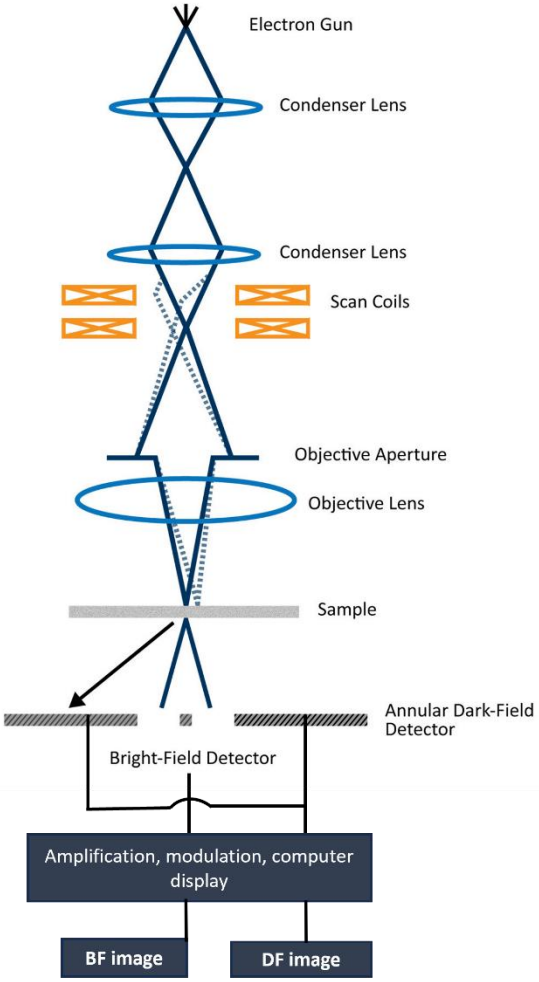

Figure 2.7. Schematic of Scanning Transmission Electron Microscope. The finely focused electron beam, generated by the electron gun, passes through a series of magnetic lenses, and is transmitted through the sample. The signals from the transmitted electrons are detected by bright-field and dark-field detectors, producing corresponding high-resolution images.[143]

As the electron beam passes through the sample, which must be very thin (usually less than 100 nm), it either transmits through or scatters depending on the material's structure. Different signals are generated based on this interaction, and the most common signals in STEM are bright field (BF), annular dark field (ADF), and high-angle annular dark field (HAADF).

Detectors positioned below or around the sample capture these transmitted or scattered electrons. The BF detector collects electrons that pass straight through the sample without scattering, highlighting denser regions with high contrast. The ADF detector captures electrons scattered at wide angles, which is useful for imaging heavier elements and atomic structures. The HAADF detector collects highly scattered electrons, enabling atomic-scale imaging and compositional analysis. These signals are processed to create high-resolution images of the sample, with atomic-level resolution.[143]

2.3.6 Focused Ion Beam (FIB)

Focused ion beam (FIB) cross-sectioning of the drop-casted nanowires was performed using a Zeiss Crossbeam 540 equipped with a carbon gas injection system (GIS) and a gallium (Ga) ion source. Three amorphous carbon layers were sequentially deposited onto the nanowires: a 20 nm layer via pre-sputtering outside the FIB chamber, a 50 nm layer using an electron beam, and a 700 nm layer using an ion beam. The Ga ion beam was employed for FIB lamella preparation. Final polishing of the sample was done using a 30 kV, 50pA probe, followed by cleaning with a 5 kV, 10pA probe. In this project, FIB on our samples was conducted in Nanyang Technological University (NTU) of Singapore.

2.3.7 X-ray Photoelectron Spectroscopy (XPS)

X-ray photoelectron spectroscopy (XPS) is a robust surface analysis technique employed to identify and quantify the elemental composition within few nanometres (~ 5nm) depth of a sample's surface. The underlying principle of XPS involves a single-step process called as photoemission, where an electron bounded in an atom of the sample is knocked out by a photon of monochromatic x-ray source, such as Al K_α or Mg K_α. The process is illustrated in Figure 2.8. The emitted electron is called as photoelectron, and the kinetic energy of the photoelectron is specific to the element it originated from. By analysing the position and intensity of peaks in the XPS energy spectrum, the chemical state, and the quantity of elements in the sample can be determined.[144]

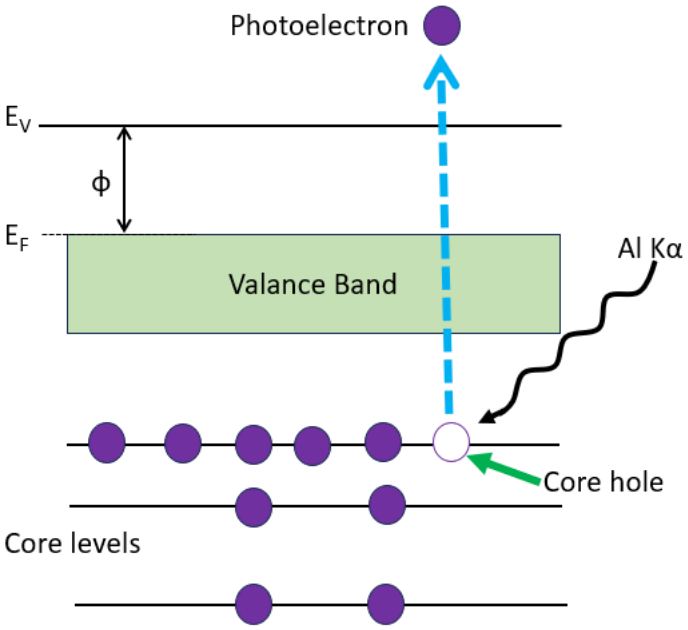

Figure 2.8. Schematic of Photoemission Process. E_V, ϕ, E_F, are the vacuum level, work function, and Femi level of the element, respectively.

In this project work, XPS spectra were obtained by employing an AXIS Supra spectrometer (Kratos Analytical, UK) equipped with a hemispherical analyzer and a monochromatic Al Kα source (1487 eV) operated at 15 mA and 15 kV. The XPS spectra were collected over an analysis area of 700×300 μm^2 at a take-off angle of 90°. Survey scans were performed at a pass energy of 160 eV, while high-resolution scans were conducted at a pass energy of 20 eV. Charge compensation was managed using low-energy electron flooding. The instrument is in Nanyang Technological University (NTU) of Singapore. Data deconvolution was executed using Casa XPS software.

2.3.8 Photoelectron Spectroscopy in Air (PESA)

Photoelectron Spectroscopy in Air (PESA) is a technique used to measure the ionization potential (IP) (or HOMO for organic materials) of materials in open air. It can be applied to a variety of materials, including organic semiconductors and thin films. Figure 2.9 shows the energy level diagrams of different solid-state materials, which provide the theoretical background for how PESA measures the IP.

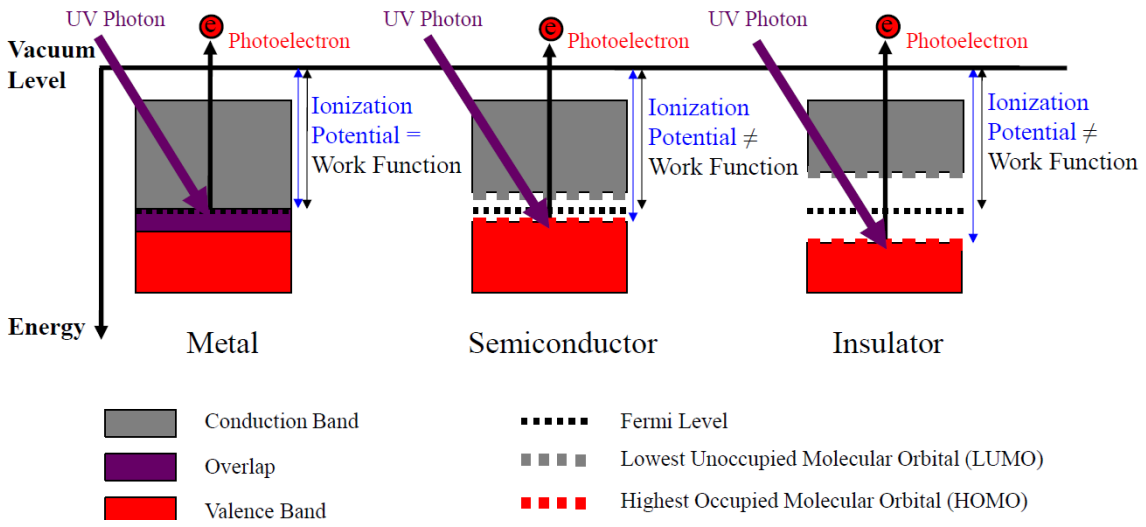

Figure 2.9. Schematic of Energy level diagrams of metal, semiconductor, and insulator.[145]

The work function is the minimum energy required to move an electron from the Fermi level to a vacuum. The ionization potential, on the other hand, is the energy difference between the vacuum level and the highest occupied molecular orbital (HOMO). In metals, the Fermi level is within the conduction band, meaning the band is partially filled. For insulators, electrons in the valence band are separated from the conduction band by a large gap. Semiconductors have a smaller gap between these bands, which can be crossed by thermal or other excitations. The PESA works by shining ultraviolet (UV) or low-energy photons onto the sample, which excites electrons in the material as shown in the Figure 2.10.

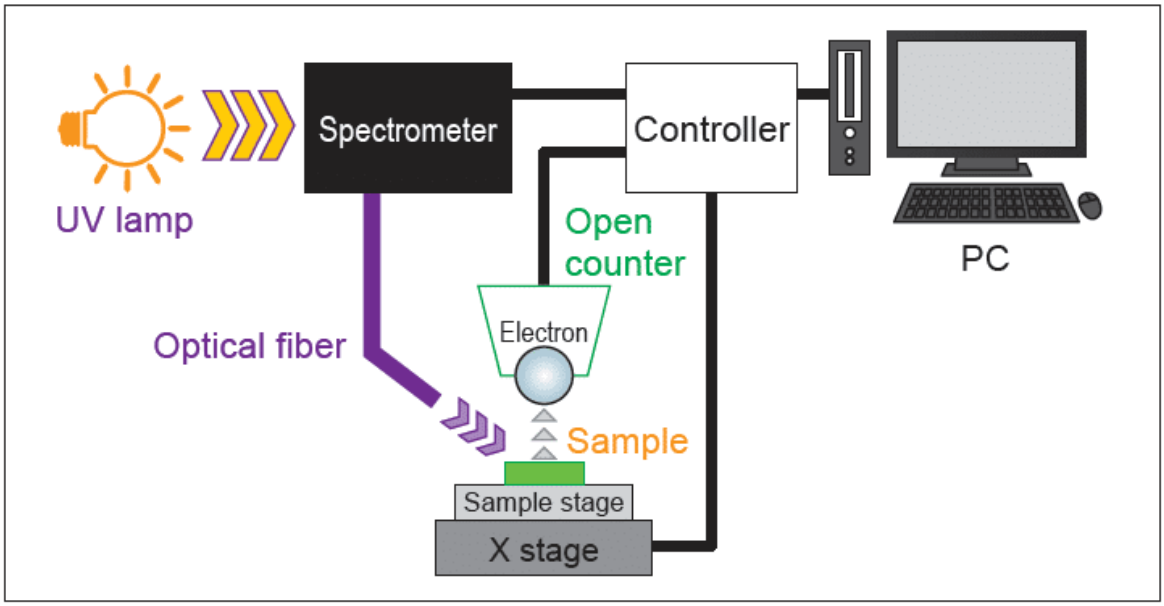

Figure 2.10. Configuration diagram of Photoelectron Spectroscopy in Air (PESA) system.[146]

If the photon energy exceeds the material's work function, electrons are ejected from the surface into the air. An open counter or detector, such as a collector electrode or electron multiplier,

captures the emitted electrons and measures the current generated by these emitted electrons (the number of electrons emitted is proportional to the photon energy). By analysing the photon energy and electron emission data, the ionization potential of the material is determined. The photoemission threshold energy at which electron emission begins corresponds to the ionization potential of the material.[145,147]

In this project, Riken Photoelectron Spectrometer AC-2 was used to measure the ionization potential with the following settings: start energy at 4.20 eV, end energy at 6.00 eV, and energy steps of 0.05 or 0.10 eV. The UV intensity was set to 250. This instrument is located at IMRE-A*STAR in Singapore.

2.3.9 Kelvin Probe Microscopy

The Kelvin probe is a non-contact, non-destructive tool used to measure the work function of a material by detecting the difference in surface potential between the probe (tip) and the sample. Since the work function is determined by the top 1-3 layers of atoms or molecules, the Kelvin probe is highly sensitive to surface characteristics. To understand how Kelvin probe measurements work, the energy levels of both the sample and the tip/probe are shown in schematic diagrams of Figure 2.11.

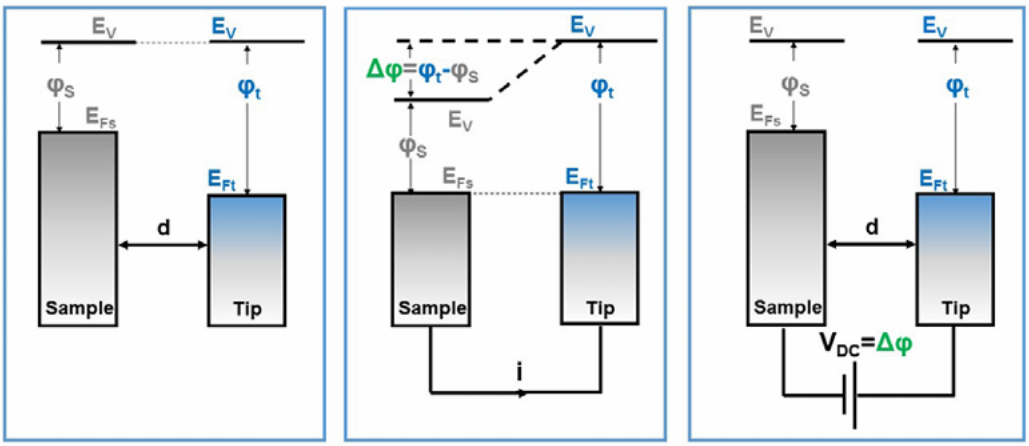

Figure 2.11. Principle of Kelvin Probe Measurements. Where (E_{FS}, ϕ_S) and (E_{Ft}, ϕ_t) are the respective Fermi level and work function of sample and tip/probe, E_v the vacuum level. Adopted from ref.[148]

When the sample and tip/probe are far apart, their Fermi levels are different, but their vacuum levels (E_v) are the same. The work function is the difference between each material's Fermi level and its vacuum level. When the probe and sample are connected, electrons flow from the sample to the probe, causing their Fermi levels to align. This creates a distortion in the vacuum levels, called the contact potential difference (V_{CPD}), which is the difference between the work functions of the

sample and the probe. To measure the work function of the sample, the Kelvin probe applies a bias voltage to the probe until the current between probe and the sample is zero, effectively cancelling out the vacuum level difference. At this point, the applied bias voltage is equal to the V_{CPD}, and this value is recorded. The work function of the sample is calculated by comparing the V_{CPD} of the sample with that of a reference material (typically a known metal, like gold). The difference in V_{CPD} directly correlates with the work function of the sample being tested.[145,149] In this project, the work function was measured using a KP Technology APS02 Kelvin Probe system, with untreated ITO (work function = 4.7 eV) serving as the reference. The instrument is at the School of Chemistry, University of Oxford, London.

2.3.10 Ultraviolet Visible Spectroscopy (UV- Vis)

UV-Vis spectroscopy is one of the most commonly used techniques for analysing a wide range of organic compounds and some inorganic species. This method measures the intensity of light in the ultraviolet (UV, 10-400 nm) and visible (VIS, 400-800 nm) regions as it passes through a sample, depending on the wavelength (nm).[150] When a compound absorbs light of specific wavelengths, the amount of light absorbed is measured, producing a spectrum that reflects the interaction of electromagnetic radiation with the compound in the UV-Vis region.[151] The wavelength and the amount of light absorbed depend on the compound's molecular structure and its concentration. As the concentration of the compound increases, more light is absorbed, while less light is transmitted. This relationship follows Beer's Law:[151]

$$A = log_{10} {}^{I_0}/_{I} = \varepsilon bc \qquad \text{Equation 16}$$

Where A is the light absorbance (no units), I is the light intensity after passing through the samples, I_0 is the reference light intensity, $\boldsymbol{\varepsilon}$ is the molar absorptivity (L/mol cm), b is the path length of the sample, that is the path length of the cuvette in which the sample is contained (typically in cm), and c is the concentration of the compound in solution (mol L^{-1}). When an organic molecule is exposed to light, it absorbs a specific wavelength, causing its electrons to jump from a lower energy level (HOMO - highest occupied molecular orbital) to a higher unoccupied energy level (LUMO - lowest unoccupied molecular orbital). The energy of the absorbed light corresponds to the energy gap (ΔE) between the HOMO and LUMO levels. This process is illustrated in Figure 2.12.

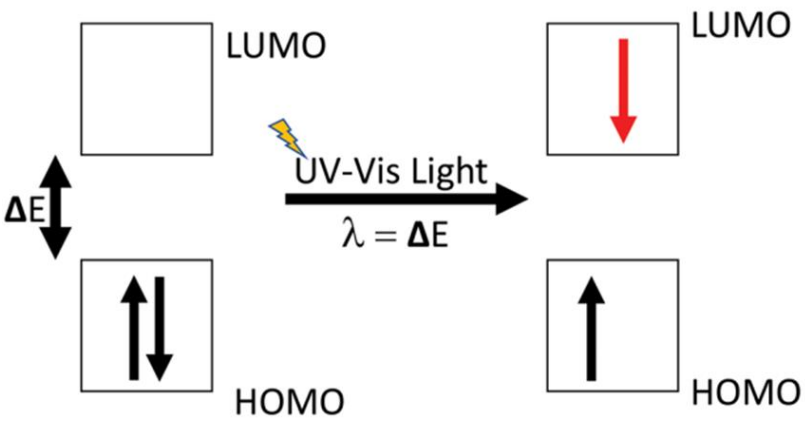

Figure 2.12. A schematic presentation of molecular orbitals and energy gap when the electrons are excited from HOMO to LUMO levels with the incident light wavelength (energy) equal to the energy gap.[151]

The absorbed wavelengths either do not appear or appear at reduced intensity in the detected spectrum. The amount of light absorbed is usually expressed as percent transmission and absorbance. Transmission, represented by I/I_0, is the fraction of light that reaches the detector after passing through the sample, and percent transmission is calculated as $100 \times (I/I_0)$. Absorbance is a logarithmic scale of I_0/I, which increases as transmission decreases.

For our UV-Vis spectroscopy experiments, we used a Shimadzu UV-3600 UV-VIS-NIR spectrophotometer at IMRE, A*STAR Singapore, with a baseline range of 300 - 3300 cm^{-1}. The data were collected using UV-Probe 2.33 software. P3HT thin films were prepared on quartz substrates, and dilute solutions of nanowires were placed in quartz cuvettes for the UV-Vis measurements.

2.4 Transport Properties Measurements

2.4.1 Room Temperature Seebeck Coefficient and Electrical conductivity measurements

The room temperature Seebeck coefficient of thermoelectric thin films was measured using a Portable Thermoelectric Meter (PTM-3, Joule Yacht), as shown in the Figure. 2.13 (a). In this setup, the red band probe functions as a heat source and the blue band probe as a heat sink, creating a temperature gradient (ΔT) of 25°C between the hot and cold probe ends. The company recommends that probe spacing on the sample should be no less than 5 mm, as results below this threshold may be unreliable. The temperature difference induces a potential difference across the material under test, which is recorded as the Seebeck voltage (V/K). The Seebeck coefficient is displayed on the screen with a positive or negative sign, indicating the behaviour (p-type or n-type) of the material under test. The probes were positioned at four different locations on the sample to measure the Seebeck coefficient in four distinct areas, and the average of these measurements was

taken as the final Seebeck value (S). Nevertheless, PTM-3 device was calibrated using a reference nickel foil (S ~ 19 μVK^{-1}) provided by the manufacturer. This reference was routinely measured to ensure the calibration of the system, with results compared to previous readings to confirm they fall within the manufacturer's specified 7% relative error. Consequently, all Seebeck coefficient measurements have an uncertainty of 7%.

Figure 2.13. Room Temperature Transport Properties Measurements (a) Portable Thermoelectric Meter for Seebeck coefficient measurements, (b) Keithley Source meter-2450 with four-point probe, (c) magnified 4-probe indicating current source on outer probes while inner two-probe for voltage.

The room temperature electrical conductivity measurements were conducted using a standard four-point probe setup with a Keithley 2450 source meter as shown in Figure 2.13 (b) &(c). After acquiring the I-V characteristic curves, the sheet resistance was multiplied by a geometric factor to account for alternative current pathways that deviate from the straight-line path between the four probes, as explained in the literature.[152] The thickness of the fabricated films was measured using an Alpha-Step IQ surface profiler. The films were scratched at the centre with a toothpick and scanned at multiple points to ensure uniform thickness and reproducibility of measurements. This thickness was then multiplied by the sheet resistance to determine the resistivity (ρ). Finally, electrical conductivity (σ) of the films was calculated using the equation:

$$\sigma = 1/\rho \qquad \text{Equation 17}$$

To ensure the results consistency obtained through PTM-3 and four-probe, we compared them with Cryostat Probe station TE measurements at room temperature as detailed in Figure Appendix A.4.

2.4.2 Temperature dependent Thermoelectric Characterisation

2.4.2.1 Fabrication of a pattern-device for measuring the thermoelectric properties of thin films

A patterned microchip used to measure the thermoelectric properties is created using a lithography-free, resistance thermometry-based technique developed by Kumar et al.[153] The microchip device is fabricated by patterning a 7×7mm^2 quartz substrate using a single-step shadow mask technique with 10 nm Ti and 100 nm Au deposition through a Denton Explorer 14® e-beam thermal evaporator. The device design is based on similar structures to those reported in the literature.[75] The device consists of two resistance-based thermometers with four-probe contacts, two heaters, and two additional electrodes for four-probe electrical resistivity measurements. The fabricated elements, including heater, thermometers, and the resistivity gold lines are depicted in Figure 2.14.

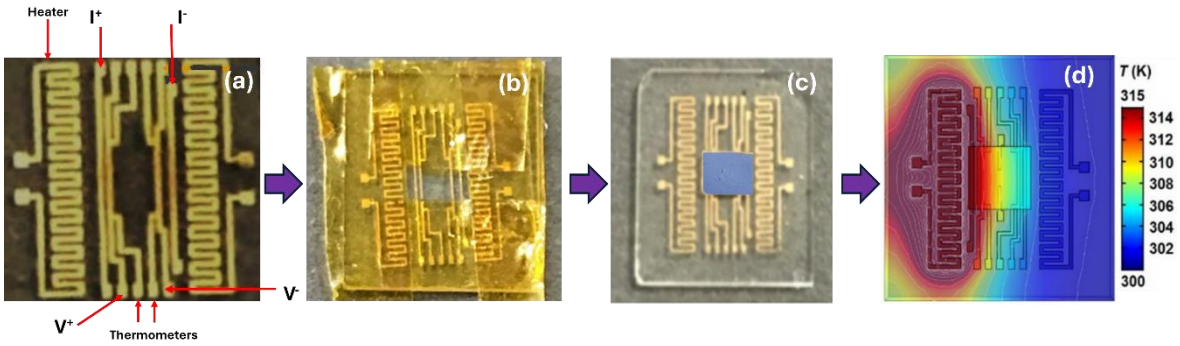

Figure 2.14. An illustration of device fabrication to measure temperature dependent Seebeck coefficient and electrical conductivity. (a) An optical image of the shadow-mask pattern on (7×7) mm^2 quartz substrate, showing two thermometers used to probe the temperature difference across the channel, two heaters, and four-probe electrodes, (b) pattern partially covered with the Kapton tape to avoid electrical shorting with the heater, (c) Thin film deposited via drop casting along the channel, (d) simulation of the temperature gradient along the channel length when current passes through the heater with an underlying quartz substrate. The image is adapted from ref.[153]

The distance between the two thermometers, referred to as the channel length, is about 1 mm. This spacing ensures a to ensure a sufficient in-plane temperature gradient for accurate Seebeck coefficient measurements. The gap between the first resistivity electrode and the heater is 0.2 mm, allowing Kapton tape to cover the heater. This prevents electrical shorting between the film and the heater and facilitates film deposition in the active area. This setup minimizes errors caused by spurious voltage generated from the conduction path outside the electrode region. The active area was prepared by covering the heater with Kapton tape as shown in Figure 2.14 (b). The film was

then deposited in the active area by drop casting, as illustrated in Figure 2.14 (c). It was dried naturally in a nitrogen-filled glovebox and then kept at 100 ^{o}C overnight.

2.4.2.2 Temperature dependent measurements of Seebeck coefficient and electrical conductivity of thin films

The homemade thermoelectric measurement setup used in this thesis is located inside a high-vacuum cryostat at IMRE, A*STAR, Singapore. Temperature dependent measurements can be performed using this setup in both high vacuum (µTorr) and low vacuum (1 mTorr) conditions with high accuracy (<1%). This method has been calibrated using nickel and PEDOT: PSS thin films, and the experimental data matched very closely with literature values of -11.2 µVK^{-1} for nickel and +8.4 µVK^{-1} for PEDOT: PSS at 300K.[153]

In this project, simultaneous temperature-dependent measurements of the in-plane Seebeck coefficient and four-point probe electrical resistivity were performed. The patterned-device with drop-casted thin film is mounted on a 24-pin chip holder using GE varnish. The electrical contacts between the chip holder and the device are established using a West Bond wire-bonder instrument equipped with an aluminium thread. Once the connections to the electrode pads are made, the chip holder is mounted on the sample stage, as shown in Figure 2.15.

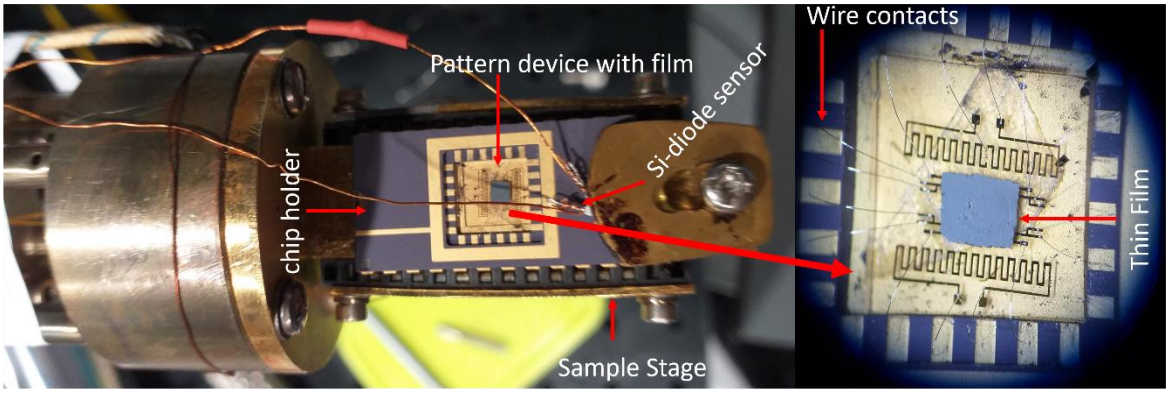

Figure 2.15. The chip holder mounted on sample stage, including a magnified image showing the wire-connections and deposited thin film on patterned-device.

To control the base temperature of device, a Lakeshore 335 controller is utilized with an accuracy of about 30 mK at 300K. A silicon diode sensor is used at the base of the cryostat's second cold stage, serving as the controlled temperature sensor. A silicon diode sensor is positioned at the top of the chip holder to measure the actual temperature of the device.

In the four-probe resistivity configuration, a Keithley 6221 current source passes current to the sample through I^+ and I^- electrodes (shown in Figure 2.14), while a Keithley 2182A nanovoltmeter measures the resistivity voltage between the V^+ and V^- electrodes (Figure 2.14). IV measurements

are performed at different temperatures to determine resistivity. The slope of the IV curves at each temperature provides the resistance value, and the resistivity of the films is calculated using the following relation:

$$\rho = \frac{RA}{L} = \frac{dV}{dI}\frac{wt}{L} \qquad \text{Equation 18}$$

Here, dV/dI represents the slope of the I-V curves, w and t are the width and thickness of the films, respectively and these are experimentally measured using an Alpha-Step IQ surface profilometer, and L is the channel length (the distance between the V^+ and V^-electrodes).

To measure the Seebeck coefficient, both thermometers are calibrated to find the exact temperature gradient across the sample. The thermometer near to heat source exhibits high resistance and referred as hot thermometer, whilst the other one is known as cold thermometer. To obtain the calibration curves (*R vs. T*), a Keithley 2450 sourcemeter supplies current to the heater, generating a temperature difference across the sample length. This temperature gradient alters the resistance of both thermometers, which is measured by two SRS 830 lock-in amplifiers in a four-probe configuration. Figure 2.16 (a) shows the temperature dependent resistance R(T) of both thermometers [R_1 (cold), and R_2 (hot)] for a thin film of S^{2-}TeNWs (sulfur capped tellurium nanowires). The curves were fitted with a linear equation, $R(T) = AT + R_0$, where A and R_0 are the fitting parameters. The value of A (slope) for cold and hot thermometers were found to be 0.03106 Ω/K and 0.03218 Ω/K, respectively. The R-square for both linear fits were almost unity ($R^2 = 0.999$). Figure 2.16 (b) indicates the resistance of both thermometers as a function of the current at room temperature. To determine the temperature gradient across the device, measurements at all temperatures were performed in a similar way. As seen from the resistance vs current (R vs I) plot, the resistance of both thermometers rises parabolically with the increase in current from 0 to 0.015 mA. Therefore, a parabolic fit of equation $R(I) = aI^2 + b$ is performed, as shown in Fig. 2.16 (b) a black line curve for R_1 and a red line curve for R_2. The values of 'a' and 'b' were found as 868.65 ± 35.6 $Ω/A^2$ and 30.0771 ± 0.004 Ω for cold thermometer whilst 558.73 ± 41.34 $Ω/A^2$ and 31.59 ± 0.004 Ω for hot thermometer. The change in resistance (ΔR) of cold and hot thermometers were converted into change in temperature (ΔT) by using the following relation:

$$\Delta T = \frac{\Delta R}{(\frac{dR}{dT})} \qquad \text{Equation 19}$$

Here, ΔR is the change in resistance as a function of current (i.e., heater current) extracted from the R-I curves, and $\frac{dR}{dT}$ is the slope extracted from the R-T curves of both thermometers. The change in temperature as a function of heater current for both thermometers is measured separately for each thermometer, from equation 19.

$$\Delta T_h = \frac{\Delta R_{hot}}{\left(\frac{dR}{dT}\right)_{hot}} \quad \text{Equation 20}$$

$$\Delta T_c = \frac{\Delta R_{cold}}{\left(\frac{dR}{dT}\right)_{cold}} \quad \text{Equation 21}$$

Where ΔT_c and ΔT_h are the resistance change in cold and hot thermometers, respectively. ΔT_c and ΔT_h were found as 3.90646 K and 6.29244 K respectively at 300K for 0.015 mA heating current. The difference between ΔT_h and ΔT_c provides ΔT ~ 2.38598K.

The open circuit voltage (V_{OC}) was measured as function of heater current for different temperatures, using a Keithley 2182A nano-voltmeter. Figure 2.16 (c) shows the V_{OC} dependence with the heater current at room temperature. The V_{OC} also changes parabolically by changing the heater current from 0 to 0.016 mA. The same parabolic fitting is performed for all temperatures. At room temperature, the fitting parameters are determined as a = - 4949162.80 ± 10755.97 μV/A^2 and b = 70.28 ± 1.15 μV for S^{2-}TeNWs thin film. Finally, the Seebeck coefficient of the sample is obtained by calculating the slope of the linear fit of the V_{oc} *vs.* ΔT as shown in Figure 2.16 (d). As the device is connected to chip holder using aluminium wires, therefore, the total V_{oc} is a sum of voltage generated along the sample and along the Al leads, an effect that cannot be ignored when measuring metallic films. The total V_{oc} can be written as:

$$V_{OC} = -S_{Al}(T_0 - T_h) - S_{Sample}(T_h - T_c) - S_{Al}(T_c - T_0) = S_{Al}(T_h - T_c) - S_{sample}(T_h - T_c) = (S_{Al} - S_{sample})\Delta T$$

Hence the Seebeck coefficient of sample is given as follow:

$$S_{sample} = -\frac{V_{OC}}{\Delta T} + S_{Al} \quad \text{Equation 22}$$

Where T_0, T_h, and T_c are the base temperature, hot thermometer temperature, and cold thermometer temperature, respectively. The Seebeck coefficient of aluminium (S_{Al}) in literature is reported as -1.7μV/K at 300K.[154]

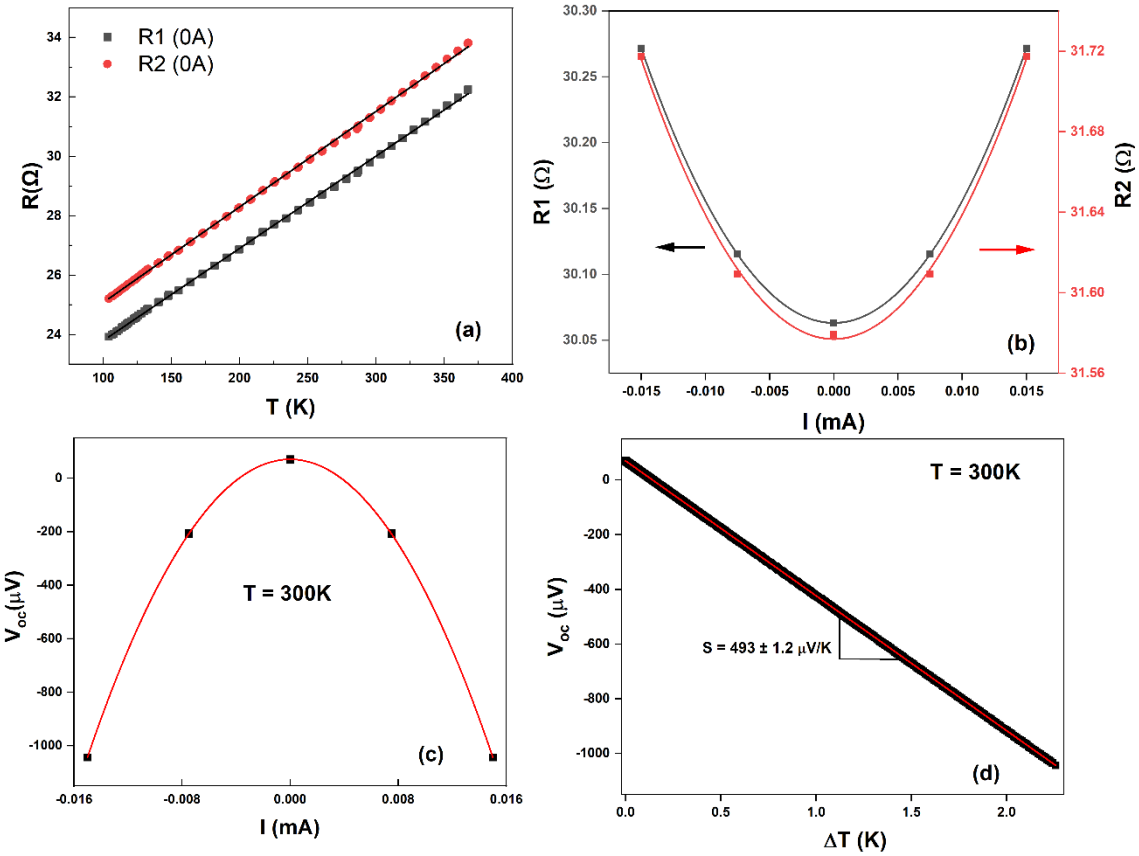

Figure 2.16. (a) Change in resistance of thermometers as a function of temperature for thin film of S^{2-}TeNWs, R_1 is the resistance of cold thermometer and R_2 is the resistance of hot thermometer. The black lines correspond to linear fits. (b) Change in resistance as a function of heater current for both thermometers at 300K. The black and red lines correspond to parabolic fits, for cold and hot thermometers, respectively. (c) Open circuit voltage V_{OC} as a function of heater current I, with red line of parabolic curve fitting. (d) A linear curve fit (red line) is performed to extract the slope from V_{OC} and ΔT to calculate the Seebeck coefficient of S^{2-}-TeNWs film.

Finally, to understand the material response at different temperatures, the temperature dependent S and σ are plotted for the tested samples (S^{2-}TeNWs thin film), as shown in Figure 2.17.

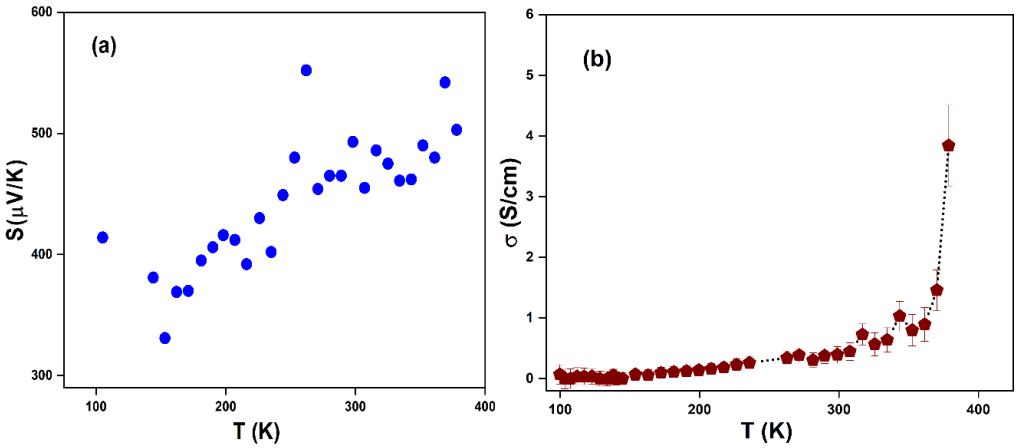

Figure 2.17. Temperature dependent (a) Seebeck coefficient, and (b) electrical conductivity for thin film of S^{2-}TeNWs.

2.4.2.3 Error Analysis

The calculation of the error in electrical conductivity and Seebeck coefficient of thin films of nanowires, polymers, and composites films in this project, is analogous to error analysis carried out by Kumar et al.[153] The error in resistivity is calculated by using the following equation:

$$\delta\rho = \rho * \sqrt{\left(\frac{\delta(R)}{R}\right)^2 + \left(\frac{\delta(w)}{w}\right)^2 + \left(\frac{\delta(t)}{t}\right)^2 + \left(\frac{\delta(L)}{L}\right)^2} \qquad \text{Equation 23}$$

Where, δ indicates the error of the parameters inside the brackets, R is the resistance (IV-slope), w is the width of thin film, t is the thickness of thin film, and L is the channel length (1 mm). As the IV curves are linear so error in R is negligible. The width (w) and thickness (t) of the film are measured through Alpha-Step IQ surface profilometer, which has minimum step height of 1 nm, therefore, the smallest absolute error in thickness (δt) is ~ 1 nm. The channel length (L) is 1 mm and width (w) 2.3 mm which are much larger than the scan resolution of 0.2 µm, hence the error in L and w are negligible. Therefore, the error in resistivity is as follow:

$$\delta\rho = \rho * \frac{\delta t}{t} \qquad \text{Equation 24}$$

The error in Seebeck coefficient comes mostly from error in measuring the temperature difference. Hence the errors in ΔT_c and ΔT_h (shown in equation 20 and 21) are determined by using the following equations:

$$\delta\Delta T_h = T_h * \sqrt{\left(\frac{\delta\Delta R_{top}}{\Delta R_{top}}\right)^2 + \left(\frac{\delta\left(\frac{dR}{dT}\right)_{T_{base.top}}}{\left(\frac{dR}{dT}\right)_{T_{base.top}}}\right)^2} \qquad \text{Equation 25}$$

$$\delta\Delta T_c = T_c * \sqrt{\left(\frac{\delta\Delta R_{bottom}}{\Delta R_{bottom}}\right)^2 + \left(\frac{\delta\left(\frac{dR}{dT}\right)_{T_{base.bottom}}}{\left(\frac{dR}{dT}\right)_{T_{base.bottom}}}\right)^2} \qquad \text{Equation 26}$$

Where $\delta\Delta T_h$ and $\delta\Delta T_c$ are the error in hot and cold side thermometer temperatures, respectively. The errors $\delta\Delta R$ and $\delta\left(\frac{dR}{dT}\right)$ are found from *R* vs. *T* and *R* vs. *I* curve fittings, respectively.

2.4.3 Thin Film Analyser for Thermal Conductivity Measurement

The in-plane thermal conductivity was measured using a LINSEIS Thin Film Analyzer (TFA) employing the 3ω-technique coupled with the Völklien geometry.[155] The LINSEIS TFA is a chip-based platform designed to measure in-plane thermal conductivity (measurement range ~ 0.05 to 200 ± 10% W/m-K) in the temperature range from -170°C to 300°C, and it includes 4-point Van-der-Pauw measurement setup for transport properties measurements (range for electrical conductivity 0.05 to 10^6 ± 6% S/cm, Seebeck coefficient 1 to 2500 ± 7% µV/K), as illustrated in Figure 2.18. To prepare the sample, a shadow mask can be utilized, allowing for deposition via methods such as drop casting, spin coating, ink-jet printing, sputtering or thermal evaporation.

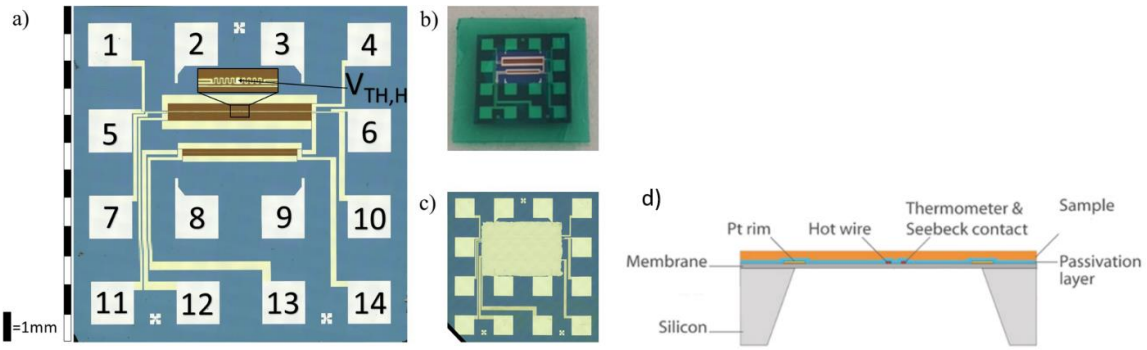

Figure 2.18. TFA chip for transport properties measurement: (a) Front view of the TFA chip designed for 3ω thermal conductivity, 4-point Van-der-Pauw, and Seebeck coefficient measurements. The chip features integrated measurement pads and contacts necessary for precise thermal and electrical characterization. (b) Close-up of the active area on the chip with a shadow mask in place for selective material deposition. This mask ensures accurate patterning and alignment of the deposited material. (c) The sample deposited on the chip, fully prepared for measurement procedures. The precise deposition ensures reliable data collection for thermal and electrical properties. (d) Schematic cross-sectional view of the membrane, illustrating the integrated thermometer used for monitoring temperature variations during measurements, essential for accurate thermal conductivity and Seebeck coefficient analysis. The image is sourced from ref.[155]

The active measurement area of the pre-patterned chips consists of a free-standing silicon nitride membrane with a lithographically defined metal wire running down its centre, shown in Figure 2.18 (d). This metal wire functions as both a thin-film resistive heater and a thermometer. The heat moves from the centre of the membrane towards the edge, facilitating an in-plane measurement of thermal conductivity in the direction perpendicular to the thin-film heater. The manufacturer claims that the TFA method can achieve a repeatability and accuracy of ± 10% in thermal conductivity measurements for most of the materials.

Chapter 3 Oxidation Control and Enhancing the Thermoelectric Performance of Composite Materials

This chapter is based on the manuscript: Syed Zulfiqar Hussain Shah et al., *Adv. Sci.*, **2024**. [DOI: 10.1002/ADVS.202400802].[156]

3.1 Introduction

In recent years, researchers have focused on integrating nanostructured inorganic materials into conducting polymers to design a new generation of organic-inorganic hybrid thermoelectric (TE) materials for converting waste heat into energy. These composite materials are promising for flexible energy-harvesting devices due to their mechanical flexibility and ease of fabrication.[157,158,159] Specifically, combining tellurium (Te) nanostructures with conducting polymers has proven effective in producing stable, processable composites that leverage the strengths of both nanostructure and polymer components. Among various conducting polymers, poly(3,4-ethylenedioxythiophene): poly (styrene sulfonate) (PEDOT: PSS), polypyrrole (PPy), polyaniline (PANI), and poly (3-hexylthiophene) P3HT are particularly suitable for achieving high thermoelectric performance when combined with nanostructured inorganic materials.[160,161,5] For example, Urban and colleagues conducted a pioneering study on Te-PEDOT: PSS composite films, where they performed in situ synthesis of Te nanorods within PEDOT: PSS matrix. These hybrid materials exhibited the combined attributes of the two individual components, with an electrical conductivity of 19 ± 2 S/cm, a Seebeck coefficient of 163 ± 4 μV/K, and a resulting power factor (PF) value of about 71 μW/m-K^2 at room temperature.[105]

Urban's group fabricated hybrid films with different weight ratios (10-90 wt%) of Tellurium (Te) to PEDOT: PSS to investigate how the thermoelectric transport mechanism works in the hybrid system. Among the composites, the composition of Te_{80}-PEDOT:PSS_{20} showed the best performance, achieving a Seebeck coefficient (S) of 179 μV/K, electrical conductivity (σ) of 11 S/cm, and a PF of 35 μW/m-K^2 at 300K.[66] This suggests that charge transport mainly happens through the highly conductive PEDOT:PSS at the interface of the Te-PEDOT:PSS composite. To explore the relationship between electrical and thermal conductivity, they also prepared free-standing core-shell nanowires of Te-PEDOT:PSS and measured how the transport properties changed with the diameter of the nanowires.[65] The results showed that reducing the nanowire diameter decreases thermal conductivity while improving electrical conductivity. This behaviour is explained by the fact that the

inorganic core mainly governs thermal transport, while the organic shell controls charge carrier transport in these organic-inorganic composites. To enhance the thermoelectric properties of Te-PEDOT: PSS, Urban's research team incorporated subphases of copper (Cu) into the Te-PEDOT: PSS matrix, creating a hybrid system composed of Te- $Cu_{1.75}Te$ -PEDOT: PSS nanowires. This approach established two energy barriers at the interfaces between Te-$Cu_{1.75}Te$ and Te-PEDOT: PSS. These barriers selectively scattered low-energy carriers back while allowing high-energy carriers to pass through, leading to an improved Seebeck coefficient and overall better performance of the composites.[162]

Similarly, Deng's team synthesized Te nanorods using a solvothermal method and combined them with the conducting polymer PANI in different weight ratios (10-90 wt%) to study the thermoelectric properties of the resulting Te-PANI hybrid materials.[68] The Te-PANI composites were treated with camphorsulfonic acid (CSA) before being drop-cast onto glass substrates and dried at 333K to form hybrid films. The PANI-Te (70 wt%) composite film showed a maximum power factor of 105 $\mu W/m \cdot K^2$, with an electrical conductivity of 102 S/cm and a Seebeck coefficient of 102 µV/K at room temperature. The team found that the ordered arrangement of PANI chains around the Te nanorods increased carriers scattering while providing a fast channel for carrier's movement, resulting in increasing the electrical conductivity. Whereas the Te nanorods significantly contributed to a high Seebeck coefficient in the hybrid film. Thermoelectric transport properties of some conducting polymer based organic-inorganic composites materials are summarized in Table 3.

Table 3. Thermoelectric performance of organic-inorganic composites at room temperature.

Composites	Electrical conductivity (S/cm)	Seebeck coefficient (μV/K)	Power factor (μW/m-K^2)	Temperature (K)
PEDOT:PSS-TeNWs [66]	11	180	35	R.T.
PEDOT:PSS-TeNWs [163]	500	23.7	29	R.T.
PEDOT:PSS-Bi_2Te_3NWs [67]	1000	45	205	R.T.
PEDOT:PSS-TeNRs [164]	205	83	142	R.T.
PEDOT:PSS-TeNRs [165]	698	383	102	R.T.
PEDOT:PSS-TeNRs [33]	215	115	284	R.T.
PEDOT:PSS-$Cu_{1.75}$Te-TeNWs [162]	17	220	84	R.T.
PEDOT:PSS-TeNWs [166]	21	270	145	R.T.
PANI-Bi_2Te_3 NCs [161]	12	36	0.02	R.T.
PANI-Bi_2Se_3 [167]	30	188	107	R.T.
PANI-TeNRs [68]	102	102	105	R.T.
P3HT-TeNWs [113]	21	67	10	R.T.
P3HT-Bi_2Te_3 NWs [57]	10	117	14	R.T.

The study of polymer/inorganic composites based on P3HT has been quite limited, with only a few reports available in the literature. For example, Ming and colleagues successfully integrated Bi_2Te_3 nanowires (NWs) into P3HT, resulting in a composite with a power factor of 14 μW/m-K².[57] They attributed the high performance of these composite materials to the energy filtering effect. Similarly, Liang et al.[113] developed P3HT-TeNW composites, which exhibited a power factor of 10 μW/m-K² at room temperature. In this case, the electrical transport behaviour was explained using a series and parallel transport model rather than the energy filtering effect.

As can be seen in Table 3, numerous polymer-inorganic composites featuring conducting polymers have demonstrated substantial thermoelectric power factors exceeding 100 $\mu W/m \cdot K^2$. The charge transport in these composite materials has been attributed to interfacial transport, structural and morphological effects, and modifications to the energy dependence of carrier scattering (energy filtering).[57,113,125,168] Recently, Kumar et al.,[128] demonstrated that the enhanced thermoelectric performance observed in these complex hybrid systems can be explained by physical interfacial interactions between the inorganic and organic components, which enhance the Seebeck coefficient and carrier mobility. Experimental evidence suggests that highly ordered morphologies of conducting polymers, facilitated by interfacial interactions with inorganic nanostructures, create highly conductive pathways for charge carriers.[128,66,129,169] However, the inorganic nanostructures are prone to oxidation, potentially affecting the thermoelectric properties of hybrid materials.[170]

A critical review of the literature reveals that previous studies on organic-inorganic hybrid thermoelectric (TE) materials have not fully disclosed the measurement techniques or experimental conditions, leading to uncertainties in the reproducibility and accuracy of the results. These studies have largely overlooked the importance of controlling oxidation during the synthesis of nanowires and composite films, which is crucial for improving the TE performance of hybrid materials. Moreover, the results presented are often single-point values, making them less reliable. To address these gaps, we report for the first time that controlling oxidation during nanowire synthesis and composite film fabrication can significantly enhance charge transport and TE performance in hybrid composites. As a result, our oxidized-hybrid system demonstrated results consistent with those previously reported by Ming[57] and Liang[113] for P3HT-based hybrid composite materials. Whilst the oxidation-controlled hybrid system exhibited a sixfold improvement in TE performance compared to prior reports in the literature.[57,113]

Here we synthesized tellurium nanowires (TeNWs) using the ASS process, as explained in Section 2.1.2. These nanowires were then incorporated into the conducting polymer P3HT through a solution mixing process to create a composite hybrid system, as described in Section 2.1.4. We developed two hybrid systems: TeNWs-P3HT, which used oxidation-controlled nanowires. This

involves the oxidation control during the synthesis of TeNWs and composites by performing all process steps in a nitrogen filled glovebox with O_2 <1ppm, and H_2O <1ppm, doping process, and then thin films packing in membrane boxes and carrying in dry box with a dehumidifier to minimize air-exposure before conducting any characterisation. The second hybrid system of TeO_2NW-P3HT, which used oxidized nanowires. Both these hybrid composite systems were designed to investigate the interfacial interactions and study their thermoelectric transport properties. In this study, we report the enhanced interfacial interaction of Te-P3HT hybrid materials by controlling oxidation. Our results show a significant improvement in the power factor (65 μW/m·K²) of the P3HT-TeNWs hybrid nanocomposites compared to TeO_2NW-P3HT (PF ~ 15 μW/mK²) at room temperature. We demonstrate that precise oxidation control during the synthesis of TeNWs and the preparation of the hybrid film is crucial for optimizing the alignment of P3HT along the TeNWs, thereby improving interfacial charge transport within the composite material.

3.2 Experimental Methods

All the characterisation conducted on thin films of nanowires and composites films along with sample preparation and measurement details are provided in experimental Section 2.3.

3.3 Results and Discussion

3.3.1 Material Characterization

To identify the elemental species and measure the oxidation level within the fabricated thin films, XPS was performed, with the results presented in Figure 3.1. The XPS survey scan spectra (a &b) reveal the presence of tellurium, carbon, and oxygen. All spectra were calibrated using the carbon C 1s peak at 285 eV. Core-level peaks corresponding to Te 3d, C 1s, and O 1s were observed in thin films of oxidized tellurium and oxidation-controlled tellurium nanowires. The O 1s peak around 530 eV corresponds to TeO_2, originating from an oxidised TeNWs surface.[171] High-resolution O 1s spectra are shown in Figure 3.1. (e). Peaks centered at binding energies of 573 eV and 583 eV are attributed to the Te $3d_{5/2}$ and Te $3d_{3/2}$ core levels, respectively, indicating the metallic state of tellurium.[172]

In Figure 3.1 (c), peaks at 576 eV and 586 eV indicate an oxidized surface of tellurium NWs with 45 atomic percent oxygen content within a depth of 5 - 10 nm of the film.[173] Figure 3.1 (d) shows that the oxygen content is reduced to 12 atomic percent at the surface of the NWs prepared by oxidation control within same depth. The peak around 401 eV is identified as the sole nitrogen peak, possibly resulting from the use of hydrazine hydrate as a reducing agent during synthesis. Moreover, since

the samples were prepared on Si substrates, characteristic peaks at binding energies around 100 eV and 151 eV are attributed to Si 2p and Si 1s, respectively.[174]

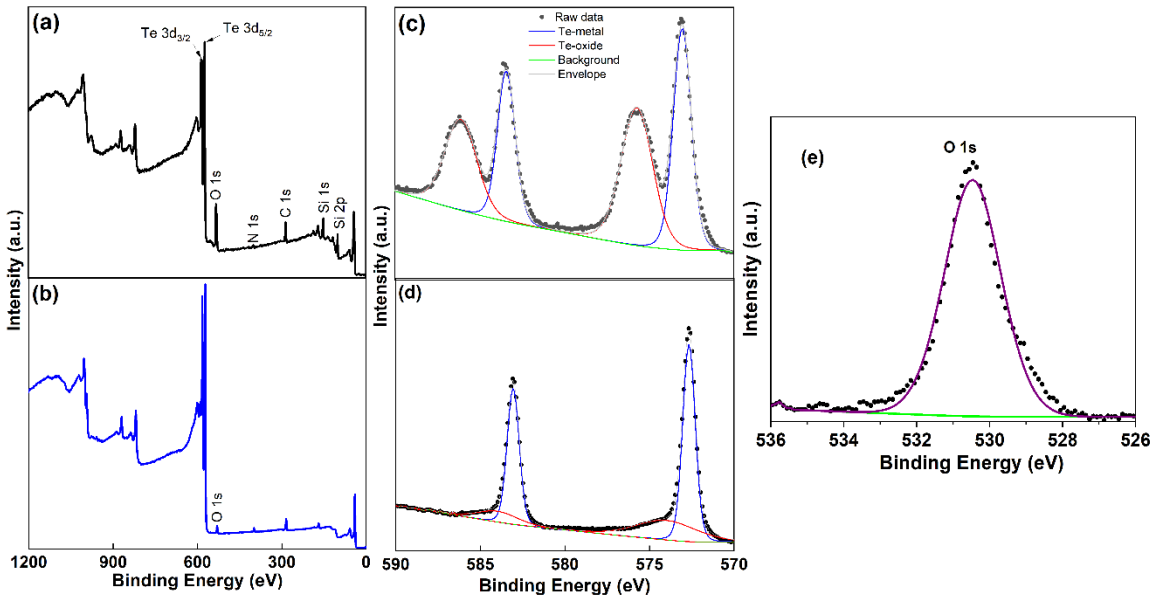

Figure 3.1. High- resolution X-ray photoelectron spectroscopy (XPS) spectra of oxidized TeNWs and oxidation control TeNWs films: Survey scan and XPS core level spectra of Te 3d of highly oxidized TeNWs (a & c), Oxidation controlled TeNWs (b & d), and core level O 1s spectra (e), respectively.

To investigate the microstructure of nanowires (NWs) and the oxygen content on their surfaces, we first dispersed the NWs in ethanol and deposited them onto a silicon substrate via drop-casting. The sample was then carbon-coated, and a cross-section was prepared using focused ion beam (FIB) cutting. Transmission electron microscopy (TEM) was utilized to characterize the sample, as illustrated in Figure 3.2. Low-magnification TEM images of TeNWs shown in Figure 3.2 (a & b) exhibiting random distribution of the TeNWs on a Si substrate and morphology of individual NWs. Most of the TeNWs, when observed in cross-section, exhibited a hexagonal shape with flat facets or edges, and were free from contamination or oxidation. The core of the TeNWs is single crystalline

with little number of defects or dislocations indicated with *white arrows in* Figure 3.2 (b) *and* (c).

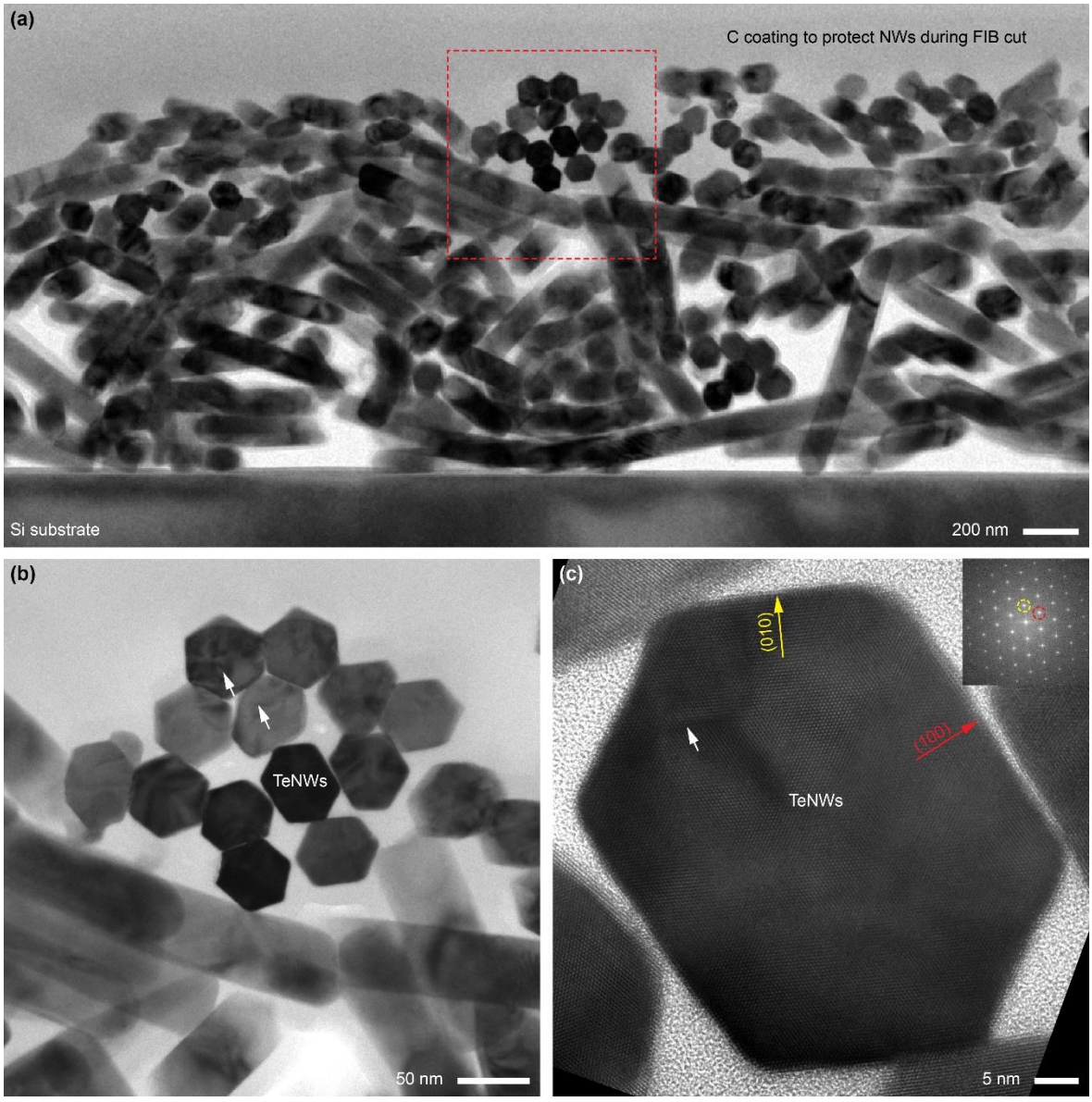

Figure 3.2. Cross-section of TeNWs: (a-b) Low-magnification TEM images of TeNWs showing random distribution of NWs and morphology of individual NWs. (c) High-resolution cross-section TEM image of a single TeNW showing the hexagonal shape of NW bounded by the six (1 0 0) facets confirmed by the lattice fringes and corresponding FFT (inset in (c)). The core of the NWs is single crystalline with minimal defects or dislocations (*white arrows in* (b) *and* (c)).

To compare TeNWs and oxidized Tellurium nanowires (TeO_2 NWs), TEM images are provided in Figure 3.3 (also see Appendix A). An oxide layer formation on the NWs is evident, which introduces more defects in the core of the NWs as shown with white arrows in Figure 3.3 (b). The interfacial layer between two nanowires is shown in Figure 3.3 (c). This interfacial layer is crystalline and appears to be TeO_2, likely due to surface oxidation. Notably, oxide regions not near to the NW surface appear amorphous, whereas the interfacial oxide appears polycrystalline.

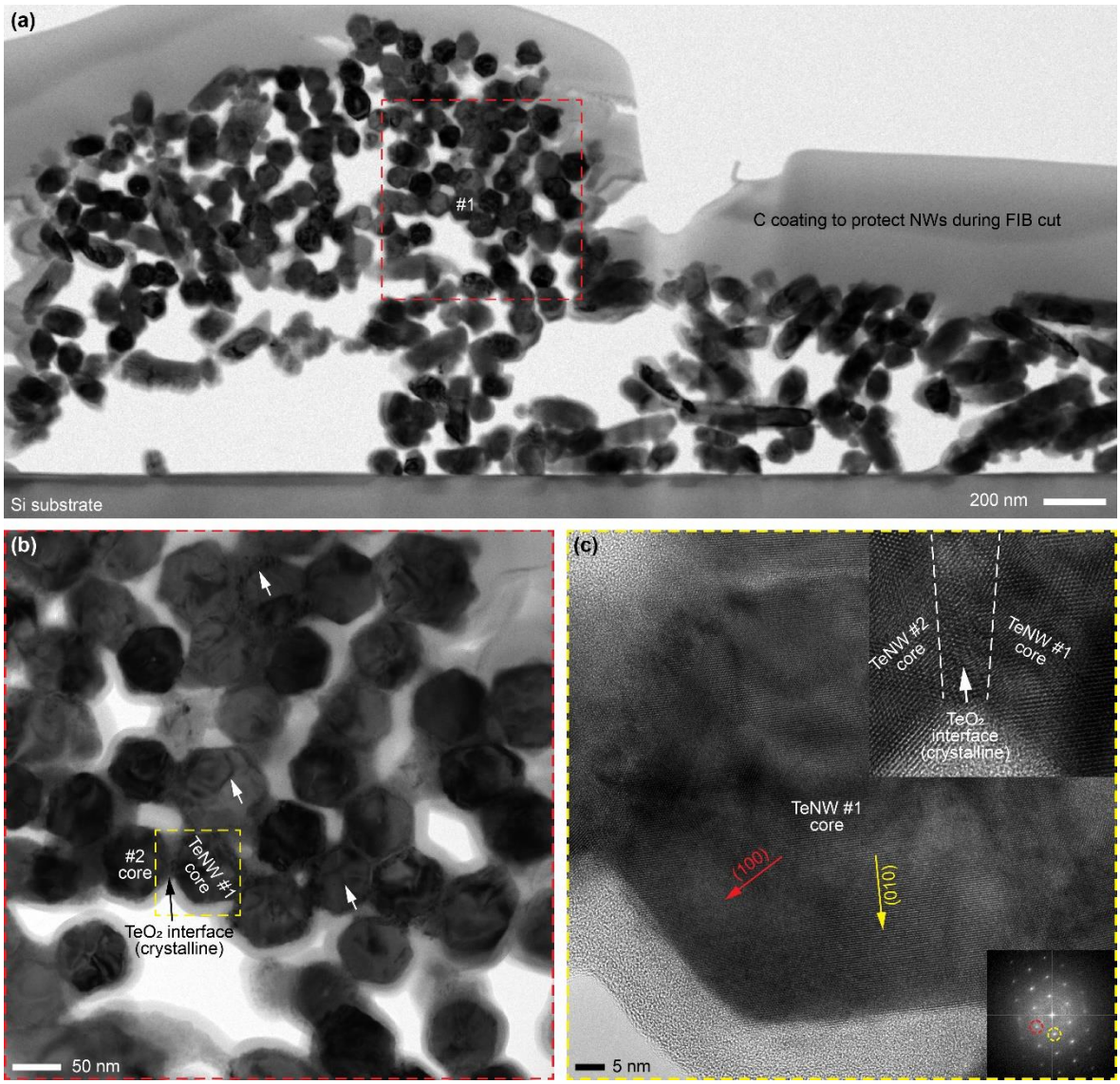

Figure 3.3. Cross-section of TeO_2 NWs: (a-b) Low-magnification TEM images of TeO_2-NWs showing the random distribution of NWs on a Si substrate and morphology of individual NWs. (b) Demonstrates that the oxide formation introduces more defects in the core of nanowires (*white arrows*). (c) High-resolution cross-section TEM image of TeNWs core and the interface layer between the two NWs.

Furthermore, to measure the oxygen content at the nanoscale, Scanning Transmission Electron Microscope (STEM) imaging and Electron Energy Loss Spectroscopy (EELS) mapping with a probe size of approximately 1 nm (in both techniques) were employed. No oxygen traces were detected in the Te-NWs [Figure 3.4(a)], whereas the nanowires in Figure 3.4(b) clearly exhibited the presence of oxygen around their edges (indicated by green colour maps) and an overall increase in the oxygen signal in the spectra [Figure 3.4(c)]. This indicates surface oxidation of the Te-NWs. A detailed examination of the overlay maps and line-profiles obtained for the nanowire shown in Figure 3.4(d) reveals that the core of the nanowire is free from oxidation in both Te-NWs and TeO_2-NWs, with oxidation occurring only on the surface of the TeO_2-NWs.

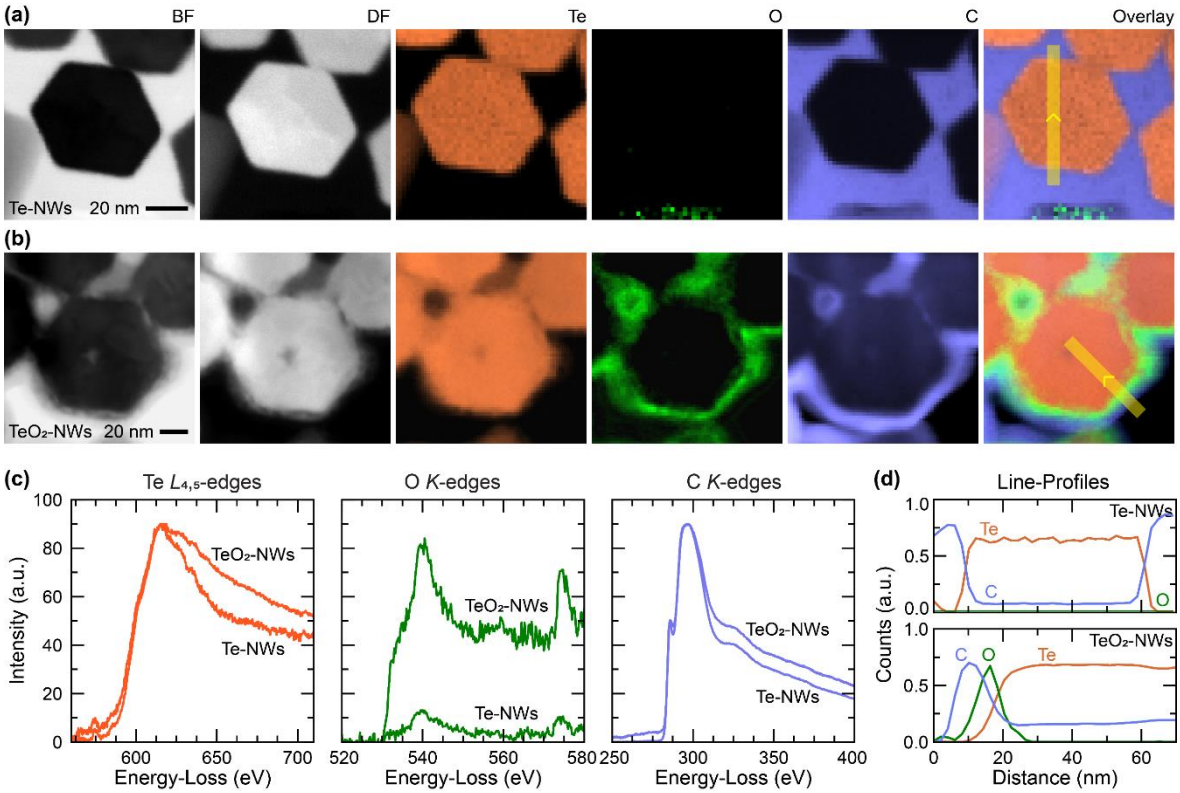

Figure 3.4. Scanning Transmission Electron Microscope (STEM) imaging and Electron Energy Loss Spectroscopy (EELS) mapping to measure the oxygen content in oxidized TeNWs and oxidation controlled TeNWs. Bright-field (BF), dark-field (DF) STEM images, corresponding elemental (Te, O, C) EELS maps, and overlay (Te + O + C) maps of the (a) Te-NWs and (b) TeO_2-NWs in cross-section. (c) Te $L_{4,5}$-edges, O *K*-edges, and C *K*-edges for the two cases extracted from the spectral image. (d) Averaged and normalized line-profile across the nanowire marked with the yellow strips in (a & b). No oxidation was observed on the surface of controlled oxidation TeNWs while a thin layer of oxidation was seen on oxidized TeNWs.

3.3.2 Fabrication and Structural Characterization of Composite Films

Homogenous suspensions of nanocomposites, containing varying concentrations of TeNWs within a P3HT matrix, were drop-casted onto quartz substrates, as detailed in section 2.2.1. Optical micrographs of the composite hybrid films shown in Figure 3.5 (b, d, f, & h) revealed uniform thin films with thicknesses ranging from 5 to 12 µm, with lower concentrations of Te nanowires (NWs) producing thicker films. Scanning electron microscopy (SEM) imaging demonstrated homogeneous dispersions of Te NWs within the P3HT matrix across all NW concentrations, only 60 wt% to 90 wt% composite films are shown in Figure 3.5 (a, c, e, & g).

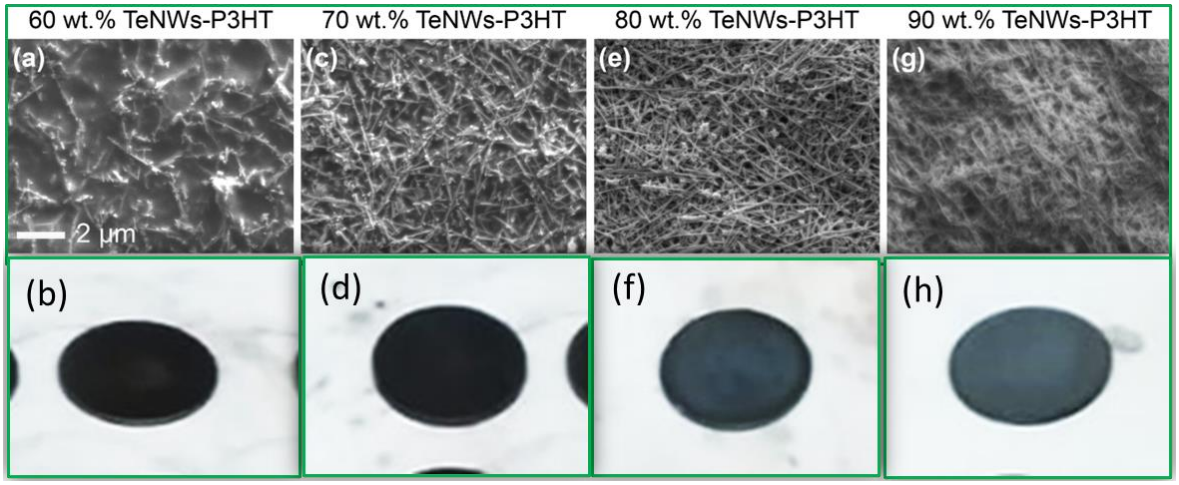

Figure 3.5. SEM and Optical images of P3HT-TeNWs composite hybrid films, using varying concentration of TeNWs in P3HT matrix (a & b) 60 wt%, (c & d) 70 wt%, (e & f) 80 wt%, and (g & h) 90 wt%. Scale bar in SEM imaging is 2µm.

To investigate the microstructure of the nanowires and the polymer coating, high-resolution transmission electron microscopy (HR-TEM) combined with selected area electron diffraction (SAED) were employed and the results are shown in Figure 3.6. TEM images of individual TeNWs and P3HT-TeNWs nanowires demonstrate that their microstructures are identical, featuring a uniform conformal polymer (P3HT) coating approximately 5 nm thick on the nanowire surfaces. HR-TEM images, along with SAED analysis, confirm that the nanowires are single crystalline, with their c-axis consistently aligned along the length of the nanowires, exhibiting an interplanar spacing of ~ 0.59 nm corresponding to the (001) reflection.

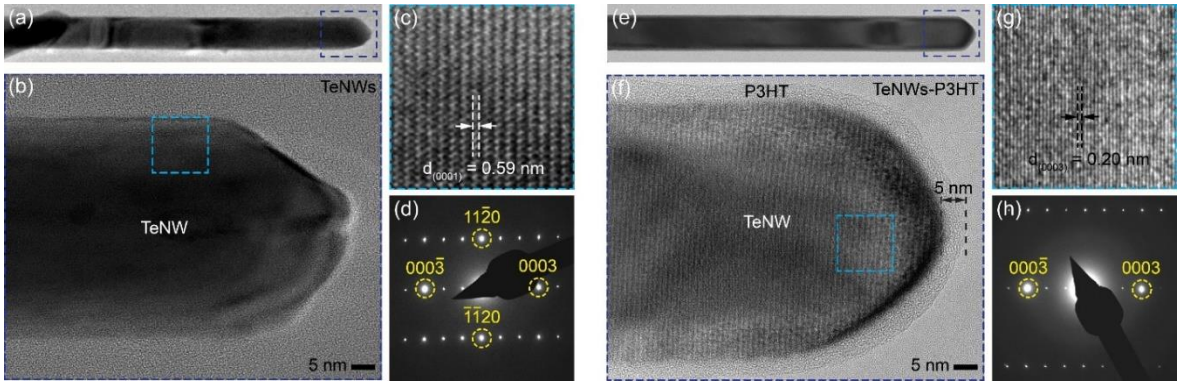

Figure 3.6. High resolution TEM and selected area electron diffraction (SAED) of individual TeNW and P3HT coated TeNW. High-resolution TEM images showing the morphology of individual NWs of (a-c) TeNWs and (e-g) P3HT-TeNWs with a uniform conformal coating of the amorphous polymer (P3HT) layer on the surface of the nanowire. Selected area electron diffraction pattern of a single (d) TeNWs and (h) P3HT-TeNWs.

3.3.3 Thermoelectric Characteristics of Composite Films

The hybrid films composed of varying weight percent (wt%) ratios of NWs (TeNWs and TeO_2NWs) and P3HT, were immersed in a 30 mM $FeCl_3$ solution for doping before measuring their TE transport properties, as shown in Figure 3.7. For both hybrid systems (P3HT-TeNWs and P3HT-TeO_2NWs), it is observed that Seebeck coefficient increases monotonically with an increasing concentration of NWs (cf. black and red arrows in Figure 3.7a). In P3HT-TeNWs hybrid films, the Seebeck coefficient ranges from 18 ± 1 μV/K to 529 ± 4 μV/K as the TeNWs concentration increases from 0 to 100%. The electrical conductivity (cf. blue arrows) initially rises from ~ 11 S/cm to ~ 34 S/cm as the TeNWs content increases from 0 to 60 wt%, then stabilizes at ~ 20 S/cm (70-90% TeNWs), and finally declines to ~ 0.02 S/cm at 100% TeNWs. A similar trend is observed in the TeNW-PEDOT: PSS system.[66] For the P3HT-TeO_2NWs hybrid system, conductivity (cf. magenta arrows) initially increases with NWs content, reaching ~ 35 S/cm at 30 % NWs, but drops to ~ 5 S/cm as NWs content further increases to 90 %. Figure 3.7(b) displays the power factor as a function of NW content for P3HT-TeNWs (wine circles) and P3HT-TeO_2NWs (blue circles) hybrid systems. The power factor for the doped P3HT-TeNWs hybrid system increases from 0.34 μW/mK^2 (0% TeNWs) to 50 μW/mK^2 (90% TeNWs), while for P3HT-TeO_2NWs hybrid system, it rises from 0.34 μW/mK^2 (0% TeNWs) to ~ 15 μW/mK^2 (80% TeO_2NWs).

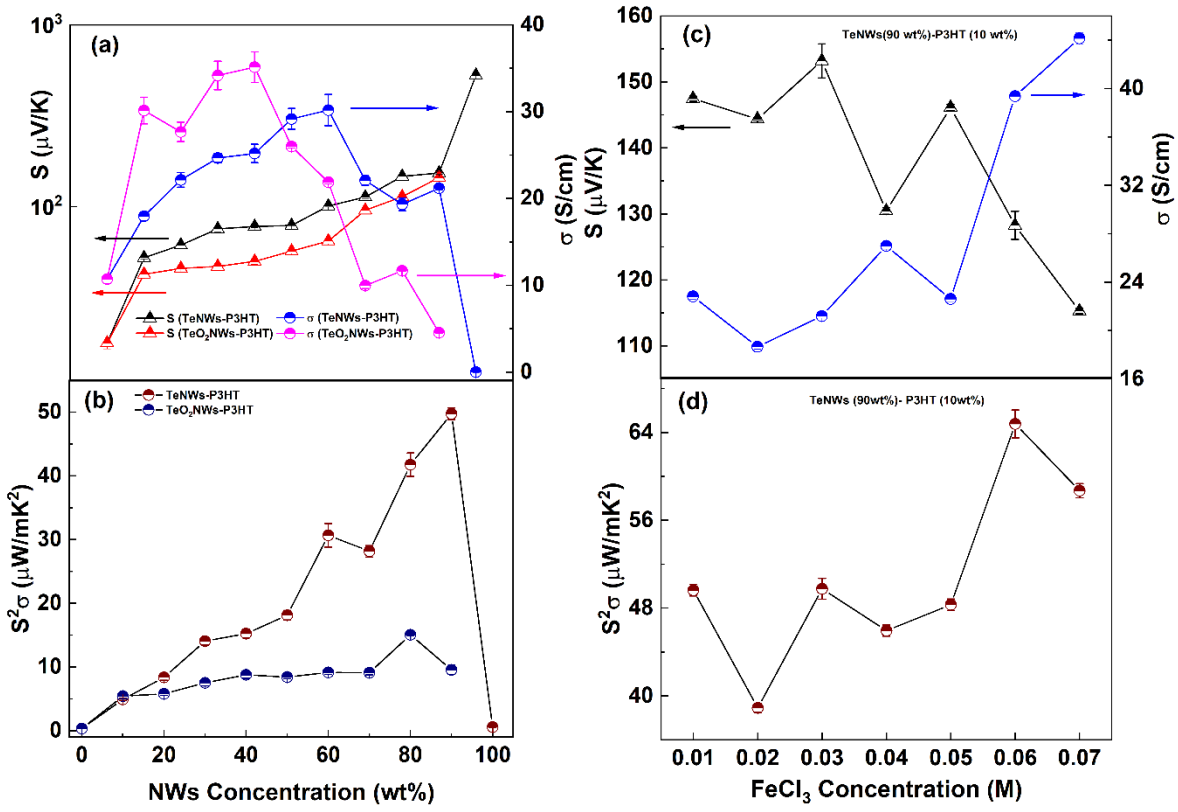

Figure 3.7. Thermoelectric properties of P3HT-based inorganic (TeNWs & TeO_2NWs) hybrid systems as a function of TeNWs content and dopant concentration. (a) Electrical conductivity

and Seebeck coefficient & (b) power factor of 30 mM $FeCl_3$ doped hybrid films in relation to the weight ratio of NWs in the P3HT matrix, ranging from 0 wt% to 100 wt%. (c) Electrical conductivity and Seebeck coefficient & (d) power factor as a function of $FeCl_3$ dopant molar concentration for P3HT-TeNWs hybrid films with 90 wt% TeNWs concentration. Vertical error bars indicate the standard deviation of multiple measurements from the average values for each sample.

To investigate the doping efficiency of the P3HT-TeNWs hybrid system, composite hybrid films [P3HT (10%) - TeNWs (90%)] were immersed in various molar concentrations (0.01 M to 0.07 M) of $FeCl_3$-acetonitrile solutions. The resulting thermoelectric trends are shown in Figure 3.7(c & d). Increasing the dopant concentration introduces more charge carriers at the P3HT-TeNWs interface, enhancing electrical conductivity while decreasing the Seebeck coefficient.[15,175] Figure 3.7(c) shows that the Seebeck coefficient decreases from 148 µV/K to 115 µV/K, while the electrical conductivity increases from 23 S/cm to 44 S/cm as the dopant concentration changes from 0.01 M to 0.07 M. This enhances the power factor of the hybrid films, reaching a maximum value of 65 $\mu W/mK^2$ at 0.06 M, as shown in Figure 3.7(d). These results suggest that incorporating nanowires within a conducting polymer matrix can effectively enhance the power factor of nanocomposite hybrid materials at an optimal doping level with a suitable dopant concentration.

3.3.4 Kang-Snyder Charge Transport Model

To study charge transport in the P3HT-TeNWs hybrid system, the Kang-Snyder CT model was used, as detailed in Section 1.6.4. The Seebeck coefficient and electrical conductivity data of Te_{90}-$P3HT_{10}$ composite hybrid system was collected through de-doping experiments. During this process, the sample was heat-treated at 50°C to gradually remove the dopant, resulting in a decrease in electrical conductivity. As anticipated, the Seebeck coefficient increased as the conductivity decreased. The power factor was observed to decrease gradually with the reduction in electrical conductivity as shown in Figure 3.8 (a).

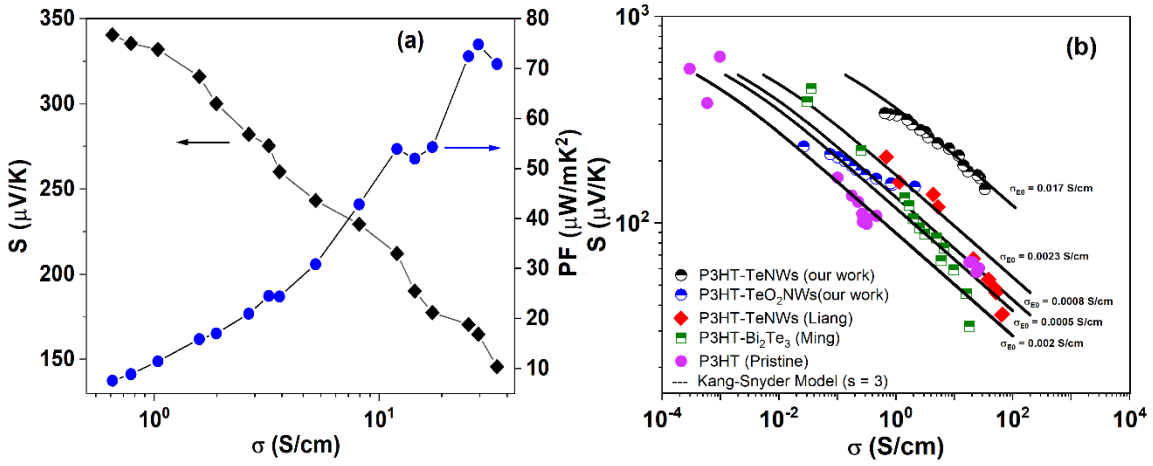

Figure 3.8. The Kang-Snyder charge transport (CT) model applied to P3HT based nanocomposite hybrid systems. (a) The experimental thermoelectric data of 60 mM $FeCl_3$ doped P3HT-TeNWs hybrid system (b) The electrical conductivity (σ) vs Seebeck coefficient (S) data of P3HT-TeNWs (black half-filled circles) from this work, TeO_2NWs-P3HT (blue half-filled circles) from this work, P3HT-TeNWs (red filled squares, Liang), Bi_2Te_3-P3HT (Olive half-filled squares, Ming), and pure P3HT (magenta circles). Our experimental data lies on the energy dependent scattering parameter s = 3 curve with energy independent transport parameter σ_{E0} = 0.017 S/cm.

The Kang-Snyder model was applied to various composite systems based on the P3HT conducting polymer, as illustrated in Figure 3.8 (b). The figure depicts the Seebeck as a function of the electrical conductivity for different systems: P3HT-TeNWs [black half-filled circles, this work], P3HT-TeO_2NWs [blue half-filled circles, this work], P3HT-TeNWs [red filled squares, Liang et al.],[113] Bi_2Te_3-P3HT [olive half-filled circles, Ming H. et al.],[57] and pure P3HT [magenta circles].[127] The experimental data for all hybrid materials exhibit an energy-dependent scattering parameter of s = 3. The fitting process of data with the Kang and Snyder CT model for different values of "s" is shown in Appendix A.6. For our P3HT-TeNWs hybrid system, σ_{E0} was found to be 0.017 S/cm, which is an order of magnitude higher compared to the P3HT-TeNWs hybrid system reported in the literature. To explain this increased σ_{E0} and the observed conductivity trend, molecular dynamics (MD) simulations were performed. These simulations revealed that P3HT aligns preferentially on a pristine Te surface rather than on a TeO_2 surface. This effective templating on the Te surface leads to the higher σ_{E0} value compared to the TeO_2 hybrid system.

We now discuss the trends in Seebeck coefficient and electrical conductivity as a function of TeNWs content. Notably, while the Seebeck coefficient increases monotonically, the electrical conductivity of the films exhibits a peak with increasing Te content in our hybrid films. Standard binary models in the literature cannot explain these non-monotonic trends in Seebeck coefficient and electrical

conductivity.[176] N. E. Coates proposed a series-connected model for these hybrid materials, which includes a highly conductive layer between the Te nanowires and the polymer matrix, accurately describing the observed trends in Seebeck coefficient and electrical conductivity. [66] We have further demonstrated using MD simulations (see Appendix A.5) that this highly conductive interfacial layer arises due to a strong templating effect at the interface. Thus, the total conductivity of the TeNW-P3HT hybrid can be expressed as:

$$\sigma_{eff}^{-1} = x_{Te}\,\sigma_{Te}^{-1} + x_{interface}\,\sigma_{interface}^{-1} + x_{P3HT}\,\sigma_{P3HT}^{-1} \qquad \text{Equation 27}$$

where σ_{eff} is the conductivity of the hybrid material, x_{Te} is the fraction of TeNW, σ_{Te} is the conductivity of the Te nanowires, $x_{interface}$ is the fraction of the interfacial component, $\sigma_{interface}$ is the conductivity of the interfacial layer, x_{P3HT} is the P3HT matrix fraction, and σ_{P3HT} is the matrix conductivity. Seebeck coefficient can be written as:

$$S = \frac{x_{Te}S_{Te}\sigma_{Te} + x_{interface}S_{interface}\sigma_{interfeace} + x_{P3HT}S_{P3HT}\sigma_{P3HT}}{\sigma_{eff}} \qquad \text{Equation 28}$$

At lower TeNW content (<10%), the P3HT matrix dominates transport, resulting in similar power factor values for both P3HT-TeNW and P3HT-TeO_2NW hybrid materials. As the nanowire content increases, the templating effect and charge transfer between the NWs and the P3HT interface also increase. The templating effect enhances mobility at the interface, while charge transfer at the interface induces de-doping, which increases the Seebeck coefficient of the interface layer. Both these factor controls the conductivity and Seebeck coefficient trend in P3HT-TeNW and P3HT-TeO_2NW hybrid materials as discussed in Table 4.[128,66]

Table 4. Summary of physical phenomena contributing to thermoelectric trends at P3HT-TeNWs and P3HT-TeO_2NWs interface.

	Templating effect	De-doping due to Charge transfer at interface	Seebeck and conductivity	Discussion
P3HT	X	X	x	
P3HT-TeNWs (10%-60%)	$\mu(\uparrow)$	$n_{de-doping}(\downarrow)$ $S_{de-doping}(\uparrow)$	$\sigma = n_{de-doping}(\downarrow) \times e \times \mu(\uparrow)$ $S(\uparrow) \propto \frac{1}{n_{de-doping}(\downarrow)}$	Conductivity increases due to Strong templating compared to reduction in carrier concentration; Seebeck coefficient increases due to charge transfer induced de-doping at interface. Strong templating take over carrier concentration reduction to improve the conductivity
P3HT-TeNWs (70%-90%)	$\mu(\uparrow)$	$n_{de-doping}(\downarrow)$ $S_{de-doping}(\uparrow)$	$\sigma = n_{de-doping}(\downarrow) \times e \times \mu(\uparrow)$ $S(\uparrow) \propto \frac{1}{n_{de-doping}(\downarrow)}$	Conductivity stays constant due to comparable *n* reduction rate and templating effect; Seebeck increases due to charge transfer induced de-doping.
P3HT-TeO_2NWs (10%-40%)	$\mu(\uparrow)$	$n_{de-doping}(\downarrow)$ $S_{de-doping}(\uparrow)$	$\sigma = n_{de-doping}(\downarrow) \times e \times \mu(\uparrow)$ $S(\uparrow) \propto \frac{1}{n_{de-doping}(\downarrow)}$	Conductivity increases due to templating compared to reduction in carrier concentration; Seebeck coefficient increases due to charge transfer induced de-doping at interface. Templating take over carrier concentration reduction to improve the conductivity
P3HT-TeO_2NWs (40%-90%)	$\mu(\uparrow)$	$n_{de-doping}(\downarrow)$ $S_{de-doping}(\uparrow)$	$\sigma = n_{de-doping}(\downarrow) \times e \times \mu(\uparrow)$ $S(\uparrow) \propto \frac{1}{n_{de-doping}(\downarrow)}$	Conductivity drops due to stronger *n* reduction rate as observed in charge transfer section in DFT and weak templating effect; Seebeck increases due to charge transfer induced de-doping.

3.4 Conclusions

In summary, this study demonstrates that surface doping of organic-inorganic composite materials and oxidation control during nanostructure synthesis significantly enhance thermoelectric performance due to strong templating effects. To explore this, we synthesized tellurium nanowires (TeNWs) under two conditions: one with controlled oxidation (TeNWs) and another with intentional oxidation (TeO_2NWs).

X-ray Photoelectron Spectroscopy (XPS) analysis revealed that the TeO_2-NWs contained 45 at% oxygen, while the oxidation-controlled TeNWs had significantly reduced surface oxygen content of 12 at%. TEM studies revealed that oxidation-controlled samples exhibited no oxidation, while oxidized samples showed amorphous oxidation layers.

We then developed two hybrid systems by blending these nanowires with P3HT polymer: one using oxidation-controlled TeNWs (TeNWs-P3HT) and another using oxidized TeO_2NWs (TeO_2NWs-P3HT). SEM images showed both hybrids formed uniform films, and TEM confirmed a smooth polymer coating on the nanowires. We doped both systems with 0.03M $FeCl_3$ dopant and measured their thermoelectric properties.

The oxidized hybrid (TeO_2-NWs-P3HT) achieved a power factor (PF) of ~ 15 μW/m-K^2, electrical conductivity (σ) of ~ 12 S/cm, and a Seebeck coefficient (S) of ~ 114 μV/K at room temperature. Whilst, oxidation-controlled hybrid (TeNWs-P3HT) showed significantly better performance, with a PF of ~ 50 μW/m-K^2, σ of ~ 21 S/cm, and S of ~ 153 μV/K.

By varying the molar concentration (10 - 70 mM) of the $FeCl_3$ dopant, we optimized the doping efficiency, which may enhance transport properties and engineer the interface between the polymer and nanowires to improve charge transport in composites. Consequently, we achieved the highest reported performance for P3HT-based inorganic hybrid composites ($TeNWs_{90}$-$P3HT_{10}$), with a power factor of 65 ± 2 μW/mK^2 along with electrical conductivity (σ) of 39 ± 0.4 S/cm, Seebeck coefficient (S) of 128 ± 2 μV/K, with 60 mM $FeCl_3$ doping at room temperature. Molecular dynamics (MD) simulations confirmed that the P3HT polymer aligned more effectively with the TeNWs surface than with oxidized surfaces (TeO_2), thereby enhancing charge transport.

In conclusion, optimising surface doping and controlling oxidation during the synthesis of organic-inorganic composite materials proves to be effective strategies for significantly enhancing thermoelectric performance. The strong templating effects achieved through these methods improve charge transport and thermoelectric performance (PF) in hybrid materials. This work introduces a promising pathway for advancing thermoelectric materials and optimizing their performance for practical applications.

Chapter 4 Impact of Surface Passivation on Nanowires

This chapter is based on the manuscript: Syed Zulfiqar Hussain Shah et al., *ACS Appl. Mater. Interfaces,* **2024**. [DOI: 10.1021/acsami.4c02469][177]

4.1 Introduction

The key properties of Te nanowires (TeNWs), including a high Seebeck coefficient and low thermal conductivity (0.16 W/m-K),[81] are crucial for maintaining high thermoelectric efficiency, making TeNWs a promising material for thermoelectric devices. However, nanostructured materials synthesized via solution-based methods often exhibit low electrical conductivity. One reason to this reduced conductivity is largely due to the presence of bulky, long-chain insulating ligands, such as polyvinylpyrrolidone (PVP), attached to the surface of the nanostructures. PVP acts as a capping agent during synthesis, influencing the shape of the nanostructures and maintaining their suspension in the solvent. It is well known that removing residual PVP is challenging due to its adhesive properties.[18] Ansar et al.[178] reported that sodium borohydride solution can be used to disperse the original TeNWs solution and remove residual PVP. However, Luo et al.[179] demonstrated that once sodium borohydride is depleted, the displaced capping agents can quickly re-adsorb onto gold (Au) nanoparticles. To remove these surfactants and obtain a refined product suitable for thermoelectric applications, the energy-intensive process of spark plasma sintering (SPS) is typically employed.

Another factor contributing to the low electrical conductivity of NWs is surface passivation, a chemical process that renders the surface virtually inert. Surface passivation is an unavoidable step in the fabrication of nanowire-based devices. It naturally occurs through oxidation, where an oxide layer forms around the nanowire upon exposure to air, making the surface chemically passive.[180,181] This oxide layer increases the junction resistance between nanowires, leading to reduced electrical conductivity, as noted by Thongkham et al.[182]

It is important to note that the efficiency of charge transport and carrier mobility in nanowires is largely dictated by their surface properties.[183] Imperfections on the surface of nanowires can trap charge carriers, reducing the effectiveness of doping and increasing the likelihood of electron-hole recombination. This results in shorter diffusion lengths, meaning carriers such as electrons or holes travel shorter distances before recombining. Additionally, impurities often occupy positions on or just below the surface of nanowires, making them electrically inactive.[180] Therefore, carefully

controlling the surface properties of nanowires is essential to achieve the desired performance in devices made from these nanostructures.

To overcome the challenges mentioned earlier, modifying the surface of nanowires with suitable ligands is considered to be an effective approach in the literature.[166] Sulfur linkers are particularly effective as they have a strong binding affinity for various chalcogenide-based nanostructures such as Tellurium, Bi_2Te_3, Bi_2S_3, CdSe.[166] Research indicates that S^{2-} ions first penetrate the polymer (PVP) coating on synthesized nanowires and bind to un-passivated tellurium (Te) atoms on the surface. As the concentration of S^{2-} ions increases, the polymer coating is gradually removed, exposing more surface sites for S^{2-} attachment. Under highly doped conditions, the polymer is almost entirely displaced, leaving the nanowire surface fully covered by S^{2-} ions.[134] However, the selection of linkers depends on factors such as the ligand's ability to prevent aggregation of individual nanostructures, enhance dispersion in various solvents, and facilitate the linkage of nanostructures with a chosen polymer. The presence of sulfur ions on the surface of nanostructures, which carry a surface charge, provides stability in polar solvents such as water and hexane. This stability is achieved by preventing aggregation through electrostatic repulsion between individual nanostructures.[47]

To the best of our knowledge, only one report currently describes a chemical solution method for attaching sulfur linkers to tellurium nanowires and encapsulating them in PEDOT:PSS polymer.[166] However, that study did not investigate the effects of surface passivation or the thermoelectric performance of the nanowires after sulfur adhesion. Here, we present for the first time the impacts of sulfur linker attachment on tellurium nanowires, particularly focusing on their thermoelectric performance under varying temperature conditions. It is demonstrated that TeNWs can be readily modified with sulfur linkers, with sulfur displacing the PVP previously present on the TeNWs surface. This surface modification not only improves the dispersion of nanowires in polar solvents but also significantly reduces oxidation of the nanowires, thereby enhancing their thermoelectric performance.

In this study, we used an aqueous solution chemical synthesis method to produce tellurium nanowires (TeNWs). This approach is energy-efficient and allows for precise control of the size and chemical composition of the nanomaterials. The synthesis process is described in detail in Section 2.1.2. After synthesis, we modified the surface of the TeNWs by introducing sulfur linkers (S^{2-} ions) through a brief mixing procedure, as outlined in Section 2.1.3. Both the synthesized TeNWs and the sulfur-modified TeNWs (S^{2-}-TeNWs) were then characterized, and their thermoelectric properties were compared with previously reported results, as detailed in the following section.

In addition to the research on Te-based nanomaterials, significant efforts have been made to combine Te nanostructures with conducting polymers to create hybrid composite materials. These

composites yield a high Seebeck coefficient (>400μV/K) of Te nanostructures whilst also addressing their poor electrical properties by incorporating electrically conductive polymers. Among the most studied polymers for these composites are poly(3,4-ethylenedioxythiophene): polystyrene sulfonate (PEDOT: PSS) and polyaniline (PANI). In a study by S.K. Yee et al.,[104] a composite was fabricated by incorporating PEDOT:PSS into the TeNWs synthesis, followed by drop-casting the mixture onto sapphire substrates, drying under a heat lamp, and annealing at 140 °C for 5 minutes. To enhance the performance of the (TeNWs-PEDOT: PSS) hybrid composite, they doped the PEDOT: PSS solution with 5% dimethyl sulfoxide (DMSO). This modification resulted in a power factor (PF) of 100 μW/m-K^2 at room temperature, which is significantly higher than the PF of the TeNWs, which was less than 2 μW/m-K^2.

Based on this, we encapsulated the synthesized S^{2-}-TeNWs in poly(3-hexylthiophene) (P3HT) to fabricate hybrid composite materials. We then doped these composites with iron trichloride ($FeCl_3$), a p-type dopant, and measured their thermoelectric transport properties. Interestingly, the S^{2-}-TeNWs-P3HT hybrid composites demonstrated improved thermoelectric performance, with a power factor (PF) of about 78 μW/m-K^2, compared to the PF of around 65 μW/m-K^2 observed in our previously reported TeNWs-P3HT hybrid system.[156] This is discussed in more detail in the results and discussion section.

4.2 Methods and Characterisation

The synthesis of tellurium nanowires (TeNWs), their surface modification, composite material fabrication, and thin film fabrication processes are all explained in detail in Section 2.1 and 2.2. Material characterization techniques are described in Sections 2.3, and temperature-dependent transport property measurements are discussed in Section 2.4.2.

4.3 Results and Discussion

4.3.1 Surface Modification of Tellurium Nanowires

To investigate whether as-prepared PVP coated TeNWs could be modified with sulfur linkers, various characterization techniques were utilized. According to Sahu et al. report,[166] the presence of sulfur ions on the surface of NWs facilitates a stable dispersion in polar solvents. To study this effect, Zeta potential measurements were used to compare the dispersibility of as-synthesized TeNWs and sulfur modified TeNWs (i.e., S^{2-}TeNWs). The suspensions of TeNWs and S^{2-}TeNWs were prepared in deionised (DI) water at a concentration of approximately 10 μg/ml. Each solution was transferred into a zeta cell, and measurements were conducted at 25°C. Zeta potentials of -37 mV

for TeNWs and -41 mV for S^{2-}TeNWs were detected, as shown in Figure 4.1, indicating the excellent dispersibility of the nanowires after surface modification with sulfur linkers.

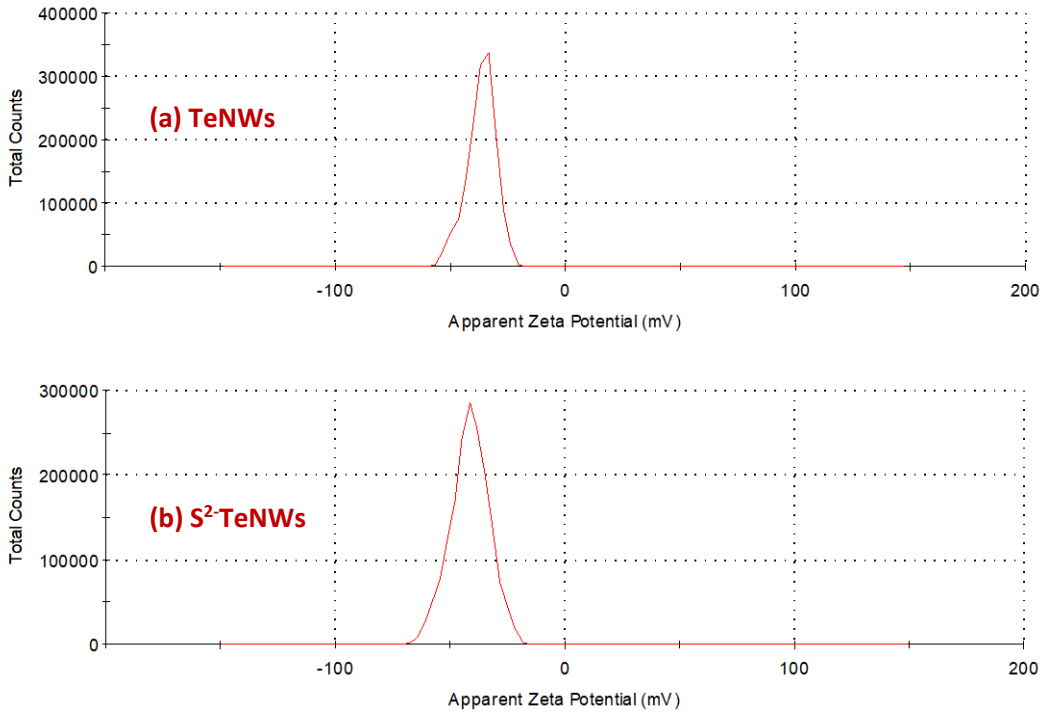

Figure 4.1. Zeta potential measurements for (a) TeNWs and (b) S^{2-}TeWNs.

Owing to their excellent dispersion properties, suspensions of TeNWs and S^{2-}TeNWs were prepared in a 3:2 mixture of isopropanol and ethanol to fabricate thin films. This was followed by 2 minutes of vortex mixing and 1 hour of power sonication. The suspensions were then drop-cast onto silicon (Si) substrates. The samples were then heat-treated at 100 ^{o}C overnight before conducting thin film characterization.

The scanning electron microscope (SEM) images, shown in Figure 4.2, revealed that the thin films of TeNWs and S^{2-}TeNWs were homogeneous and uniform.

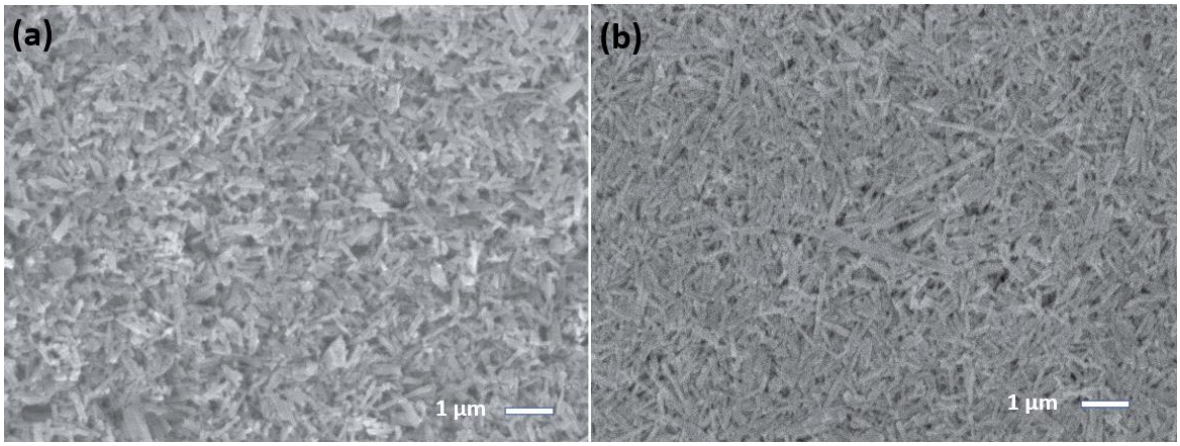

Figure 4.2. SEM images of drop cast thin films on Si substrate (a) TeNWs, (b) S^{2-}TeNWs. Films were fabricated under nitrogen filled glovebox environment with O_2 <1ppm, and H_2O <1ppm.

Although the films were porous, they formed a compact, interconnected network of nanowires. Most importantly, the S^{2-}TeNWs films had a more consistent and smoother surface compared to the bare TeNWs films. To accurately measure the length and diameter of the nanowires, we obtained low-magnification TEM images by dispersing the nanowires onto a standard TEM grid, as shown in Figure 4.3. Details of the sample preparation and measurement method are provided in Section 2.3.4. The measurements revealed that the nanowires ranged in length from 1 to 3 µm, with diameters of 45 - 55 nm for TeNWs and 54 - 62 nm for S^{2-}TeNWs. This indicates that the nanowire diameter increased by approximately 8 nm after sulfur capping. It is likely that the ultrasonication process used before drop-casting the sample onto the TEM grid caused the longer nanowires to break into smaller pieces.

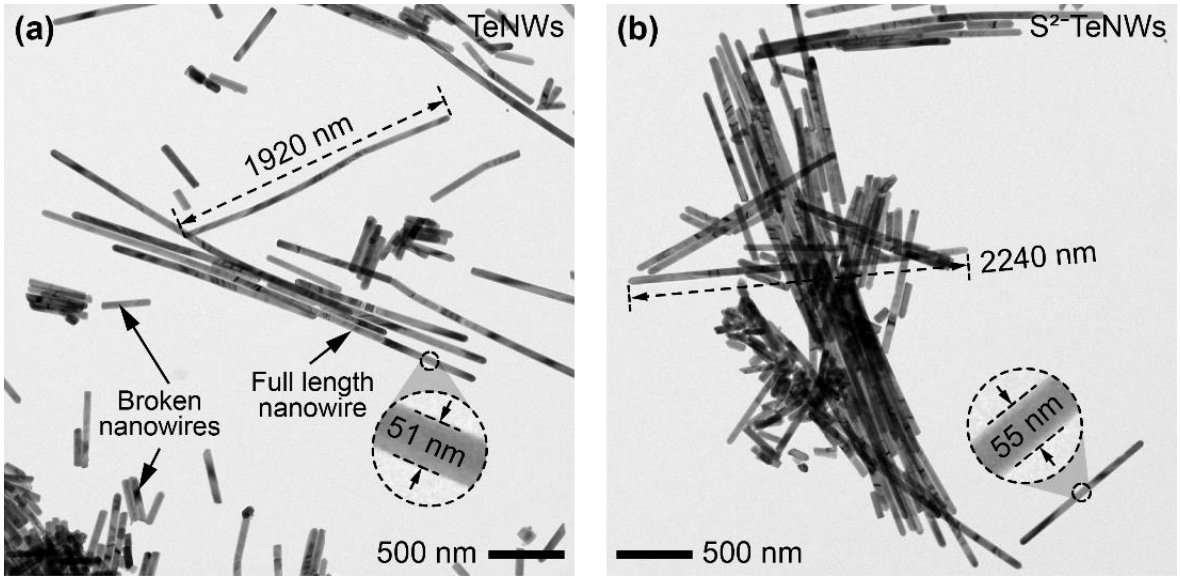

Figure 4.3. Low-magnification TEM images of (a) TeNWs and (b) S^{2-}TeNWs. The images display multiple nanowires, with some appearing broken into smaller segments, likely due to the TEM sample preparation process.

The EDX spectra of TeNWs and S^{2-}TeNWs films, as shown in Figure 4.4, confirm the presence of tellurium and oxygen in both materials.

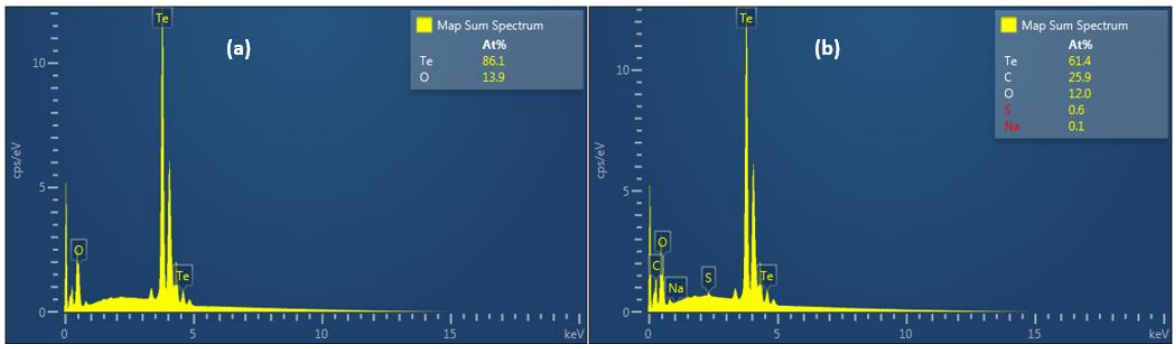

Figure 4.4. EDX analysis of (a) TeNWs (b) S^{2-}TeNWs Films, indicating Te and oxygen contents, also showing a small quantity of S and Na in red colour (i.e., below the detection range) in Figure (b) spectra.

However, the introduction of sulfur moieties decreases the oxygen atomic percentage from 14 at% to 12 at%, suggesting that the incorporation of sulfur into the TeNWs matrix effectively reduces surface oxidation. This is further supported by the X-ray photoelectron spectroscopy (XPS) analysis shown in Figure 4.5.

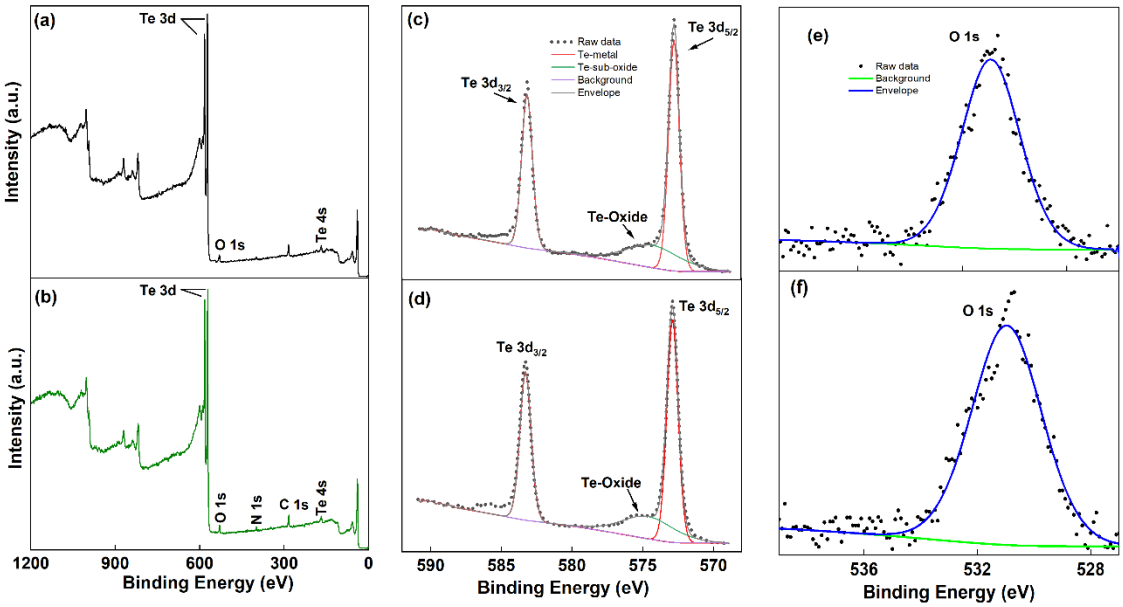

Figure 4.5. XPS spectra of TeNWs and S^{2-}TeNWs films: survey scan (a & b), core level spectra of Te 3d (c & d) and core level spectra of O 1s (e & f).

The XPS results indicate that the nanowires are mainly composed of elemental tellurium, identified by a Te 3d binding energy of 572 eV. The XPS analysis of S^{2-}TeNWs shows no peak around 169 eV, confirming that there is no chemical interaction between tellurium and sulfur. Quantitatively, the XPS data shows that the S^{2-}TeNWs film contains approximately 3 at% sodium (Na), 19 at% sulfur (S), and 29 at% tellurium (Te). Additionally, surface oxidation in the TeNWs films, initially detected at

around 15 at%, was reduced to 10 at% after sulfur passivation within the TeNWs matrix. These findings are consistent with the EDX analysis.

X-rays diffraction (XRD) analysis was conducted on the drop-casted TeNWs and S^{2-}-TeNWs thin films, as shown in Figure 4.6.

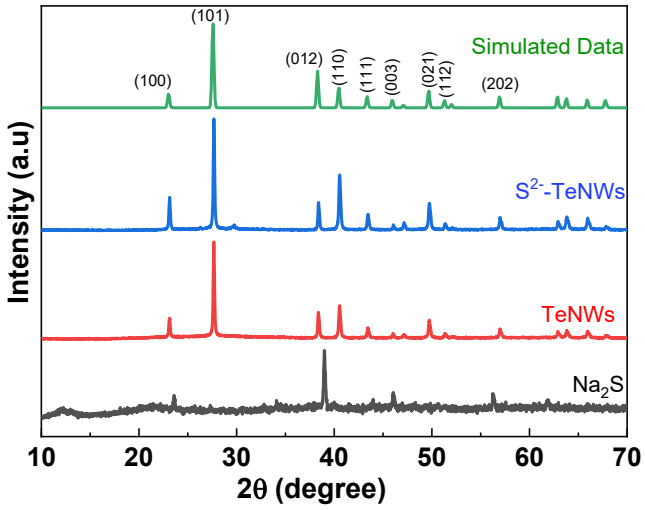

Figure 4.6. X-rays diffraction patterns obtained for, reference of Te from JCPDS card No.36-1452, TeNWs, S^{2-}TeNWs films and Na_2S powder.

The results revealed that the nanowires were composed of Te with a polycrystalline structure, showing a preferred orientation of (1 0 1). The XRD pattern of TeNWs remained unchanged before and after sulfur capping. This indicates that adding sulfur does not significantly alter the tellurium (Te) structure, and the TeNWs in both cases closely match the bulk Te phase as reported in the literature [JCPDS card No. 36-1452].

To confirm that sulfur is only present on the surface of the TeNWs and does not penetrate the bulk, we used high-resolution TEM images and scanning transmission electron microscope – electron energy loss spectroscopy (STEM-EELS) maps. The high-resolution TEM images revealed no change in the lattice parameters, with the measured d-spacing (d_{0001} = 0.59 nm) closely matching that of pristine Te, as shown in Figure 4.7. This suggests that the bulk of the TeNWs remains sulfur-free. Additionally, the Fast Fourier Transform (FFT) analysis of selected regions (Figure 4.7 (c) & (f)) confirms that the nanowires are oriented along the c-axis in both cases.

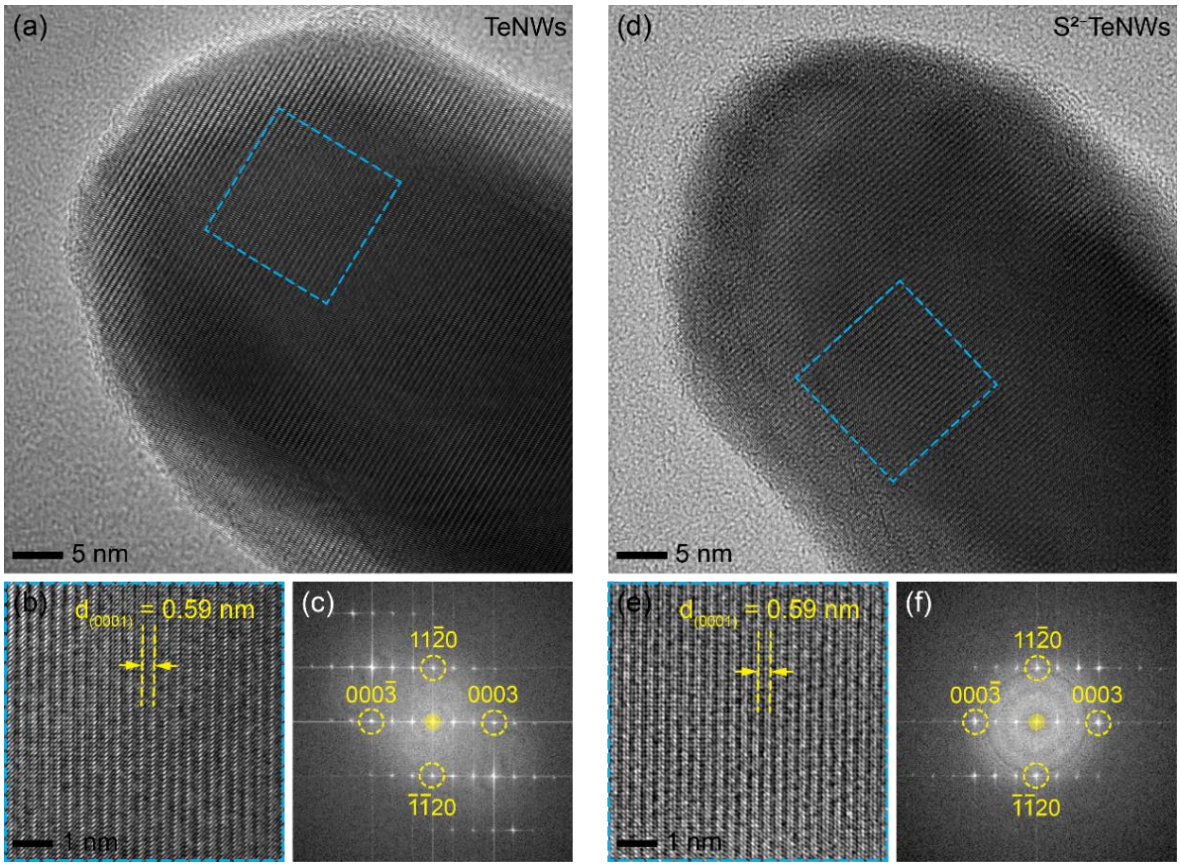

Figure 4.7. High-resolution TEM images of (a) TeNWs and (d) S^{2-}TeNWs, showing the morphology of the NWs. (b & e) A zoom-in section from the selected regions showing lattice fringes. (c & f) Fast Fourier Transform (FFT) of the selected regions showing that in both cases the nanowires are grown along the c-axis with a lattice fringe spacing of 0.59 nm that matches well with reported d-spacing of Te along (001).

To better understand how sulfur is distributed, we obtained STEM-EELS maps for S^{2-}TeNWs (Figure 4.8).

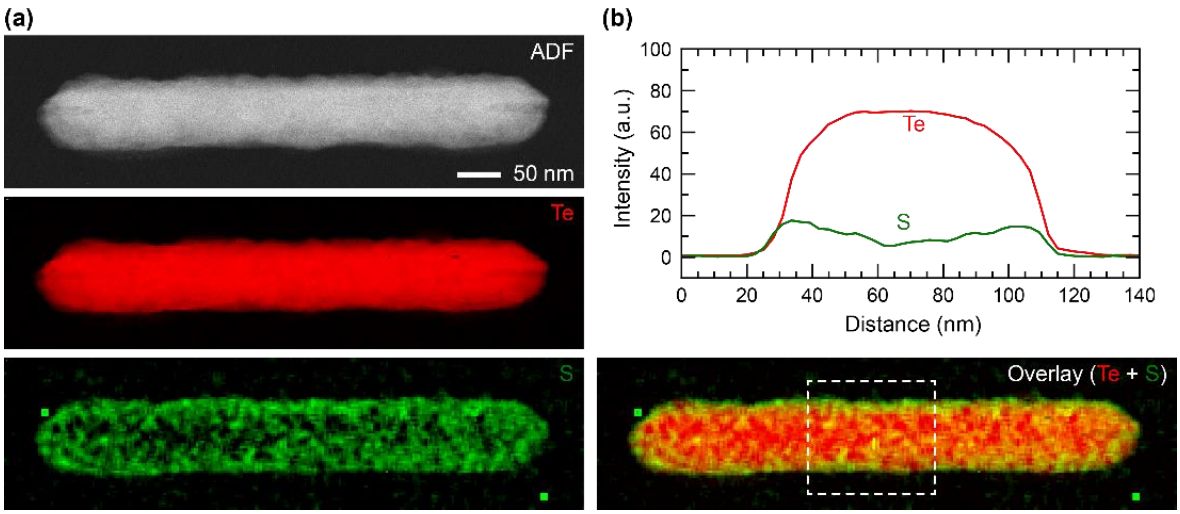

Figure 4.8. STEM-EELS elemental mapping of S^{2-}Te-NWs: (a) Annular dark-field (ADF) STEM image of a selected NW and corresponding (Te, S) elemental EELS maps. (b) Overlay map of Te and S (bottom) and averaged and normalized line-profile across the NWs marked with the white dotted rectangle in the overlay map.

The higher spatial resolution of STEM-EELS allows us to create a more detailed map of sulfur distribution (Figure 4.8 a). The average line profiles from the overlay map clearly show that sulfur is concentrated on the surface, while tellurium is mainly located in the core region (Figure 4.8 b).

4.3.2 Thermoelectric Transport Properties of TeNWs and S^{2-}TeNWs Films

The thermoelectric properties of TeNWs and S^{2-}TeNWs films were evaluated using a cryostat probe station at temperatures ranging from 300K to 400K. The experimental method is described in section 2.4.2. To ensure consistency and to measure thermoelectric properties at higher temperatures (300K to 600K), we used a Seebeck coefficient/electrical resistance measurement system, ZEM3. For this purpose, we prepared drop-casted thin films on quartz substrates (13×4) mm^2 by depositing a solution of TeNWs and S^{2-}TeNWs (suspended in a 3:2 mixture of IPA and ethanol), followed by annealing at 300°C in a nitrogen-rich environment for one hour. Figure 4.9 illustrates the temperature-dependent thermoelectric properties of both the TeNWs and S^{2-}TeNWs films.

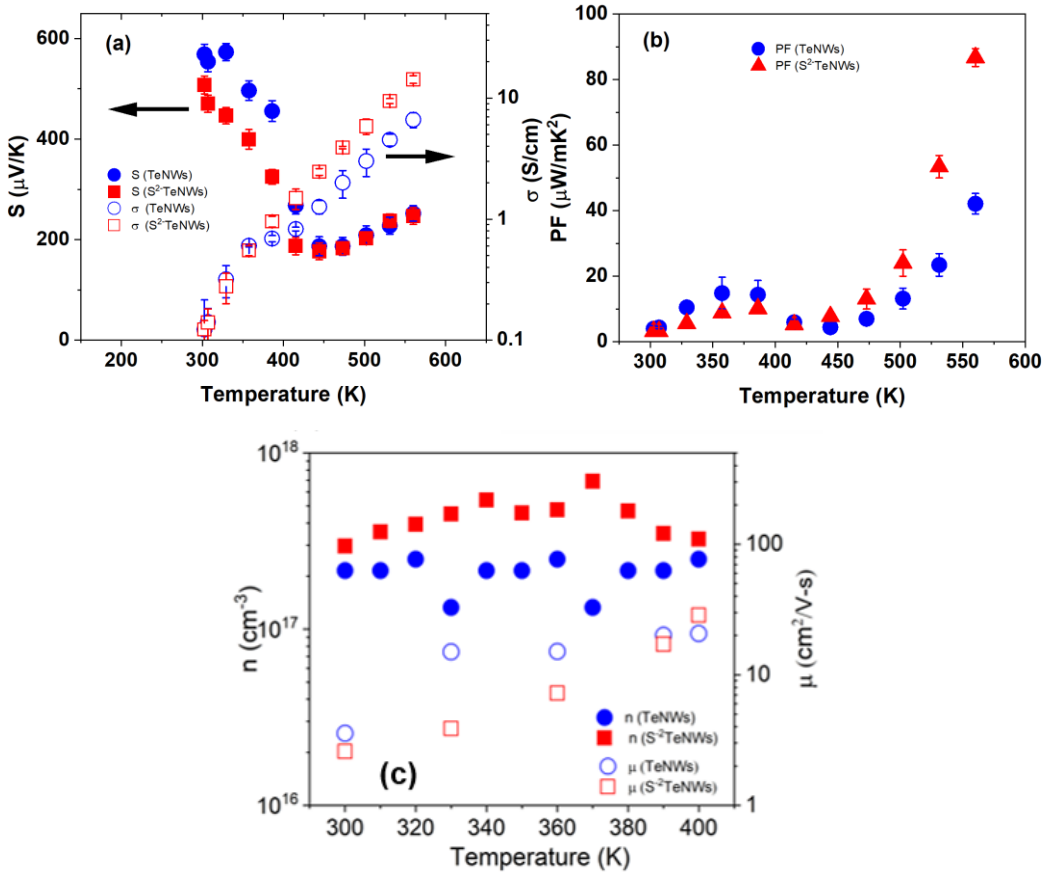

Figure 4.9. Transport properties of nanowires films: (a) Temperature dependent Seebeck coefficient, electrical conductivity and (b) power factor of TeNWs and S^{2-}TeNWs films. (c) Carrier concentration and mobility as a function of temperature.

The positive Seebeck coefficient values observed in these films confirm their p-type semiconductor characteristics. As the temperature increases, the Seebeck coefficient decreases up to 450K, after which it begins to increase for both TeNWs and S^{2-}TeNWs films. Above 460K, the Seebeck values of both films become similar. A similar Seebeck coefficient trend has been reported for Te bulk material by Hua Peng et al.[89] and T. Fukuroi et al.[184] Meanwhile, the electrical conductivity of TeNWs shows a steady increase, from 0.12 S/cm at 300K to 7 S/cm at 560K. This leads to a peak power factor of 42 ± 3 $\mu W/mK^2$ at 560K. We observed an improvement in thermoelectric performance when sulfur was added to the TeNWs matrix. The thermoelectric properties shown in Figure 4.9 (a & b) indicate that the S^{2-}TeNWs film follows a similar trend to the TeNWs film but with higher power factors. The Seebeck coefficient of the S^{2-}TeNWs behaves similarly to that of the TeNWs. However, as the temperature increased from 300 to 560 K, the electrical conductivity of S^{2-}TeNWs gradually increased from 0.12 to 14 S/cm, resulting in a power factor increase to 87 ± 3 $\mu W/mK^2$. To understand this better, we performed Hall measurements to determine carrier concentration and mobility in both TeNWs and S^{2-}TeNWs films. The results are plotted in Figure 4.9 (c). The S^{2-}TeNWs films have slightly higher carrier concentrations throughout the temperature range (300-400 K) compared to TeNWs films, which leads to a slightly lower Seebeck coefficient, as seen in Figure 4.9 (a). At room temperature, the carrier concentration was about ~ 3-5 $x10^{17} cm^{-3}$ for S^{2-}TeNWs films and ~ 2 $x10^{17}$ cm^{-3} for TeNWs films. Similar carrier concentrations have been reported by Fukuroi et al. for pristine Te bulk material at room temperature.[184] On the other hand, mobility increases with temperature in both systems. While the TeNWs show slightly higher mobility at 300 K, a crossover occurs at 400 K. This increase in mobility further enhances the electrical conductivity in both TeNWs and S^{2-}TeNWs films, as demonstrated in Figure 4.9 (a). We conducted a comparison with the existing literature, as summarized in Table 5.

Table 5. Summary of Transport Properties of Thin Films based on Te Nanowires, including Te bulk.

Material	σ(S/cm)	S(μV/K)	PF (μW/m-K^2)	T	κ(W/m-K)	ZT
Te-bulk [90]	59	300	531	300K	1.69	0.10
TeNWs [93]	0.26	568	8.44	300K	-	-
TeNWs [81]	0.013	551	0.39	300K	0.16	7.2×10^{-4}
TeNWs [104]	0.1	400	1.6	300K	-	-
TeNWs [105]	0.08	408	2.7	300K	2- (bulk value)	4.4×10^{-4}
TeNWs [113]	0.015	758	0.9	300K	-	-
TeNWs (our work)	7 ± 1	252 ± 15	42 ± 1	560K	-	-
S^{2-}TeNWs (our work)	14 ± 1	246 ± 16	87 ± 3	560K	-	-

We compared our power factor values of thin films with those reported in previous studies, and as shown in Table 5, our work achieved the highest power factor. Specifically, our highest power factor of 87 μW/mK² is about 10 times greater than the 8 μW/mK² reported in the literature and nearly twice as high as the 42 μW/mK² measured for the TeNWs we synthesized in this study without sulfur capping.

4.3.3 Fabrication of S^{2-}TeNWs-P3HT Composite Hybrid Materials

Although the incorporation of conducting polymers with inorganic nanostructured materials is a novel versatile pathway to design and develop the high performing next generation of TE materials yet there is a lack of high performing materials, which limits the applications of organic-inorganic hybrid TE materials on large scale. The main reason behind this is the chemical incompatibility between two dissimilar materials which is responsible for the electronic and morphology mismatch and leads to worse transport properties of TE hybrid materials. To construct hybrid TE materials; electronic and energetic matching, and chemical compatibility between inorganic and organic elements needs to occur.[166,185,186,187,188] The conventional physical mixing of organic and inorganic materials leads to uncontrolled phase separation, which further results in irreproducible and poor properties of hybrid materials. Besides, if the soft organic and hard inorganic components are not strongly combined together, they segregate from one another because of weak interactions and produce an unstable composite material, this would sternly limit their use in any thermoelectric applications.[166,189]

Based on our experimental and literature understanding detailed in section 4.1, we conceived that surface of nanowires modified with sulfur linker may facilitate the linkage of nanostructures to a polymer of choice and may produce an extremely stable nanocomposite hybrid TE material. Therefore, for the first time, we utilised S^{2-}TeNWs to embed them into P3HT matrix via mechanical mixing and a suspension was drop-casted onto Si and quartz substrates to fabricate composite hybrid thin films. The complete process is explained in section 2.1.4. Next, we attempted to engineer the interface between S^{2-}TeNWs and P3HT polymer via doping through a suitable dopant ($FeCl_3$), to observe an optimum potential barrier height of nanocomposite hybrid TE materials. The hybrid films of S^{2-}TeNWs-P3HT composites were subsequently used for material characterization and their thermoelectric transport properties were evaluated, as described in the following section.

4.3.4 Characterisation of Composite Hybrid Films

To examine the morphology of the films, SEM imaging was conducted on the composite hybrid films. Figure 4.10 shows representative SEM images of S^{2-}TeNWs-P3HT composite films with different concentrations of S^{2-}TeNWs within the P3HT matrix. The images reveal a uniform distribution of the nanowires throughout the P3HT matrix.

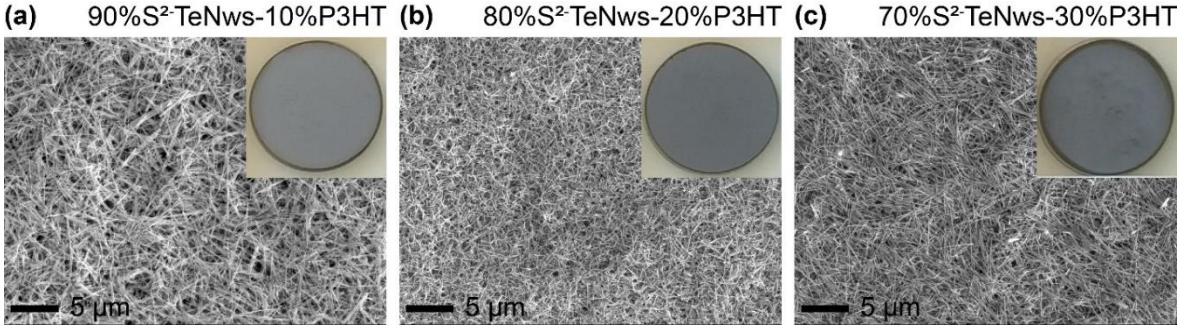

Figure 4.10. Microstructural characterization of S^{2-}TeNWs-P3HT composites. SEM micrographs of composite hybrid films with different concentration of S^{2-}TeNWs in P3HT matrix (a) 90 wt%, (b) 80 wt%, and (c) 70 wt%. Insets of SEM images include the optical image of uniform, and homogenous S^{2-}TeNWs-P3HT hybrid films, corresponding to each concentration.

To observe the encapsulation of the nanowires within the polymer, TEM imaging was performed. Sample preparation for TEM is detailed in Section 2.3.4. High-magnification TEM images of individual S^{2-}TeNWs-P3HT composite nanowires reveal a uniform, conformal coating of the polymer on each nanowire as shown in Figure 4.11 (d & e). The presence of an approximately 3 - 4 nm amorphous layer on the highly crystalline nanostructures indicates that the S^{2-}TeNWs are well embedded within the P3HT matrix.

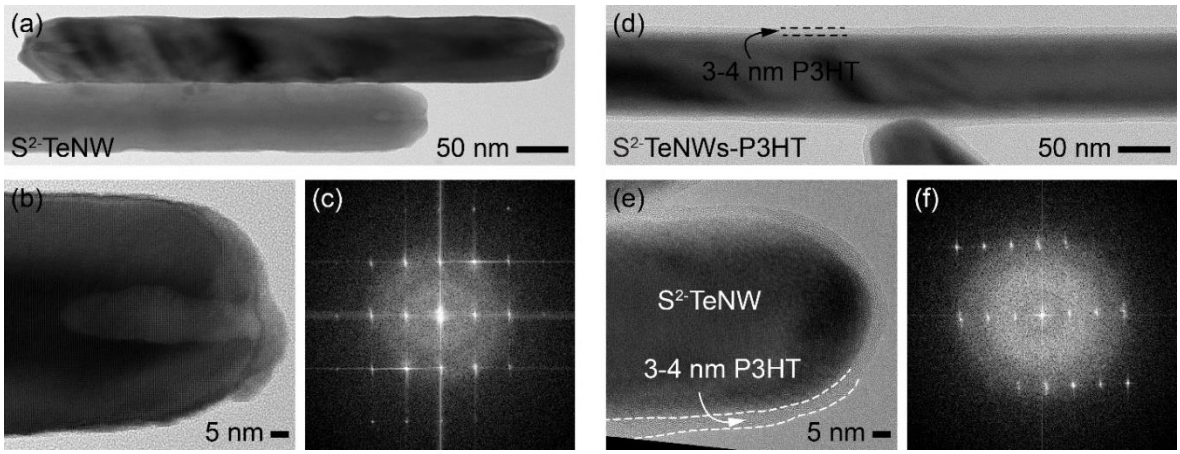

Figure 4.11. Microstructural characterization of composites by TEM. TEM images of (a, b) S^{2-}TeNWs and (d, e) S^{2-}TeNWs-P3HT hybrid composites, exhibiting the individual nanowires morphology and uniformly coated surface of nanowires with an amorphous layer of P3HT. (c & f) FFT of S^{2-}TeNWs and S^{2-}TeNWs-P3HT.

4.3.5 Thermoelectric Transport Properties of S^{2-}TeNWs-P3HT Composite Hybrid Films

The fabricated uniform hybrid films were doped in 0.03M $FeCl_3$-acetonitrile solution prior to measuring the TE transport properties. The doping process is described in section 2.2.2. The electrical conductivity and the Seebeck coefficient of S^{2-}TeNWs-P3HT composite hybrid films were determined through the standard procedures explained in experimental section 2.4.1. TE transport parameters as a function of weight percent concentration of nanowires are shown in Figure 4.12. All measurements were obtained at room temperature.

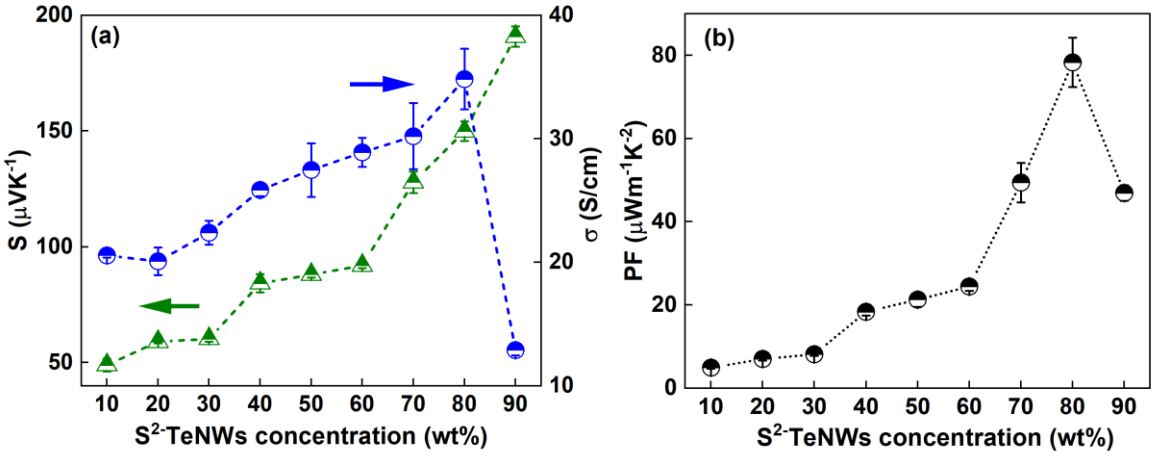

Figure 4.12. TE transport properties of S^{2-}TeNWs-P3HT hybrid films: (a) Seebeck coefficient and electrical conductivity, (b) power factor as a function of weight ratio of S^{2-}TeNWs from 10 wt% to 90 wt% blended with P3HT matrix, samples were doped with 0.03M $FeCl_3$.

Figure 4.12 (a) indicates that the Seebeck coefficient (S) increases with increasing content of S^{2-} TeNWs in hybrid composites. The Seebeck coefficient increases gradually from 49 to 191 μVK^{-1} by changing 10 wt% to 90 wt% content of S^{2-}TeNWs in composite hybrid films. The effects of S^{2-}TeNWs contents on electrical conductivity (σ) of composites are also presented in Figure 4.12(a). Electrical conductivity rises from 21 S/cm to a peak of 35 Scm^{-1} as the S^{2-}TeNWs content increases form 10 wt% to 80 wt%. Beyond the 80 wt% it drops down quickly to 12 Scm^{-1} at 90 wt% content of S^{2-} TeNWs.

As a result, the optimum performance is achieved at 80 wt% S^{2-}TeNWs, where the hybrid composite film exhibits a power factor of 78 $\mu W\text{-}m^{-1}K^{-2}$, electrical conductivity (σ) of 35 S/cm, and a Seebeck coefficient (S) of 150 µV/K at room temperature. This highlights the unique advantage of hybrid materials, as their thermoelectric performance surpasses that of their individual inorganic and organic components.

4.3.6 Interfacial Barrier Heights of S^{2-}TeNWs-P3HT Composites

To observe the rational engineering of interface potential barriers between organic and inorganic components, we fabricated thin films of S^{2-}TeNWs-P3HT composite with 80 wt% S^{2-}TeNWs on quartz substrates and these films were immersed in different molar concentration of $FeCl_3$-acetonitrile solution to estimate the highest occupied molecular orbital (HOMO) onsets in hybrid films through photoelectron emission spectroscopy in air (PESA) under normal conditions of pressure and temperature. The valance band onset and work function of pure S^{2-}TeNWs was estimated by ultraviolet photoemission spectroscopy (UPS). Representative graphs are shown in Figure 4.13.

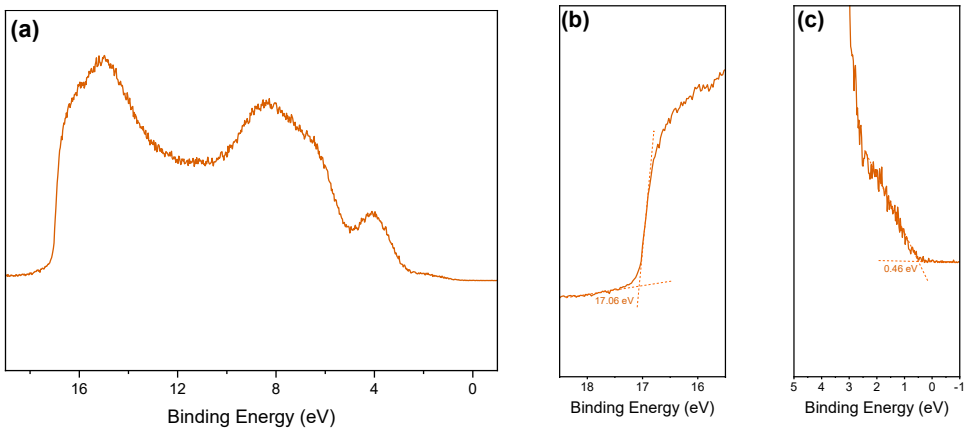

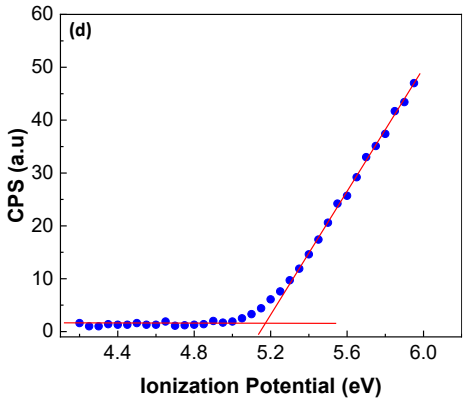

Figure 4.13. UPS and PESA spectra for energetics estimation. (a) UPS full spectra of pure S^{2-}TeNWs, (b) the secondary electron cut-off region, (c) Ionization potential of valance band onset. (d) PESA representative plot to estimate the ionization potential of 0.01M $FeCl_3$ doped S^{2-}TeNWs-P3HT hybrid film.

UPS was conducted to determine the energy levels and work function of drop casted S^{2-}TeNWs films as shown in Figure 4.13 (a-c). The ionization potential (IP) and work function (Φ) were obtained by using the relation: $(\Phi) = h\nu - E_{SECO}$ and $IP = E_{onset} + \Phi$, where $h\nu$ is 21.22 eV, E_{SECO} is secondary electron cut-off energy and E_{onset} is the spectral onset in the valance range. The values of E_{SECO} =17.06 eV, E_{onset} = 0.46 eV, Φ = 4.16 eV, and IP = 4.62 eV for S^{2-}TeNWs film were determined. Liang et al.[113] have also determined the ionization energy (IP) of pure tellurium nanowires (TeNWs) to be 4.52 eV. The discrepancy in our measured value (4.62 eV) compared to those reported in the literature may be attributed to the surface modification of TeNWs with a sulfur linker. As displayed in Figure 4.13 (d), the energy levels of hybrid materials were estimated through PESA, where the data points along the horizontal axis formed a background line while the sloped data points formed the regression line. The intercept of regression line and background line provides the HOMO onset or ionization potential of hybrid materials. The interface barrier heights were calculated by finding the difference between HOMO of composites at various doping levels and E_{VB} of pure S^{2-}TeNWs film and summarized in Table 6.

Table 6. Summary of Energy levels of Hybrid Materials, including S^{2-}TeNWs. Where the IP, E_{VB}, HOMO, $E_{barrier}$ are the ionization potential, valance band energy, the highest occupied molecular orbital, and energetic potential barrier heights respectively.

Sample	*Dopant Molar Conc. [M]*	*IP/E_{VB}/HOMO [eV]*	*$E_{barrier}$ [eV]*
S^{2-}TeNWs-P3HT	0.01 M	5.17 ± 0.09	0.55 ± 0.088
S^{2-}TeNWs-P3HT	0.02 M	5.32 ± 0.01	0.70 ± 0.013
S^{2-}TeNWs-P3HT	0.03 M	5.34 ± 0.004	0.72 ± 0.003
S^{2-}TeNWs-P3HT	0.04 M	5.39 ± 0.02	0.77 ± 0.021
S^{2-}TeNWs-P3HT	0.05 M	5.40 ± 0.03	0.78 ± 0.026
S^{2-}TeNWs-P3HT	0.06 M	5.41 ± 0.03	0.79 ± 0.031
S^{2-}TeNWs-P3HT	0.07 M	5.40 ± 0.03	0.78 ± 0.026
S^{2-}TeNWs	-	4.62 ± 0.003	-

A band diagram based on interface potential barriers is shown in Figure 4.14(a), a representative plot of 0.03M $FeCl_3$ doped composite hybrid sample is displayed in Figure 4.14 (b).

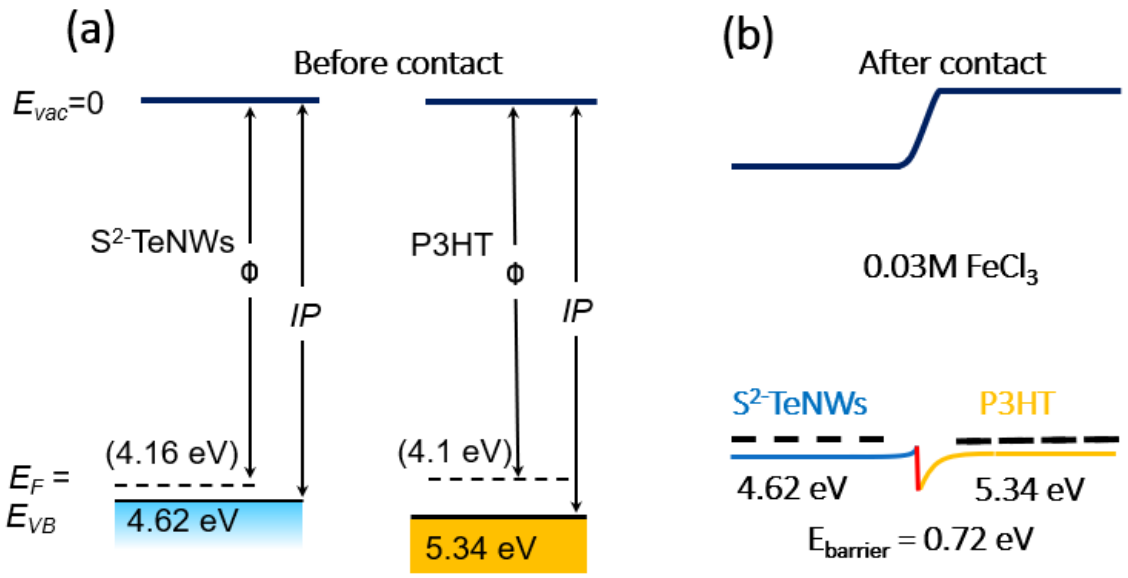

Figure 4.14. The band diagram of S^{2-}TeNWs-P3HT hybrid composites (80% S^{2-}TeNWs-20% P3HT). (a) before contact and (b) after contact. E_{vac}, E_F, E_{VB}, and $E_{barrier}$ are the vacuum level, Fermi level, valance band energy/Ionization potential and interfacial potential barrier, respectively.

Table 6 and Figure 4.14 reveal that a barrier height of 0.72 eV is attained at 0.03M of $FeCl_3$ dopant for the $S^{2-}TeNWs_{80}$-$P3HT_{20}$ composite hybrid material. We compared our results with existing studies and found that Liang et al.[113] have experimentally tuned the energy barrier between the

HOMO of P3HT and the valance band (VB) of TeNWs. They reported an energy barrier height of 0.88 eV for the composite film doped with 0.03M $FeCl_3$.

4.3.7 Doping Efficiency of S^{2-}TeNWs-P3HT Hybrid Films

To investigate the doping level of S^{2-}TeNWs- P3HT composites, we chose the 80 wt% S^{2-}TeNWs composite hybrid sample that has resulted in the highest performance at room temperature. TE transport properties as a function of doping levels were performed on seven hybrid films which were doped with different molar concentration of $FeCl_3$ (0.01M-0.07M) as shown in Figure 4.15.

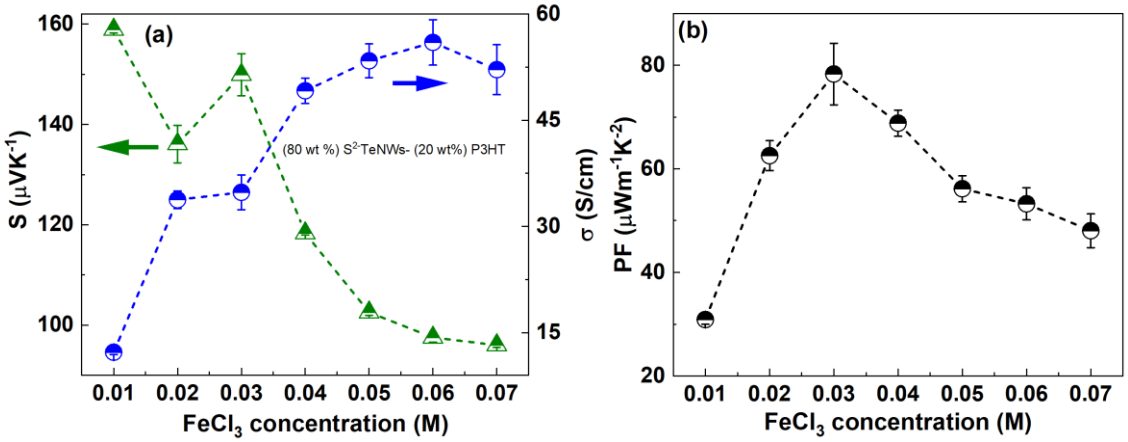

Figure 4.15. Doping efficiency of S^{2-}TeNWs-P3HT hybrid composite films. (a) Seebeck coefficient and electrical conductivity, (b) power factor as a function of molar concentration of $FeCl_3$.

Figure 4.15 (a) shows the decreasing values of Seebeck coefficient from 159 μVK^{-1} to 96 μVK^{-1} with increasing molar concentration of $FeCl_3$. The electrical conductivity exhibits a reverse trend compared to Seebeck coefficient, as expected. By increasing the molar concentration of the dopant, the electrical conductivity has risen from 12 Scm^{-1} to 67 Scm^{-1}. The highest power factor of 78 $\mu W m^{-1}K^{-2}$ for 0.03M $FeCl_3$ doping level is consistent with the results in Figure 4.12 (b). This implies that 0.03M $FeCl_3$ doping is an optimum level to effectively enhance the performance of S^{2-}TeNWs-P3HT composite hybrid films. The possible explanation is that the number of charge carriers generated along the polymer chain increase with increasing molar concentration of dopant in composite materials, which further leads to enhance the electrical conductivity and reduces the Seebeck coefficient.[115,175]

To compare our results with the literature, so far we have found a single report of Liang Z.,[113] who designed the TeNWs-P3HT composite hybrid materials system and doped them with 5% and 30% $FeCl_3$ (wt%). The heavily doped (30% $FeCl_3$) TeNWs-P3HT composites with 50% (by weight) TeNWs content, exhibited conductivity values of 2 Scm^{-1}, Seebeck coefficient of 222 μVK^{-1}, and a power factor of ~ 10 $\mu Wm^{-1}K^{-2}$ at room temperature. The second reported value is from our previously

published work on TeNWs-P3HT hybrid system where we reported the power factor values of 65 $\mu Wm^{-1}K^{-2}$ at 300K.[156] In comparison to both reports, here we first resolved the issue of chemical incompatibility between organic and inorganic components through surface modification with sulfur linkers to provide the best dispersion in polar solvents and facilitate the linkage with polymers to fabricate a robust high performing composite hybrid TE material. We controlled over the oxidation during the fabrication of composite hybrid materials by performing all processes in a nitrogen filled glovebox with O_2 < 1ppm, and H_2O < 1ppm. In summary, our experimental data indicates the sample with 80% (by weight) content of S^{2-}TeNWs doped at 0.03M $FeCl_3$ exhibits the highest power factor of 78 $\mu Wm^{-1}K^{-2}$ is amongst the highest reported values for S^{2-}TeNWs-P3HT composite hybrid materials.

4.4 Conclusions

In summary, our study demonstrates a significant enhancement in the thermoelectric (TE) properties of Tellurium nanowires (TeNWs) by modifying the surface of the TeNWs using sulfur moieties. Bare-TeNWs exhibited electrical conductivity (σ) of 7 ± 1 S/cm, Seebeck coefficient (S) of 252 ± 15, and a power factor (PF) of 42 ± 3 $\mu W/mK^2$ at 560K. After modifying the surface of TeNWs, these values improved to σ of 14 ± 1 S/cm, S of 246 ± 16, and PF of 87 ± 3 $\mu W/mK^2$ at 560K, with enhanced charge carrier mobility observed as the temperature increased. This surface modification not only resulted in the improvement of the TE properties but also effectively reduced oxidation 15 at% to 10 at% within the TeNWs matrix.

We further combined the surface-modified TeNWs with a conductive polymer (P3HT) to create hybrid composite materials. Among these, a composite film with a composition of $S^{2-}Te_{80}$-$P3HT_{20}$ exhibited the optimum power factor (PF) of 78 ± 6 $\mu W/mK^2$, electrical conductivity (σ) of 35 ± 3 S/cm, and Seebeck coefficient (S) of 150 ± 4 μV/K, with 0.03M $FeCl_3$ doping at room temperature. The thermoelectric transport properties of composite hybrid system have strongly established that the performance of hybrid system is robustly higher than the individual constituent elements, which is true definition of a hybrid composite material.

In conclusion, sulfur passivation on the surface of Te nanowires replaced the insulating PVP ligands with sulfur ions or functionalized the exposed surface with these ions. This was confirmed through elemental analysis using Energy Dispersive Spectroscopy (EDS) and validated by sulfur adherence onto the TeNWs' surfaces in elemental mapping via Scanning Transmission Electron Microscopy-Electron Energy Loss Spectroscopy (STEM-EELS). The sulfur ions on the nanowire surface carried a surface charge, which stabilized the nanostructures in polar solvents such as water or hexane,

preventing aggregation through electrostatic repulsion, as evidenced by stable dispersion shown in Zeta potential measurements.

Additionally, sulfur-passivated Te nanowires (TeNWs) exhibited reduced surface oxidation, as confirmed by X-ray Photoelectron Spectroscopy (XPS) analysis, and demonstrated enhanced charge carrier mobility compared to bare-TeNWs. These enhancements improved the thermoelectric transport properties of TeNWs. Sulfur capping also increased the compatibility between the inorganic TeNWs and the organic P3HT polymer, resulting in highly stable hybrid thermoelectric nanocomposite materials, as shown in SEM and TEM images. Consequently, the fabricated hybrid composite films (S^{2-}TeNWs-P3HT) displayed superior thermoelectric properties compared to hybrid films made with bare-TeNWs and P3HT.

These results imply that surface modification of nanostructures is an effective way of improving the TE transport properties of composite hybrid materials. This methodology is not confined to tellurium nanowires and P3HT hybrid system only, but it could be applied to other nanostructured materials with various conducting polymers. Additionally, to engineer the interface between organic and inorganic components assist to build an optimum barrier for obtaining the highest plausible TE performance of a hybrid system.

Chapter 5 Thermoelectric Performance of Composite Materials on using Long Nanowires and High Molecular Weight Polymers

This chapter is based on the manuscript: Syed Zulfiqar Hussain Shah et al., *Energy Env. Sci.,* **2024**. [To be submitted]

5.1 Introduction

Organic-inorganic hybrid thermoelectric materials hold significant appeal due to their ability to merge the advantageous characteristics of organic materials, such as low thermal conductivity and solution processability, with the structural and electronic tunability offered by inorganic nanostructures.[190,40,191] The distinctive feature of hybrid materials is their significantly enhanced performance, originating from non-linear interactions occurring at the nanoscale interfacial layer formed between organic and inorganic components.[162,192,166,128] Thus, to achieve the best thermoelectric performance in organic/inorganic composites, it is essential to manage both the material composition and the interactions at the interfaces.

It has been hypothesized that manipulating the length or diameter of nanowires could potentially enhance the thermoelectric performance of organic-inorganic hybrid materials. S.K. Yee et al.,[104] conducted a study in which tellurium nanowires (TeNWs) of varying sizes (length/diameters) were grown and embedded into a conducting polymer, poly(3,4-ethylenedioxythiophene): polystyrene sulfonate) (PEDOT: PSS), forming an organic-inorganic hybrid system. During the synthesis of the composites, the length of the nanowires was controlled by varying the amount of PEDOT: PSS solution: 4 mL produced short wires (~ 300 ± 50 nm), 2 mL produced medium wires (~ 450 ± 100 nm), and 1 mL produced long wires (~ 900 ± 100 nm). The study explored how nanowire length (or diameter) influences electrical conductivity and the Seebeck coefficient. A linear trend was observed: as the length of the nanowires increased, the Seebeck coefficient rose from 81 to 185 µV/K, whilst the electrical conductivity dropped from 23 to 7 S/cm. This trend is attributed to the size of the nanowires and electron-phonon scattering, where longer nanowires result in a thinner conductive interface, leading to reduced conductivity and more scattering of charge carriers between the polymer and nanowires. As a result, longer nanowires had higher Seebeck coefficients but lower electrical conductivity. To enhance the electrical conductivity, the longer nanowires encapsulated in PEDOT: PSS were doped with 5 vol.% of dimethyl sulfoxide (DMSO). This hybrid composite achieved a maximum power factor of 100 µW/mK² at room temperature.

Sahu et al.,[166] later used a multistep synthesis method to create two sets of nanowires (NWs) with different aspect ratios (length/diameter): 20 and 1000. The diameter was kept constant at 25 nm. The NWs were combined with PEDOT: PSS to fabricate hybrid systems. The resulting thermoelectric power factors were 25 μW/m-K² for the lower aspect ratio and 145 μW/m-K² for the higher aspect ratio. Recently, M.P. Gordon and colleagues[193] synthesized TeNWs with different diameters whilst keeping their length constant, then encapsulated them with PEDOT:PSS to create composite materials. They measured the transport properties based on the nanowire diameters and observed that the power factor increased from 40 ± 6 to 127 ± 10 μW/m-K² as the average diameter decreased from 109 to 57 nm. It was found that electrical conductivity consistently increased with decreasing nanowire diameter, while the Seebeck coefficient remained relatively stable. This improvement is attributed to increased charge carrier mobility, which resulted from polymer templating more effectively on the surface of the smaller-diameter nanowires, reducing surface energy and allowing the polymer chains to align or self-assemble on the TeNWs surface. Despite these discoveries, there has been limited exploration of the effects of nanowire diameter and length on the enhancement of TE performance in hybrid thermoelectric materials.[193]

However, achieving high ZT values in the hybrid system is highly desirable, necessitating low thermal conductivity. Table 7 is a comparison of thermoelectric transport properties of different conducting polymers based on inorganic-organic hybrid composites.

Table 7. Summary of transport properties of polymer/inorganic composites at room temperature.

Nanocomposites	Ref.	σ(S/cm)	S (μVK^{-1})	PF(μWm^{-1}K^{-2})	κ(Wm^{-1}K^{-1})	ZT
PEDOT: PSS/Sb_2Te_3	[194]	341	92.6	275	0.44	0.2
PEDOT: PSS/Bi_2Te_3	[182]	123.72	24.5	7.45	0.047	0.048
PEDOT: PSS/Bi_2Te_3	[67]	1000	45	205	0.29	0.2
PEDOT: PSS/Cu_2Se	[195]	1047	50.8	270	0.25	0.3
PEDOT: PSS/Te-NR	[105]	19.3	163	51	0.22	0.1
PEDOT: PSS/Te-NW	[66]	11	180	35	0.16	0.07
PANI/ Bi_2Te_3	[161]	11.6	36	1.5	0.10	0.005
PANI/ Te-NR	[68]	102	102	105	0.21	0.15
P3HT/ Bi_2Te_3	[57]	10	117	13.6	0.54	0.007

Kumar et. al., predicted P3HT based hybrid will be superior compared to PEDOT: PSS due to a higher scattering rate, as P3HT based polymers show higher scattering rate.[128] However, there is a scarcity of reports on Poly(3-hexylthophene)-P3HT based inorganic nanocomposites and so far we have only found two reports in the literature. Ming He et al.,[57] embedded Bi_2Te_3 into P3HT to fabricate P3HT/ Bi_2Te_3 nanocomposite hybrid films. They reported a PF ~ 14 μW/mK^2 coupled with a thermal conductivity of 0.54 W/m-K and ZT values ~ 0.007 for P3HT/Bi_2Te_3 hybrid films. Later Liang et al.,[113] fabricated P3HT-TeNWs nanocomposite hybrid films, achieving an electrical conductivity of 21 S/cm and a Seebeck coefficient of 67 μV/K. The highest reported PF of ~ 10 μW/mK^2 was achieved by doping the hybrid films with a 30 wt% $FeCl_3$ dopant. Recently our work on Te-P3HT has shown PF ~ 65 ± 1 μW/mK^2 by controlling the oxidation of TeNWs.[156]

Studies indicate that extended nanowires may demonstrate reduced thermal conductivity, attributed to the larger surface-to-volume ratio of nanowires, resulting in enhanced phonon scattering.[81,196] On the other hand, high molecular weight conducting polymers (CPs) demonstrate improved thermoelectric performance by virtue of their more extended and organized structure, which facilitates the delocalization of charge carriers (electrons or holes) along the polymer chains. The elongated chains offer a greater number of continuous conjugated pathways for charge

transport, thereby enhancing electrical conductivity. Simultaneously, these longer chains serve as barriers to the propagation of thermal energy, resulting in a decrease in lattice thermal conductivity. This combined effect contributes to the efficient thermoelectric performance of CPs.[197,198,199]

Although many polymer/inorganic composites have shown promisingly high Seebeck coefficients, their electrical conductivity remains below the desired levels. The formation of an intimate interfacial contact between nanostructures and polymer proves to be a significant challenge due to weak interactions. As a result, carrier transport in organic-inorganic composites is significantly hindered.[200]

The literature review reveals ongoing controversy regarding the role of nanowires with varying dimensions in composite materials, which remains unclear. To address this, we scaled up the synthesis process to grow longer nanowires by increasing the reaction time during the synthesis, embedding them into a conducting polymer, and investigated the thermoelectric (TE) performance of the resulting hybrid composites. Additionally, we fabricated composite materials by encapsulating Te nanowires (TeNWs) into high molecular weight P3HT, a study that has not been previously reported. We further examined the charge transport mechanisms and TE performance of these high molecular weight P3HT-based hybrid composites.

In this study, we synthesized long tellurium nanowires (~13 ± 2 µm) via ASS method as detailed in Section 2.1.2 and integrated them into Poly(3-hexylthiophene) (P3HT) using two different molecular weights (50-70 kDa and 80-143 kDa) via mechanical mixing as explained in Section 2.1.4. Our findings reveal an enhanced templating effect of P3HT along the tellurium nanowires, which significantly improved interfacial charge transport in the polymer-inorganic hybrid composites. The resulting $P3HT_{20}$-$TeNW_{80}$ thermoelectric hybrid composites achieved a high power- factor of 303 ± 38 µW/mK², with a thermal conductivity of 0.25 ± 0.04 W/mK, leading to a zT value of 0.36 ± 0.06 at room temperature. This shows a 32-fold increase in power factor compared to previously reported Te-P3HT hybrids[113] and a twofold improvement over Te-PEDOT:PSS composites.[166,193] We also systematically investigated the effect of varying nanowire concentrations within the polymer matrix and explored the corresponding doping levels for each concentration. The thermoelectric performance of these polymer-inorganic hybrid composites is discussed in detail in the results and discussion section.

5.2 Materials and Characterisation

The synthesis of TeNWs, the fabrication of hybrid composites, and the doping processes are explained in Sections 2.1 and 2.2. Details on the measurement of transport properties are provided

in Section 2.4. The material characterization methods used for the composites, along with sample preparation, are discussed in Sections 2.3.

5.3 Results and Discussion

5.3.1 Characterisation of TeNWs and Composite Films

We fabricated hybrid composite films by combining Tellurium nanowires (TeNWs) with Poly(3-hexylthiophene) (P3HT) in different weight ratios, ranging from 10% to 90 wt% TeNWs. The TeNWs and P3HT were dispersed in chlorobenzene and then drop-casted onto quartz substrates. Figure 5.1 shows that the resulting composite solution formed a stable suspension (Figure 5.1 a), and the films produced were uniform and consistent in appearance, as confirmed by optical imaging (Figure 5.1 b).

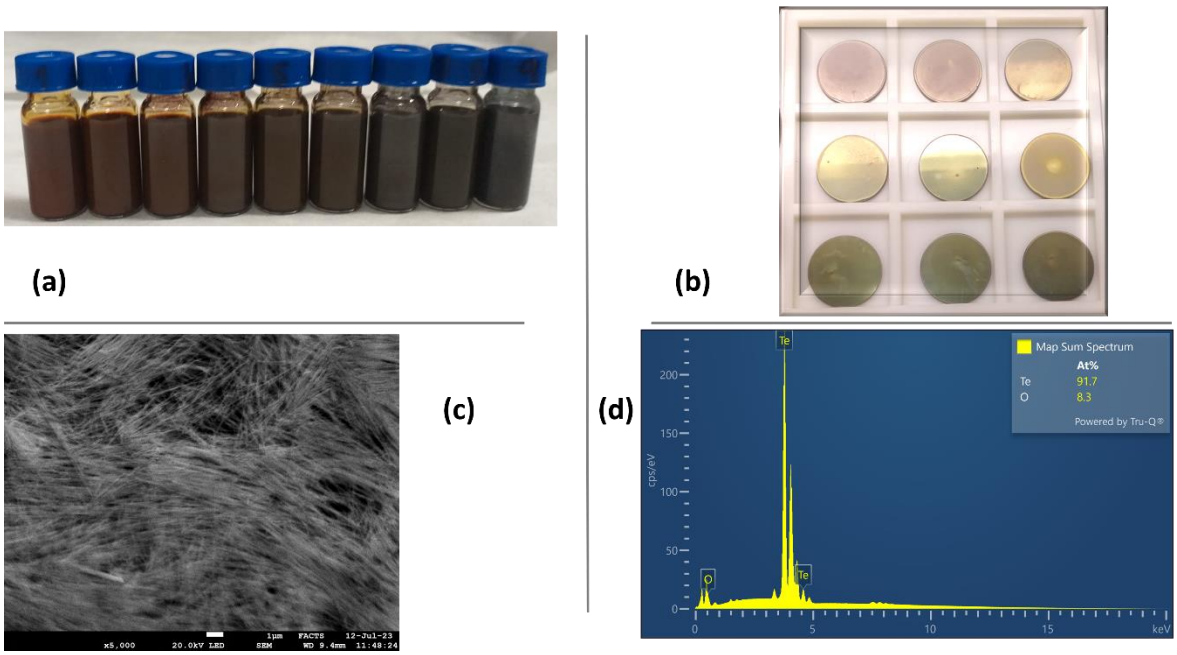

Figure 5.1. (a) Dispersion of TeNWs and P3HT in chlorobenzene (b) Fabricated hybrid thin films (c) SEM imaging of TeNWs (d) SEM-assisted EDX spectra of TeNWs.

To study the morphology and composition of the nanowires, we performed SEM imaging and EDX, as presented in Figure 5.1 (c & d). The SEM images reveal nanowires extending over several microns in length [8 to 13 µm]. Additionally, the EDX spectra, taken at a depth of 1-3 µm of the NW film, confirm the presence of Tellurium (92 at%) and demonstrated signs of oxidation (~ 8 at%) within the synthesized nanowires. We used X-ray photoelectron spectroscopy (XPS) to analyse the elemental composition and oxidation states in the fabricated thin films of TeNWs, as shown in Figure 5.2. The XPS survey spectra in Figure 5.2 (a), revealed the presence of tellurium, carbon, and oxygen. The spectra were calibrated using the carbon C 1s peak at 285 eV as a reference. Core-level

peaks corresponding to Te 3d, C 1s, and O 1s were observed in the TeNWs thin films. The O 1s peak near 530 eV indicated that the surface of the TeNWs was slightly oxidized (about 9 at%),[171] which aligns with the EDX results. In Figure 5.2 (b), peaks at 573 eV and 583 eV were identified as the Te $3d_{5/2}$ and Te $3d_{3/2}$ core levels, confirming the metallic state of tellurium.[201] Additionally, peaks at 576 eV and 586 eV indicated surface oxidation of the TeNWs within a depth of 5 nm from the film surface.[202]

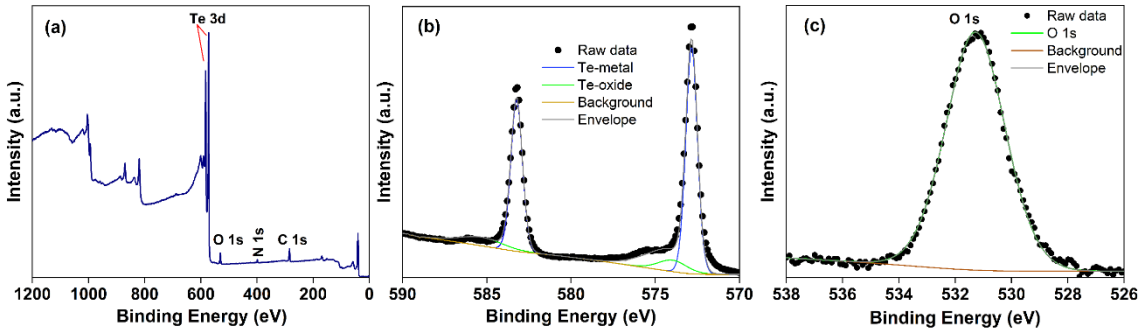

Figure 5.2. High-resolution X-ray photoelectron spectroscopy (XPS) spectra of TeNWs film: survey scan (a), XPS core level spectra of Te 3d (b) and core level spectra of O 1s (c).

5.3.2 Microstructural Analyses of TeNWs and Composite Films

To conduct detailed microstructural analyses of the extended nanowires (NWs) and hybrid composite materials, we utilized Transmission Electron Microscopy (TEM). The procedures for sample preparation and analysis are described in Section 2.3.4. As mentioned in the introduction, we fabricated hybrid composites by combining long TeNWs with two different molecular weights of P3HT. TEM analyses were performed on both types of composites including TeNWs as shown in Figure 5.3.

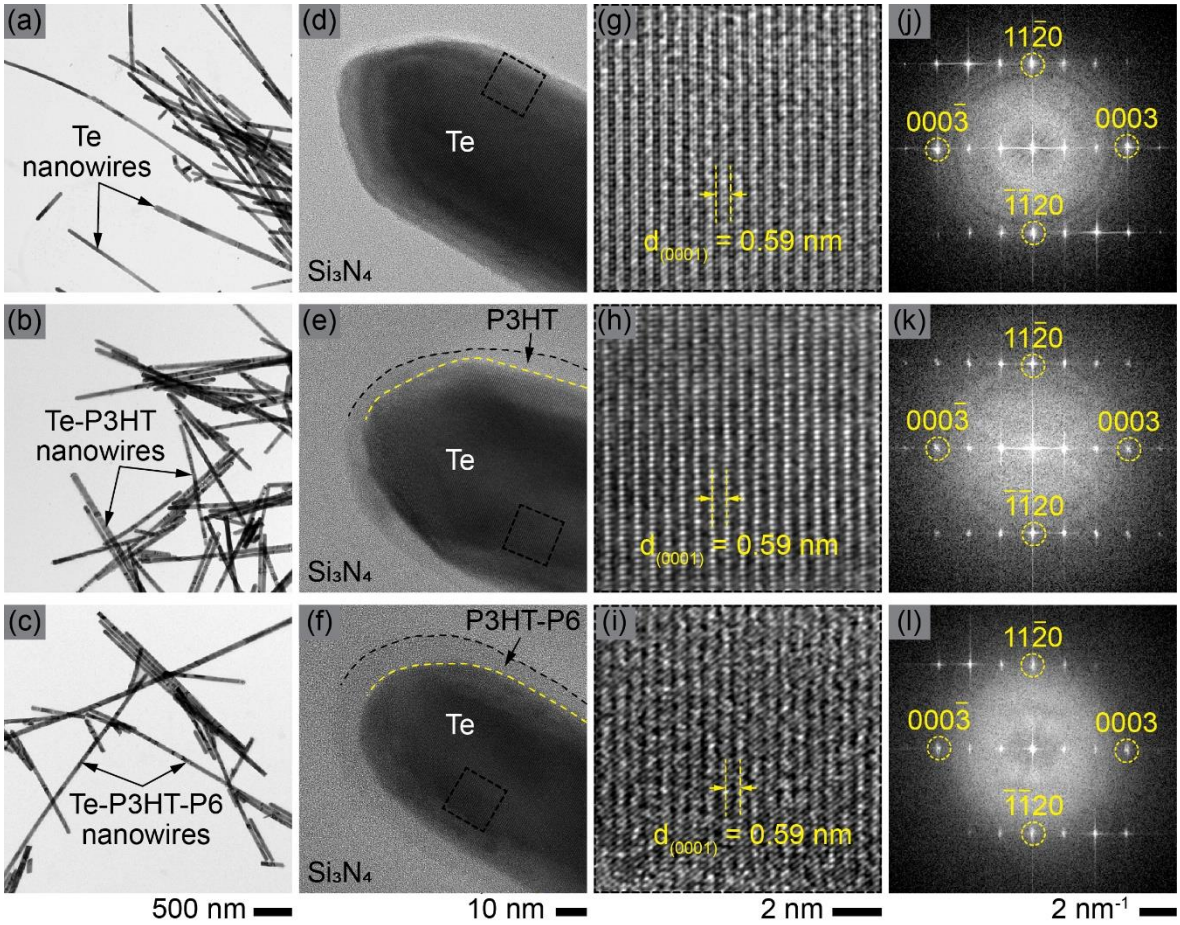

Figure 5.3. (a-c) Overview, (d-f) high-magnification, and (g-i) high-resolution TEM images showing the morphology of TeNWs, TeNWs-P3HT (50-70 kDa) and TeNWs-P3HT-P6 (80-143 kDa) nanowires, respectively. A uniform conformal coating of the amorphous polymer (P3HT) layer can be seen on the surface of the TeNWs-P3HT nanowires. (j-i) Fast Fourier Transform (FFT) of the single nanowires shown in (d-f), respectively.

Low-magnification TEM images of the TeNWs, TeNWs-P3HT (50-70 kDa), and TeNWs-P3HT-P6 (80-143 kDa) samples showed similar microstructures, with no noticeable differences in diameter (Figure 5.3 a-c). However, as anticipated, higher magnification TEM images of individual nanowires (Figure 5.3 d-f) revealed a uniform conformal coating of the polymer (P3HT) layer on the surface of the hybrid nanowires (Te-P3HT and Te-P3HT-P6). The thickness of this coating ranged from 3 to 10 nm, with an average of about 5 nm for both samples. High-resolution TEM (HR-TEM) images (Figure 5.3 g-i) and Fast Fourier Transform (FFT) analyses (Figure 5.3 j-l) confirmed that the nanowires are single-crystalline, with their c-axis ([001] crystallographic direction) aligned along the length of the nanowires, featuring an interplanar spacing of approximately 0.59 nm.

5.3.3 Characterisation of FIB Cross-Section Samples of TeNWs and Composites

Focused Ion Beam (FIB) cross-section samples of TeNWs and hybrid composites were prepared as described in Section **Error! Reference source not found.**. To protect the nanowire surface from b eam damage during FIB cutting, a 25 nm thick carbon layer was applied using a sputtering system. These cross-sectional samples were used to observe and correlate the distribution of chemical species detected in the XPS and SEM-assisted EDX results. To achieve this, we conducted Scanning Transmission Electron Microscopy (STEM) imaging and Electron Energy Loss Spectroscopy (EELS) mapping on these samples, using a probe size of approximately 1 nm as shown in the Figure 5.4.

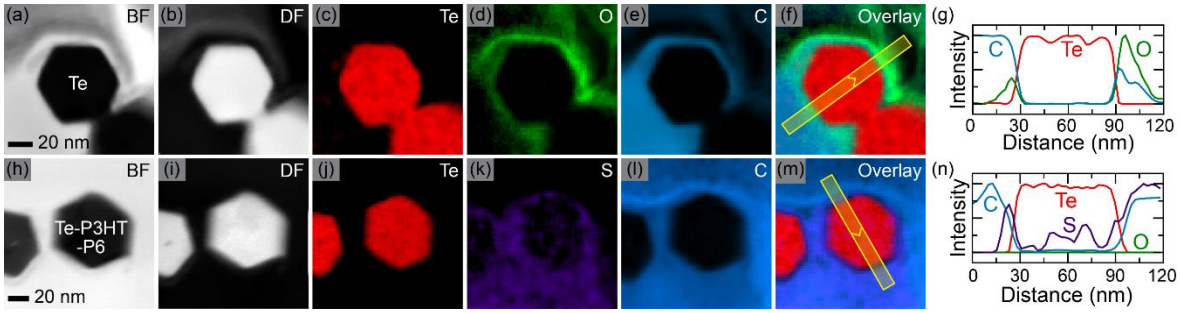

Figure 5.4. STEM on FIB cross-sectional samples of Te and hybrid composites: (a) Bright-field (BF) and (b) dark-field (DF) STEM images showing cross-section view of the Te-NWs. Elemental EELS maps of (c) Te (red), (d) O (green), (e) C (blue), and (f) overlay (Te + O + C) image for the Te-NWs. (g) Normalized line-profile across a single nanowire marked with the yellow strips in (f) showing chemical composition variation across the nanowire for the Te-NWs. (h-n) Corresponding data for the TeNWs-P3HT showing absence of O and presence of S (*purple*) around the edges of NWs.

The cross-sectional view of the TeNWs matrix in Figure 5.4 reveals that the nanowires have a hexagonal shape, with six (100) facets. TEM images from both the plane-view (Figure 5.3 a-c) and the cross-section (Figure 5.4 a-b and 5.4 h-i) show that the nanowires are several microns long and about 60 nm in diameter. Elemental mapping of nanowires using EELS in a cross-sectional view reveals that the core of the TeNWs is composed mainly of tellurium (shown in red), while oxygen (green) and carbon (blue) are located around the edges (Figures 5.4 c-e), also depicted in Figure 5.5 with extended area analysis. It is important to note that the carbon seen in the EELS map comes from the FIB process, not from the nanowire synthesis.

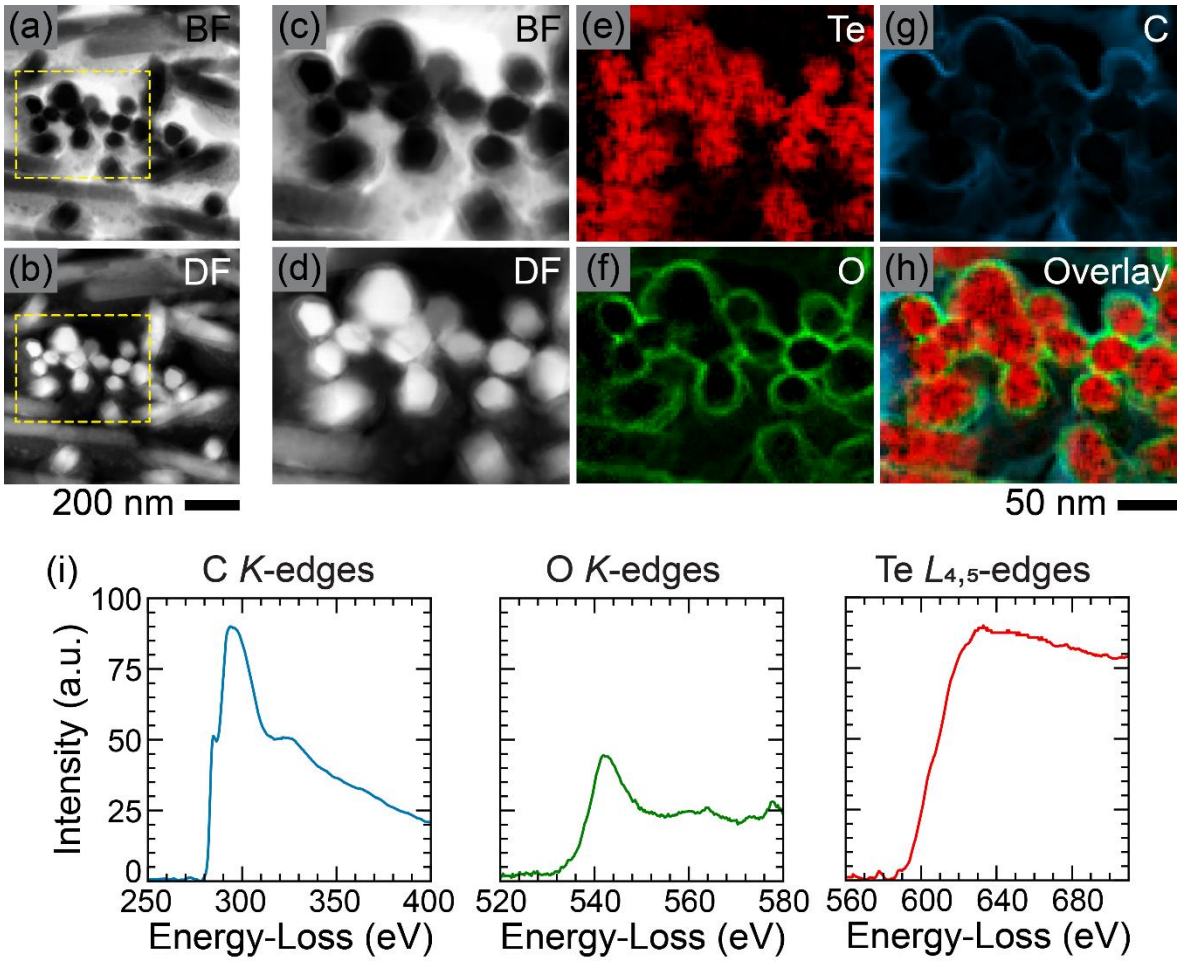

Figure 5.5. Cross-section STEM imaging and EELS mapping of TeNWs. Low-magnification STEM (a) bright-field (BF), (b) dark-field (DF) images of TeNWs. High-magnification STEM (a) BF, (b) DF images from the selected regions marked by yellow dotted box in (a and b). Elemental maps of (**e**) Te (*red*), (**f**) O (green), (**g**) C (*blue*), and (**h**) overlay (Te + O + C) image showing elemental distribution of different elements. (i) Average EELS C-*K*, O-*K* and Te-$L_{2,3}$ edges used to make the maps. All EELS were acquired using a probe size of about 1 nm and energy resolution of 1.25 eV.

A detailed examination of the overlay map (Figure 5.4 f) and the line-profile of a single nanowire (Figure 5.4 g) shows that the core of the nanowire is not oxidized. Both XPS and STEM-EELS results are consistent, indicating that non-coated tellurium nanowires do experience surface oxidation. In contrast, EELS mapping of hybrid (coated) nanowires shows the presence of sulfur around the nanowires (indicated by purple in Figure 5.4 k). Additionally, the line-profile of a single nanowire from the hybrid sample shows no oxygen signal (Figure 5.4 n).

5.3.4 Thermoelectric Transport Properties of TeNWs-P3HT Hybrid Composites

We fabricated hybrid composite films with different weight ratios (10 - 90 wt%) of TeNWs and P3HT for two molecular weights of P3HT (50-70 kDa and 80-143 kDa). For each combination (wt% ratio)

of TeNWs and P3HT, we prepared seven films to study doping levels using various concentrations of $FeCl_3$ (ranging from 0.01M to 0.07M). We then measured the thermoelectric properties of the TeNWs-P3HT hybrid films, of both systems. Figure 5.6 displays the thermoelectric properties of both hybrid systems as a function of TeNWs concentration at a fixed doping level (for TE measurements on other compositions, see Appendix B). The optimal doping levels were found to be 0.03M for the TeNWs-P3HT (50-70 kDa) and 0.02M for the TeNWs-P3HT-P6 (80-143 kDa) hybrids, yielding the highest thermoelectric performance.

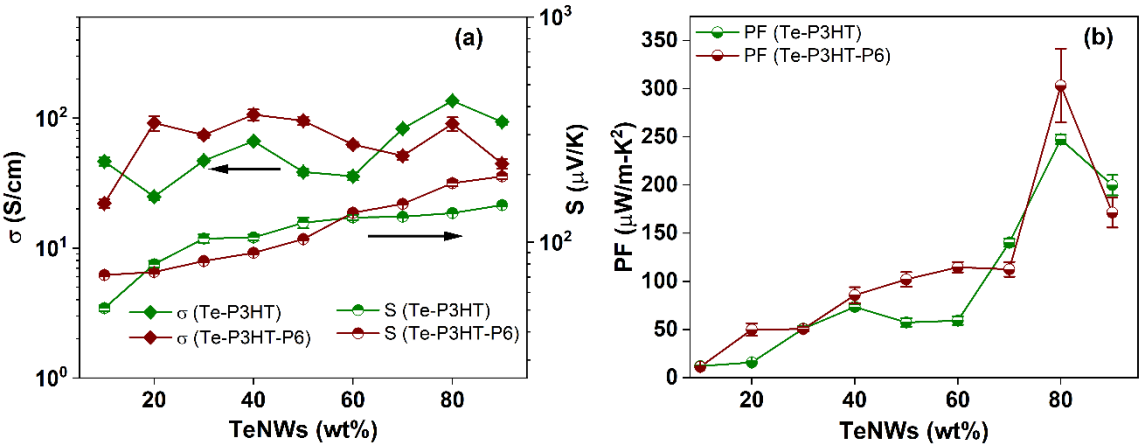

Figure 5.6. Exploring Thermoelectric Properties: TeNWs-P3HT hybrid systems reveal (a) conductivity and Seebeck coefficient, (b) power factor in hybrid (10-90 wt% TeNWs) with P3HT (M.W. 50-70 kDa), and with higher molecular weight P3HT-P6 (M.W. 80-143 kDa).

As shown in Figure 5.6 (a), the Seebeck coefficient consistently increased with higher TeNWs concentration, ranging from 51 to 146 μV/K as TeNWs concentration rose from 10% to 90% in the 0.03M doped samples. In contrast, electrical conductivity showed a non-linear response to increasing TeNWs content, rising from about 46 ± 3 S/cm at 10% TeNWs to 136 ± 3 S/cm at 80% TeNWs, then dropping to about 94 ± 5 S/cm at 90% TeNWs. Similar trends were observed in the TeNWs-P3HT-P6 (80-143 kDa) system (Figure 5.6 a), where electrical conductivity initially increased to ~ 106 ± 10 S/cm at 40% NWs, decreased to ~ 51 ± 4 S/cm at 70%, increased again to 91 ± 11 S/cm at 80%, and finally dropped to 45 ± 4 S/cm at 90% NWs. In both systems, the Seebeck coefficient consistently rose with increasing NWs content. Figure 5.6 (b) shows the power factors as a function of NWs content for the two hybrid systems, with improvements from 12 μW/mK² (10 wt% TeNWs) to 248 μW/mK² (80 wt% TeNWs) for the 0.03M $FeCl_3$ doped system, and from 11 μW/mK² (10 wt% TeNWs) to ~ 303 μW/mK² (80 wt% TeNWs) for the TeNWs-P3HT-P6 (80-143 kDa) system.

To measure thermal conductivities using the LINSEIS Thin Film Analyzer, we prepared TeNWs-P3HT-P6 (molecular weight: 80-143 kDa) hybrid films with 70%, 80%, and 90% TeNWs by weight, as these

compositions demonstrated higher power factors. Each sample underwent three heating cycles from room temperature to 100 °C, and three measurements were taken for each batch. Figure 5.7 (a) shows the average thermal conductivities of the doped samples as a function of TeNWs content. As the TeNWs content increased, thermal conductivity decreased. Specifically, the thermal conductivities for undoped 90%, 80%, and 70% TeNWs-P3HT-P6 hybrid composite films were 0.19 ± 0.04 W/m-K, 0.24 ± 0.02 W/m-K, and 0.33 ± 0.01 W/m-K, respectively. These values are relatively low, closely matching the intrinsic thermal conductivity of lattice structures in conducting polymer films, which typically range from 0.2 to 0.5 W/m-K.[203]

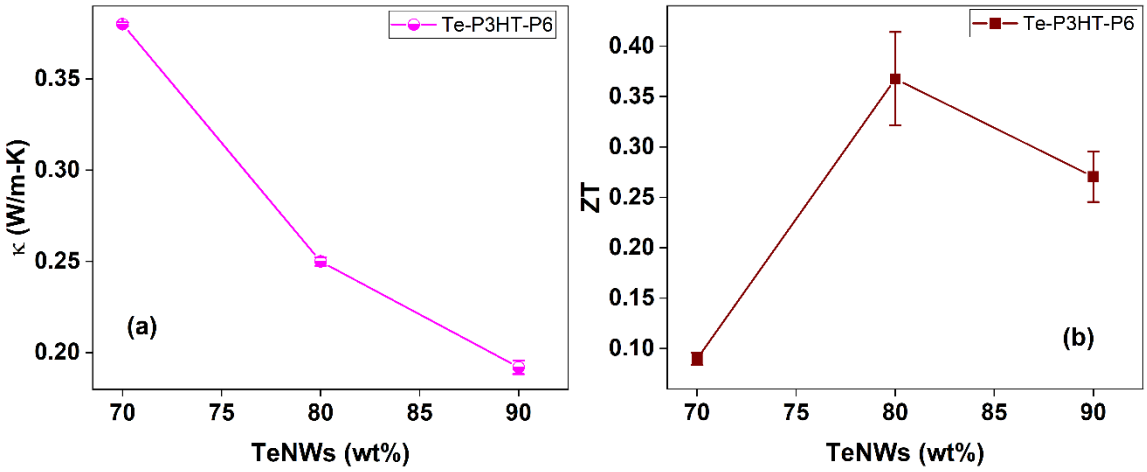

Figure 5.7. Thermal conductivity of Te-P3HT-P6 hybrid materials of 0.02M $FeCl_3$ doped hybrid samples (70% and 80 % Te), and undoped sample (90 wt%) Te-P3HT-P6 (a) and *zT* values as a function of TeNWs concentration (b). Error bars depict standard deviation from multiple measurements, ensuring result reliability.

The *zT* values for the hybrid composites were calculated using the thermal conductivity measured at room temperature. Figure 5.7 (b) shows the *zT* values plotted against the weight percentage of TeNWs. The highest zT value of 0.36 ± 0.06 was obtained for the sample with 80% TeNWs and 20% P3HT when doped with 0.02M $FeCl_3$. To the best of our knowledge, this represents the highest *zT* value reported for P3HT-based inorganic nanocomposite hybrid p-type materials, as highlighted in the literature comparison presented in Figure 5.8.

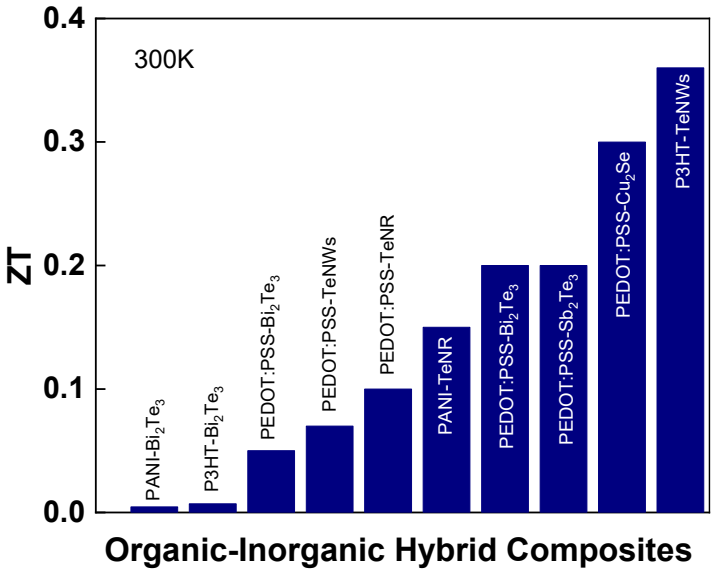

Figure 5.8. A comparison of *zT* values of different conducting polymers based organic-inorganic composites at room temperature, indicating the highest *zT* values of our fabricated P3HT-TeNWs hybrid composite films.

5.3.5 Interfacial Barrier Heights of TeNWs-P3HT-P6 Hybrid Composites

To investigate the interface potential barriers in the composites, we prepared thin films of TeNWs-P3HT-P6 composites with 70%, 80%, and 90% TeNWs (by weight) on quartz substrates. These films were immersed in $FeCl_3$-acetonitrile solutions with concentrations ranging from 0.01M to 0.03M. The work function (WF) and highest occupied molecular orbital (HOMO) of the hybrid composite films were measured using a Kelvin probe and photoelectron emission spectroscopy in air (PESA), respectively. The results are presented in Figure 5.9.

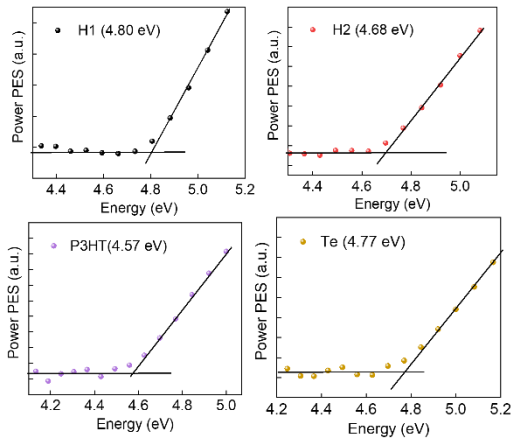

Type	HOMO[eV]
H1	4.80 ±0.01
H2	4.68±0.02
H3	4.68±0.08
P3HT	4.57±0.03
Tc	4.77±0.02

Type		WF[eV]
H1	w/o	4.26
	0.02M	4.43
H2	w/o	4.35
	0.01M	4.42
	0.02M	4.55
	0.03M	4.82
H3	w/o	4.42
	0.02M	4.66

Figure 5.9. Work function (WF) and HOMO measurements for TeNWs-P3HT hybrid composites (H1=90%, H2= 80%, and H3= 70% TeNWs by weight) obtained using Kelvin probe and PESA, respectively. The figure includes PESA plots and tables summarizing the

measured WF and HOMO values for both undoped (w/o) samples and samples doped with $FeCl_3$-acetonitrile solutions ranging from 0.01M to 0.03M.

Alberto et al.[116] demonstrated that the doping process significantly impacts the work function and electrical conductivity of hybrid materials. To investigate this effect, we can analyse the trend of the work function (WF) shown in Figure 5.9. The hybrid composite samples of Te_{80}-$P3HT_{20}$ were doped with $FeCl_3$ at molar concentrations ranging from 0.01M to 0.03M. The undoped (w/o) film had a WF value of 4.53 eV, which increased progressively with higher dopant concentrations, reaching 4.68 eV at 0.03M. P-type doping shifts the Fermi level closer to the HOMO of the composites. As a result, the WF increases because the Fermi level moves away from the vacuum level. At low dopant concentrations, the Fermi level shift is moderate, causing a small change in WF. However, as the dopant concentration rises, the Fermi level shifts more significantly, leading to a greater increase in the work function. Moreover, in our transport measurements of the hybrid samples Te_{80}-$P3HT_{20}$, we observed that the electrical conductivity increased from 16 ± 2 S/cm to 91 ± 11 S/cm as the dopant concentration was increased from 0.01M to 0.02M.

In hybrid composite materials, doping can significantly alter the interfacial barrier heights between the organic and inorganic components. The theoretical optimal energy barrier for maximum power factor enhancement is typically ≤0.2 eV.[106] These interface barrier heights are determined by the difference between the HOMO of the organic component and the E_{VB} of the inorganic component. As shown in Figure 5.9, the HOMO of P3HT is 4.57 eV, and the E_{VB} of TeNWs is 4.77 eV, resulting in an interfacial barrier height of 0.2 eV (close to the theoretical limit). When the hybrid film (H2 = Te_{80}-$P3HT_{20}$) was doped with 0.02M, the HOMO shifted to 4.68 eV, creating a reduced interfacial barrier height of 0.09 eV (≤0.2 eV). This change corresponded with the highest observed power factor of 303 ± 38 μW/m-K².

5.3.6 Kang-Snyder Charge Transport Model for Te-P3HT Hybrid Composites

We investigated the charge transport within the P3HT-TeNWs hybrid systems using the Kang and Snyder charge transport model for conducting polymers, as explained in detail in Section 1.6.4. We initially conducted de-doping experiments on TeNWs-P3HT (50-70kDa) and TeNWs-P3HT-P6 (80-143kDa) hybrid films, which were doped with 0.03M and 0.02M $FeCl_3$, respectively. The Seebeck coefficient as a function of conductivity is presented in Figure 5.10 (a). De-doping was achieved through heat treatment at 70°C, which gradually removed dopants and reduced electrical conductivity. As expected, the Seebeck coefficient increased as conductivity decreased. Additionally, the power factors gradually declined with the reduction in electrical conductivity.

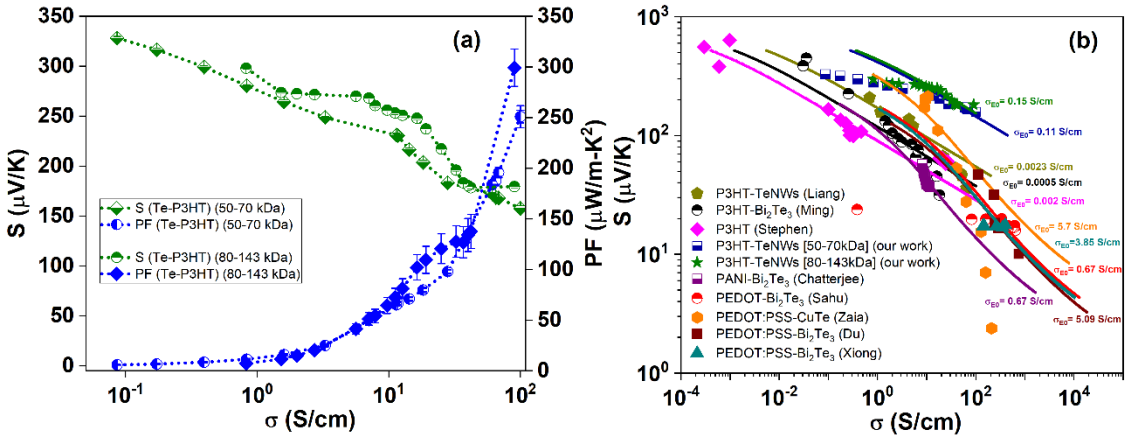

Figure 5.10. The application of the Kang-Snyder charge transport (CT) model to P3HT-inorganic hybrid systems. (a) The experimental data exhibiting relationship between Seebeck coefficient (S) and electrical conductivity (σ) for 0.02M and 0.03M $FeCl_3$-doped TeNWs-P3HT hybrid systems. (b) The data of electrical conductivity versus Seebeck coefficient for TeNWs-P3HT (olive stars) and TeNWs-P3HT (half-filled royal blue squares) from this study, along with TeNWs-P3HT (dark yellow pentagons), Bi_2Te_3-P3HT (half-filled black circles), pure P3HT (magenta square), PANI-Bi_2Te_3 (half-filled purple squares), PEDOT-Bi_2Te_3 (half-filled red circles), PEDOT:PSS-CuTe (orange hexagons), PEDOT:PSS-Bi_2Te_3 (wine squares), and PEDOT:PSS-Bi_2Te_3 (dark cyan triangles). Our experimental data aligns with the energy-dependent scattering parameter s = 3 curve, featuring energy-independent transport parameters σ_{E0} of 0.11 S/cm and 0.15 S/cm for TeNWs-P3HT (50-70kDa) and TeNWs-P3HT (80-143kDa) hybrid films, respectively.

To compare various binary organic-inorganic hybrid composite materials, we present Figure 5.10 (b), which shows the Seebeck coefficient as a function of electrical conductivity for several systems. These include TeNWs-P3HT (80-143kDa) [olive stars, this work], TeNWs-P3HT (50-70kDa) [half-filled royal blue squares, this work], TeNWs-P3HT [dark yellow pentagons, Liang Z.],[113] pure P3HT [magenta squares, Kang & Snyder],[127] Bi_2Te_3-P3HT [half-filled black circles, Ming H.],[57] PANI-Bi_2Te_3 [half-filled purple squares, Chatterjee],[161] PEDOT-Bi_2Te_3 [half-filled red circles, Sahu],[166] PEDOT:PSS-CuTe [orange hexagons, Zaia],[162] PEDOT:PSS-Bi_2Te_3 [wine squares, Du],[186] and PEDOT:PSS-Bi_2Te_3 [dark cyan triangles, Xiong].[196] Our data exhibited the highest σ_{E0} compared to those reported in the literature, therefore, indicating a superior power factor [see Table 7, Section 5.1].

The Kang-Snyder model was applied to analyse P3HT-based systems. As shown in Figure 5.10 (b), the experimental results for various P3HT-based hybrid materials consistently point to an energy-dependent scattering parameter of s = 3 [See Appendix A.6., an example for the fitting process of data with the Kang -Snyder model for different values of "s"]. In our TeNWs-P3HT (80-143kDa) hybrid system, σ_{E0} was determined to be 0.15 S/cm, representing a 65-fold increase compared to

the TeNWs-P3HT hybrid system reported in the literature[113] and about 10 times higher than our previous study on Te-P3HT hybrid materials.[156]

This significant enhancement in σ_{E0} is primarily due to the improved templating of P3HT on the Te surface, as discussed in detail in our earlier work on TeNWs-P3HT hybrid materials.[156] Longer nanowires with well-defined structures greatly improve both the templating effect and interfacial charge transport.[128,66] Additionally, using a high molecular weight polymer with longer chain lengths to encapsulate the nanowires enhances charge transport at the interfacial layer by providing a large, well-ordered polymer region (templating effect) along the nanowires.[198] The templating effect enhances mobility at the interface, while charge transfer at the interface induces de-doping, which increases the Seebeck coefficient of the interface layer. These factors collectively influence the conductivity and Seebeck coefficient trends in the hybrid composite materials.

5.4 Conclusions

In summary, in this study we adopted the strategies to enhance the thermoelectric (TE) performance of P3HT-TeNWs hybrid systems by increasing the length of the nanowires and using a high molecular weight polymer, both of which enhance the templating effect. This was achieved by scaling up the ASS reaction to synthesize longer tellurium nanowires. The resulting nanowires were ~ 13 ± 2 µm in length and 60 nm in diameter, as confirmed by SEM and TEM imaging.

These extended Te nanowires were then encapsulated in P3HT with two different molecular weights (50-70kDa and 80-143kDa) to create hybrid nanocomposites. TEM images of the individual nanowires showed a uniform conformal coating of the polymer (P3HT) layer, with an average thickness of about 5 nm for both samples. XPS and STEM-EELS analyses revealed no oxygen signal on a single nanowire from the hybrid sample, indicating successful encapsulation.

When measuring the thermoelectric properties of the hybrid samples (Te-P3HT 50-70kDa and Te-P3HT 80-143kDa), both systems showed optimal performance at a composition of 80 wt% Te and 20% P3HT, achieving the highest power factors of 248 ± 5 µW/mK² and 303 ± 38 µW/mK², respectively. The highest-performing hybrid composite, Te-P3HT (80-143kDa), exhibited a thermal conductivity (κ) of 0.25 W/m-K, leading to a *zT* value of 0.36 at room temperature—the highest reported for the P3HT-TeNWs hybrid system to date. The work function and HOMO of the high-performing hybrid sample (Te_{80}-$P3HT_{20}$) doped with 0.02M $FeCl_3$ were measured using Kelvin probe and PESA, showing a reduced interfacial barrier height of 0.09 eV, which is below the theoretical threshold (≤0.2 eV) needed to achieve the highest power factor in composite materials.

Using the Kang and Snyder Charge Transport Model on the TeNWs-P3HT (80-143kDa) hybrid system, σ_{E0} was found to be 0.15 S/cm, confirming the strong templating of P3HT on the Te nanowire surface. As a result, the hybrid composite materials demonstrated improved thermoelectric performance.

In conclusion, we have demonstrated that the thermoelectric performance of P3HT-TeNWs hybrid systems can be significantly enhanced by synthesizing longer tellurium nanowires and using high molecular weight P3HT, which enhance the templating effect. The optimized hybrid (Te-P3HT 80-143kDa) achieved a record-high power factor of 303 ± 38 μW/mK² and a zT value of 0.36, the best reported for this system. These findings highlight the potential of structural and interfacial engineering to advance thermoelectric materials.

Chapter 6 Conclusions and Prospectives

6.1 Summary of Results

This dissertation aimed to develop organic-inorganic hybrid thermoelectric composite materials and to explore various strategies for enhancing their thermoelectric properties. Through a series of experiments, we examined several approaches, such as controlling oxidation, improving doping efficiency, modifying the surface of nanowires, using long nanowires, and incorporating high molecular weight polymers to optimize the thermoelectric performance of these composite materials. The enhancements in thermoelectric properties achieved with each strategy are summarized in the following paragraphs.

Oxidation Control and Doping Efficiency: In Chapter 3, we developed ASS synthesis of Tellurium nanowires. After thorough cleaning, these nanowires were drop-casted onto silicon substrates and analysed using SEM, revealing lengths between 1 and 3 μm and diameters between 45 and 55 nm. We then fabricated two types of hybrid composite materials: one with oxidation-controlled tellurium nanowires (TeNWs) mixed with P3HT polymer, and the other with oxidized tellurium nanowires (TeO_2NWs) blend with P3HT. The nanowires, ranging in concentration from 10% to 90% by weight, were dispersed in chlorobenzene and drop-casted onto quartz substrates to measure the thermoelectric properties of the composite hybrid films. The films were doped with varying concentrations (0.01M to 0.07M) of $FeCl_3$. Our experimental results demonstrated that TeO_2NWs-P3HT exhibited electrical conductivity values of 12 S/cm, Seebeck coefficient of 114 μV/K and power factor values of 15 μW/m-K^2, whilst TeNWs-P3HT showed enhanced electrical conductivity of 39 S/cm, Seebeck coefficient of 128 μV/K, and power factor of 65 μW/m-K^2, at doping levels of 0.03M and 0.06M respectively. Both hybrid systems showed optimal performance at a composition of Te_{80}-$P3HT_{20}$ (wt%).

To better understand charge transport within these composite systems, we performed theoretical modelling and molecular dynamics (MD) simulations. The experimental data indicated an energy-dependent scattering parameter s = 3 for both hybrid materials. The energy independent parameter σ_{E0} was found to be 0.017 S/cm for TeNWs-P3HT and 0.0023 S/cm for TeO_2NW-P3HT. This higher σ_{E0} and the observed conductivity trends were explained by (MD) simulations, which revealed that P3HT aligns preferentially on a pristine Te surface rather than on a TeO_2 surface. This alignment or “templating” on the Te surface leads to the higher σ_{E0} value compared to the TeO_2 hybrid system. This templating effect increases the charge carrier concentration, leading to increased electrical conductivity (σ). Whilst the charge transport can cause de-doping at the

composite interface, and results in a high Seebeck coefficient (S). The combined effects of σ and S contribute to enhancing the power factors of hybrid composites.

Surface Modification of Nanowires: In Chapter 4, we demonstrated a significant enhancement in the thermoelectric (TE) properties of Tellurium nanowires (TeNWs) by modifying the surface of the TeNWs using sulfur moieties. The material characterization such as EDX, XPS exhibited that the surface modification effectively reduced oxidation within the TeNWs matrix. Temperature dependent thermoelectric transport properties measurements were conducted on thin films of TeNWs and Surface modified TeNWs (S^{2-}TeNWs). For both TeNWs and S^{2-}TeNWs films we observed that increasing the temperature decreases the Seebeck coefficient, while electrical conductivities show a steady increase, from 0.12 ± 0.09 S/cm at 300K to 7 ± 1 S/cm at 560K for TeNWs and 0.12 ± 0.03 to 14 ± 1 S/cm for S^{2-}TeNWs films. This leads to a peak power factor of 42 ± 3 μW/mK^2 and 87 ± 3 μW/mK^{2}at 560K for TeNWs and S^{2-}TeNWs, respectively. Hall measurement demonstrated a slightly higher carrier concentration throughout the temperature range 300K - 400K in S^{2-}TeNWs films compared to TeNWs films, which leads to a slightly lower Seebeck coefficient. At room temperature, the carrier concentration was about ~ 3-5 x10^{17}cm^{-3} for S^{2-}TeNWs films and ~ 2 x10^{17} cm^{-3} for TeNWs films. On the other hand, mobility increases with temperature in both systems. This increase in mobility further enhances the electrical conductivity in both TeNWs and S^{2-}TeNWs films.

We further mechanically mix surface modified nanowires (S^{2-}TeNWs) with a conducting polymer (P3HT) to fabricate robust composite hybrid materials to investigate on charge transport mechanism and their thermoelectric properties. Transport properties as a function of NWs (wt%) concentration indicated optimum composition of hybrid composite films was $S^{2-}Te_{80}$-$P3HT_{20}$. The optimum doping level achieved in S^{2-}TeNWs-P3HT system was 0.03M with p-type dopant $FeCl_3$. At 0.03M doping, hybrid films of $S^{2-}Te_{80}$-$P3HT_{20}$ exhibited the maximum performance of 78 μW/mK^2 with electrical conductivity values of 35 S/cm and Seebeck coefficient of 150 μV/K at room temperature. Moreover, an optimum interfacial barrier height of 0.72 eV was found for 0.03M $FeCl_3$ doped hybrid composites. Based on our findings we demonstrate that surface modification of nanostructures can be an effective way of improving the TE transport properties of composite hybrid materials. This methodology could be implied to other high performing nanostructured materials with various conducting polymers in future work.

Nanowire length and Polymer Molecular Weight: In Chapter 5, we adopted a third strategy to improve the charge transport at interfaces and to enhance the thermoelectric properties of hybrid composites. We demonstrated that the thermoelectric (TE) properties of P3HT-TeNWs hybrid systems can be significantly improved by increasing the length of the nanowires and using a high molecular weight polymer, both of which enhance the templating effect. We scaled up the ASS

reaction and synthesized longer TeNWs of length about 13 µm with an average diameter of 60 nm. To fabricate hybrid composites for thermoelectric properties investigation, we embedded these longer NWs into P3HT of two different molecular weights of 50-70kDa and 80-143kDa. The uniform conformal coating of P3HT on TeNWs was confirmed through TEM analysis for hybrid composite systems. On measuring the thermoelectric transport properties, we observed that TeNWs- P3HT (50-70kDa) showed optimal composition of Te_{80}-$P3HT_{20}$ with σ of 136 S/cm, S values of 135 µV/K and power factor of 248 µW/mK^2. The optimum doping of 0.03M $FeCl_3$ was observed in this composite system. The composite hybrid system of TeNWs- P3HT (80-143kDa) depicted the similar optimum composition of Te_{80}-$P3HT_{20}$. However, this hybrid system exhibited a slightly lower electrical conductivity of 91 S/cm, and higher Seebeck coefficient values of 183 µV/K compared to TeNWs- P3HT (50-70kDa) hybrid system. Nevertheless, the maximum power factor of 303 µW/mK^2 was achieved in TeNWs- P3HT (80-143kDa) hybrid system at an optimum doping of 0.02M.

The high performing hybrid composite [Te-P3HT (80-143kDa)] was utilized to perform thermal conductivity measurements, and it exhibited a thermal conductivity (κ) of 0.25 W/m-K, leading to a zT value of 0.36. The interfacial barrier height between NWs and P3HT at 0.02M $FeCl_3$ doping showed 0.09eV values that is below the theoretical threshold (≤0.2 eV) reported in literature to achieve the highest PF of composite materials. For clear understanding of charge transport (CT) in TeNWs-P3HT (80-143kDa) hybrid system, Kang and Snyder CT model was utilised. The energy independent parameter σ_{E0} was found to be 0.15 S/cm, which confirmed the strong templating of higher molecular weight P3HT on the TeNWs surface. This templating enhances the charge carrier concentration, leading to increased electrical conductivity. However, the charge transport induces de-doping at interface, and this results in high S. Finally, the composite hybrid materials exhibit the higher power factors.

Finally, we developed a unipolar (three-leg) p-type flexible thermoelectric device by drop-casting TeNWs-P3HT hybrid composite materials (thickness of film ~ 7.3 µm) onto a Kapton substrate, as shown in Figure 6.1. The device was dried overnight at 100 °C and subsequently doped using a 0.03M $FeCl_3$/acetonitrile solution. It produced an output voltage of 116 mV with a temperature difference of 40 °C after 40 seconds, achieving an output power of 2.23 nW/cm^2.

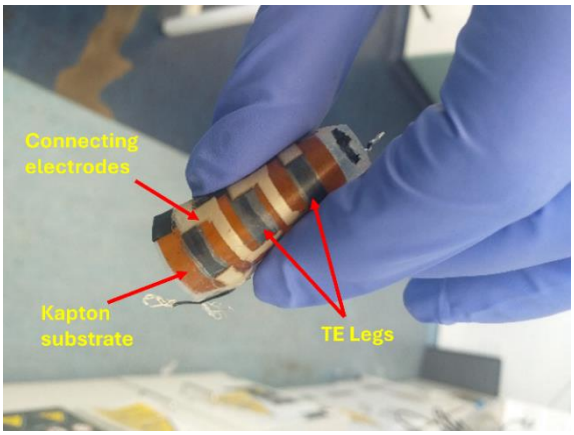

Figure 6.1. Unipolar flexible thermoelectric device fabricated by drop-casting TeNWs-P3HT hybrid composite onto a Kapton substrate.

Overall, this dissertation has advanced our understanding of the charge transport mechanisms at the interfaces of organic-inorganic hybrid composites and provided effective strategies for enhancing their thermoelectric properties. The findings underscore the importance of interface engineering, surface modification, and material selection in designing high-performance thermoelectric materials. These insights pave the way for future research on the development of next-generation hybrid composites with tailored properties for energy harvesting applications.

6.2 Future Work

Future work in the development of hybrid thermoelectric materials for energy harvesting in wearable devices should focus on several key areas to enhance their performance and practicality. Although these materials are attractive due to their ease of fabrication, light weight, and flexibility, their current performance falls short of the requirements for practical application. To bridge this gap, new mechanisms within hybrid thermoelectric materials must be explored. Here, we propose several research directions for improving the thermoelectric properties of these hybrid composites.

The ASS reactions used for synthesizing nanostructures should be revisited. The goal is to achieve high-quality nanostructures without relying on highly toxic substances like hydrazine hydrate. This can be pursued by investigating the potential of Ethylene Glycol (EG) reduction reactions on precursor chemicals, as well as exploring safer reducing agents like ascorbic acid. While we have successfully grown Tellurium Nanowires (TeNWs) using ascorbic acid, the nanowires exhibited significant surface oxidation, likely due to the ascorbic acid being dissolved in deionized water. Further research should explore alternative solvents or conditions to minimize oxidation and improve nanowire quality.

For extending the work presented in this thesis could involve optimizing ASS reactions for synthesizing nanostructures of other high-performing inorganic materials, such as Bi_2Te_3, Bi_2Se_3, and SnSe. These optimized nanostructures could then be combined with suitable polymers to fabricate advanced hybrid composite materials. During fabrication, controlling the dimensionality of the nanostructures and the interface between the polymer and inorganic components is crucial, as these factors significantly influence carrier transport within the composites. Moreover, the transport behaviour at the interfaces between the nanostructures and polymers requires further investigation to better understand the thermal and electrical properties of these composites—a longstanding challenge in the field.

The interaction mechanisms between inorganic materials and polymers, as well as their impact on thermoelectric performance, remain under debate. Establishing a fundamental physical model to explain performance enhancement is difficult. Therefore, both theoretical and experimental analyses should be further developed to clarify these interactions. Additionally, the thermoelectric figure of merit (ZT) of current composites is too low for commercial use. Identifying strategies to enhance ZT values is essential for making these materials viable for real-world applications. Several strategies can help to achieve this, such as carefully designing the interface between nanocomposites, employing structural engineering techniques to create a carrier filtering effect, doping with other elements, modifying the polymers, and using other inorganic or organic fillers to create ternary or multi-component composites, can lead to higher ZT values.

From a practical perspective, designing flexible thermoelectric generators (FTEGs) will require optimizing the electronic properties of both p-type and n-type composite materials while ensuring they remain stretchable and flexible. In this context, developing stable n-type conducting polymers is particularly important, as current versions are not air-stable. Future work should address the synthesis of these polymers, as well as optimize their integration with n-type inorganic nanostructures to produce high-performance n-type composites. This will be crucial for improving the overall thermoelectric properties of hybrid composites and advancing the development of flexible thermoelectric devices.

Appendix A [TEM images of TeNWs-P3HT Hybrid Composites]

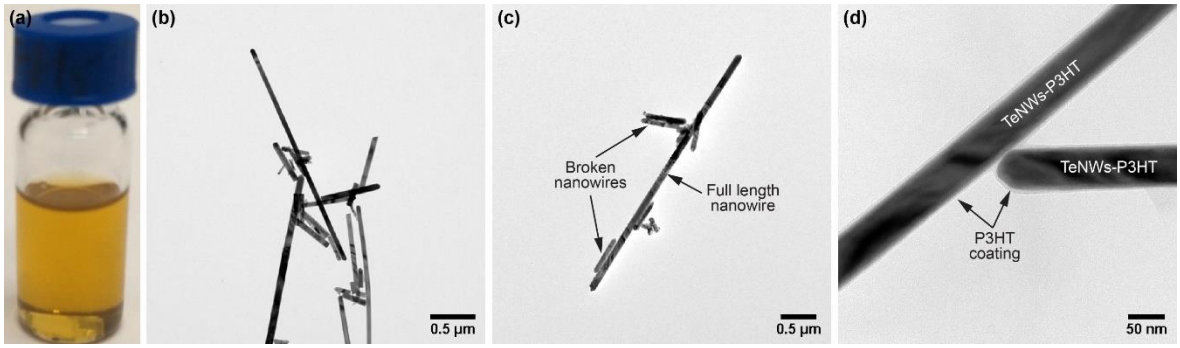

Figure A. 1. (a) Dilute dispersion solution of P3HT-TeNWs (50 wt.% TeNWs in P3HT matrix) nanocomposite in chloroform used to prepared grid samples and perform TEM characterization. (b), (c) and (d) Low-magnification TEM images of P3HT-TeNWs hybrid nanocomposites showing a few nanowires. The amorphous layer on the surface of nanowires in (d) indicates the conformal coating of polymer on nanowires.

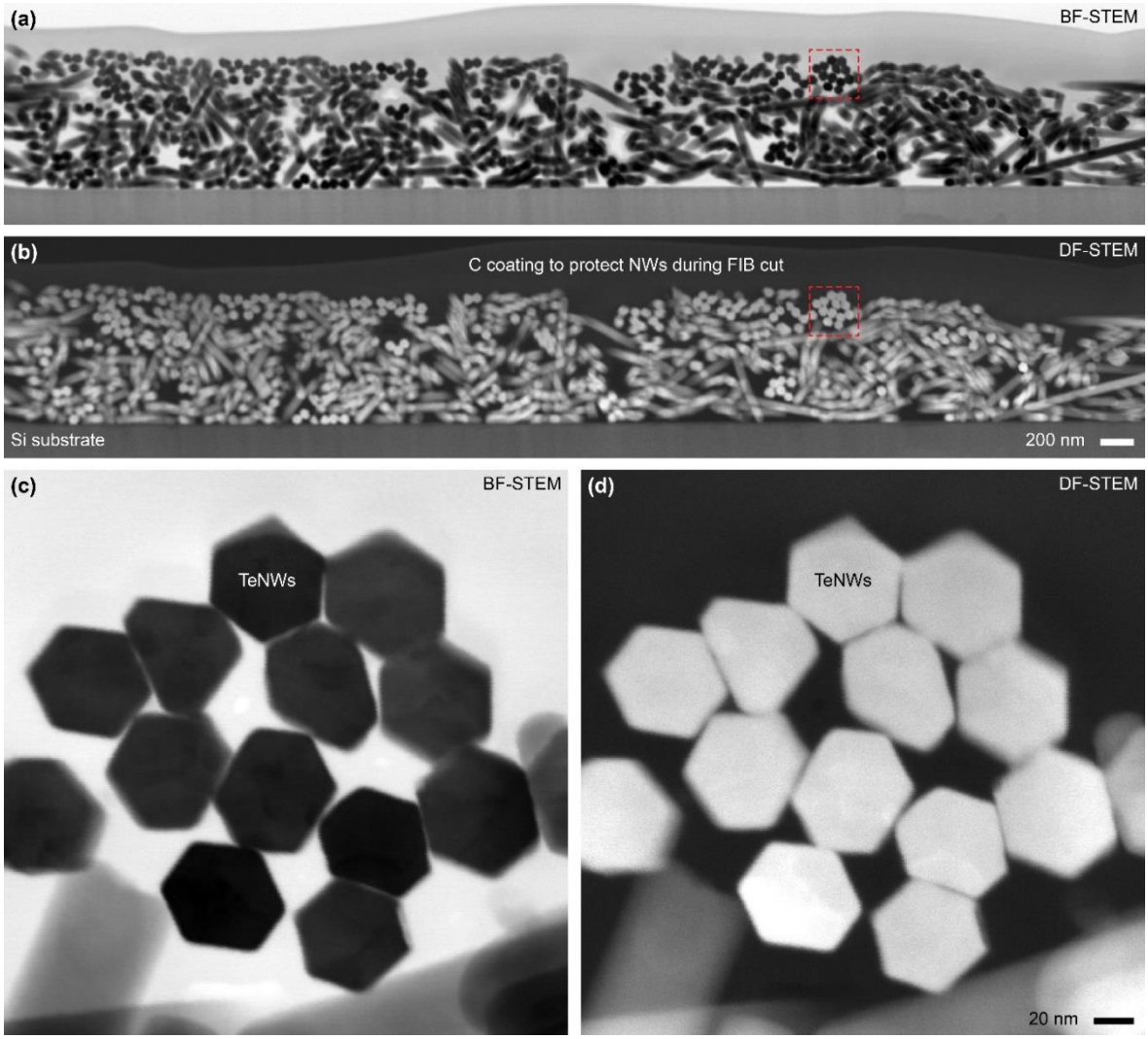

Figure A. 2. (a) Bright-field (BF) and (b) dark-field (DF) STEM images of TeNWs at low-magnification showing random distribution and texture of the NWs. High-magnification (c) BF-STEM and (d) DF-STEM images of TeNWs from selected areas (*red dotted squares*) showing a cross-sectional view of the NWs. Most of the NWs when seen in cross-section are in hexagonal shape with flat facets or edges and free from any contamination or oxidation.

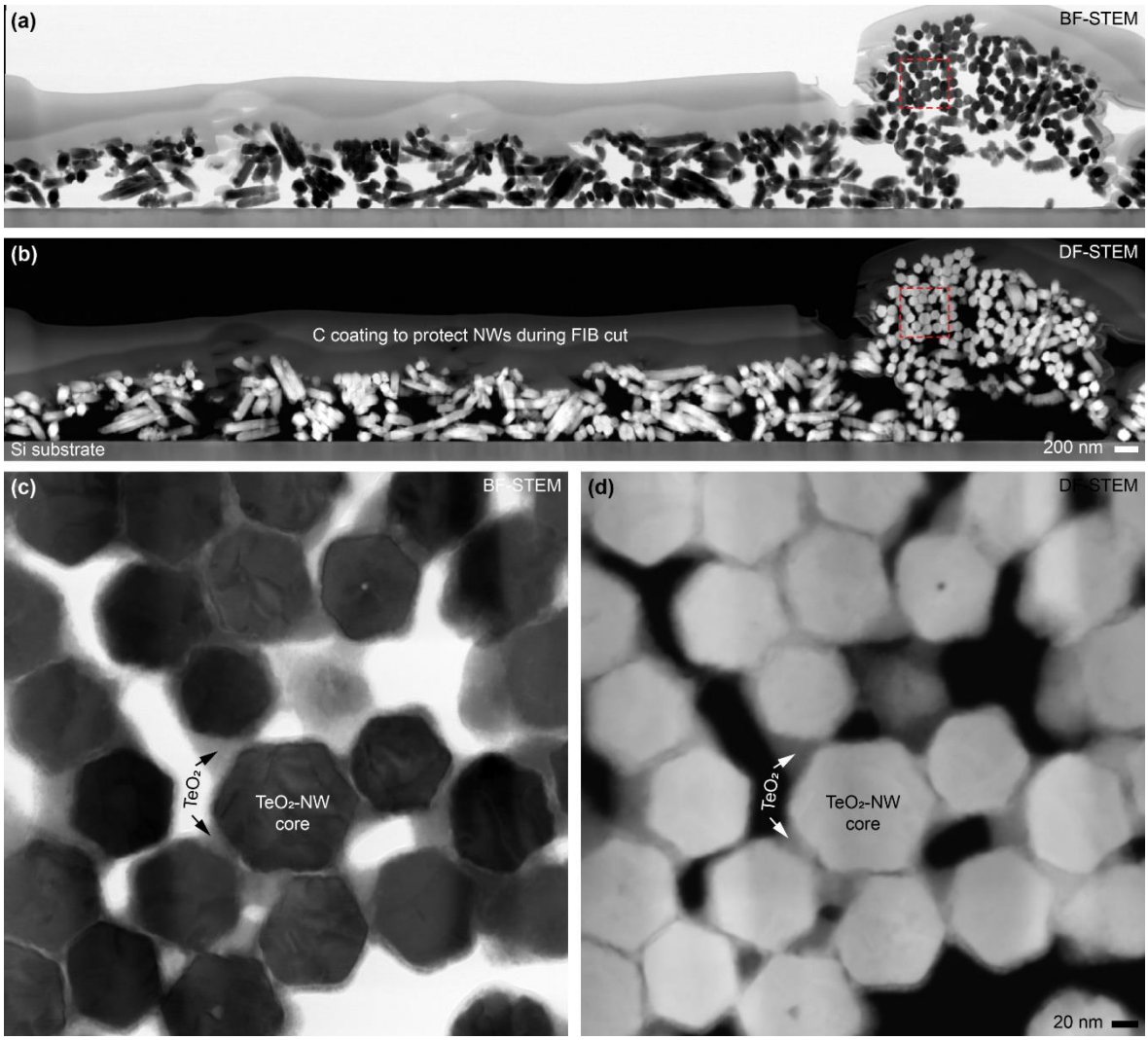

Figure A.3. (a) Bright-field (BF) and (b) dark-field (DF) STEM images of TeO_2-NWs at low-magnification showing random distribution and texture of the NWs. High-magnification (c) BF-STEM and (d) DF-STEM images of TeO_2-NWs from selected areas (*red dotted squares*) showing a cross-sectional view of the NWs. Most of the NWs when seen in cross-section are in hexagonal shape with flat facets or edges. However, in contrast to TeNWs, in this case we clearly see surface roughness due to surface oxidation.

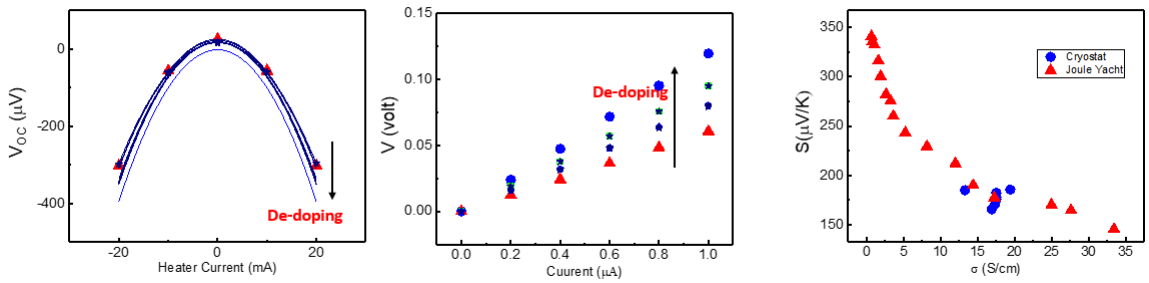

Figure A. 4. A comparison of TE properties measured via cryostat probe station and portable Seebeck Tester (PMT) on de-doping the 0.06M $FeCl_3$ hybrid film containing 90% Te and 10% P3HT.

In this study, we conducted thermoelectric measurements in ambient conditions utilizing a Seebeck coefficient Tester (PTM-3) manufactured by Wuhan Joule Yatch Technology. To ensure result consistency, we performed de-doping on hybrid films using a cryostat probe station. This allowed us to compare the results obtained with those from the PTM-3 and 4-probe as shown in Figure A.4

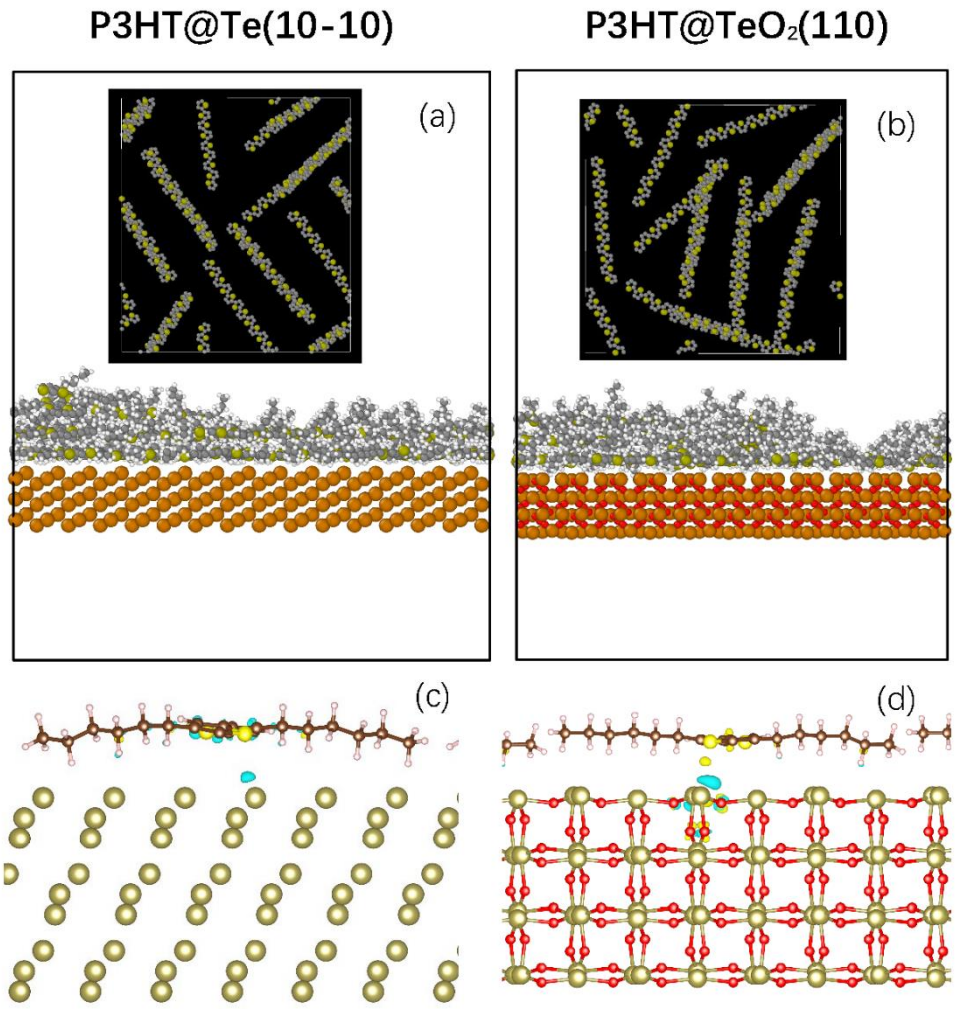

Figure A. 5. **MD simulation of P3HT polymer morphology and alignment at the organic-inorganic interface on Te and TeO_2 surface**. Here, the final polymer structures are depicted after

simulated annealing of five chains of P3HT on (a) Te (hexagonal) and (b) TeO_2 (tetragonal) surfaces. There is a high concentration of S atoms of P3HT observed at 3–5 Å from the nanowire surfaces, suggestive of highly ordered and aligned P3HT chains at the organic-inorganic interface. Although alignment occurs, self-assembly of chains is reduced on TeO_2 compared to the Te surface. (c) DFT calculations reveal electronic effects at the organic-inorganic interface. Electrons transfer from Te surface to P3HT chains monitored by increase of electron density (yellow) on P3HT and at the interface and decrease of electron density (cyan) at the Te phase. (d) Electron transfer from TeO_2 to P3HT. The iso-values in (c) and (d) are 10^{-3} and 2.5×10^{-3} $Å^{-3}$, respectively. Obviously, the amount of charge transfer is more significant in the case of TeO_2 substrate.

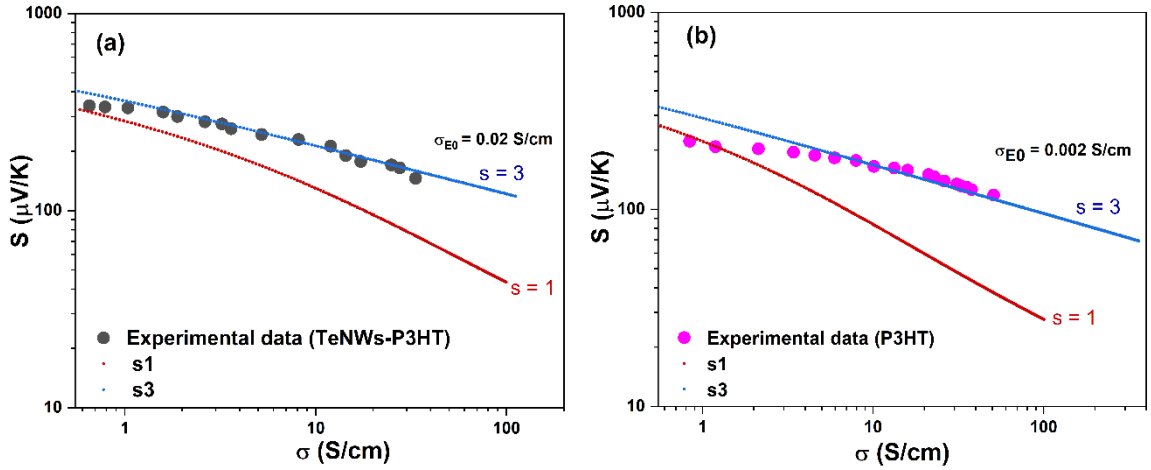

Figure A. 6. **Application of the Kang-Snyder charge transport model on composite and polymer materials**. Experimental data for Seebeck coefficient and electrical conductivity of (a) TeNW-P3HT composite, and (b) P3HT polymer, including curve fitting with the energy-dependent parameter "s".

Figure A.6 illustrates the curve fitting process for the data from the TeNWs-P3HT composite and the P3HT polymer using the Kang - Snyder charge transport model. The curve fitting was conducted using MATLAB simulations. The results indicate that the P3HT-based systems align best with the data, with an energy-dependent scattering parameter s = 3.

Appendix B [Thermoelectric Properties of Te-P3HT-P6 Hybrid Composites]

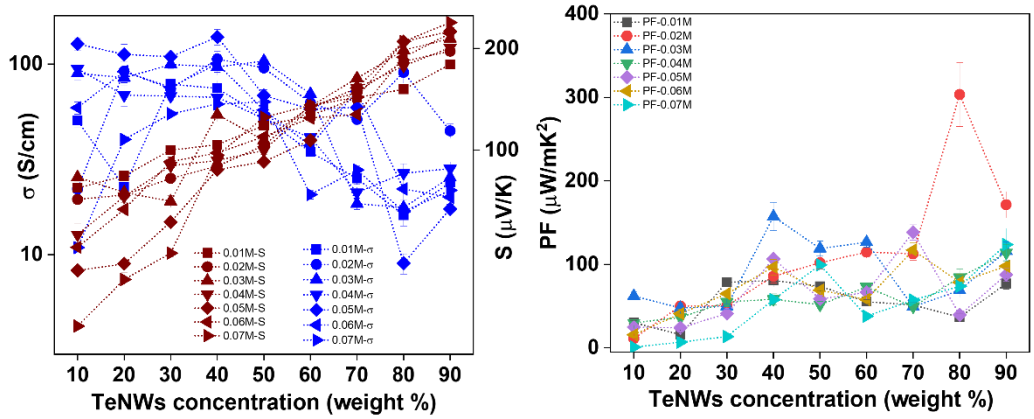

Figure B. Thermoelectric Properties of TeNWs-P3HT hybrid systems (a) conductivity and Seebeck coefficient, (b) power factor in nanocomposites, with high molecular weight of P3HT (80- 143kDa).

Long TeNWs were encapsulated in highest molecular weight of P3HT (80- 143kDa) by varying concentration of NWs into polymer matrix (10-90 wt%). Each composition of composites was doped with different molar concentration of $FeCl_3$ (10-70mM). The transport properties are measured as a function of NWs concentration, as Shown in Figure B.

Appendix C [Thermal Conductivity Measurements]

The LINSIES Thin Film Analyzer (TFA) was used to measure thermal conductivities of Hybrid composites for TeNWs-P3HT-P6 (80-143kDa). Three hysteresis from 20 °C to 100 °C were performed for each batch and three different measures was performed for the samples H2(Te_{80}-$P3HT_{20}$), and H3(Te_{70}-$P3HT_{30}$) and named as follows: H2 sample (H2.1, H2.2, H2.3), and H3 sample (H3.1, H3.2, H3.3). The thermal conductivities of the undoped and 0.02M- $FeCl_3$ doped samples of H2, and H3 are shown in Figure C. The Figure (c, f) represents the average Thermal conductivities of both samples.

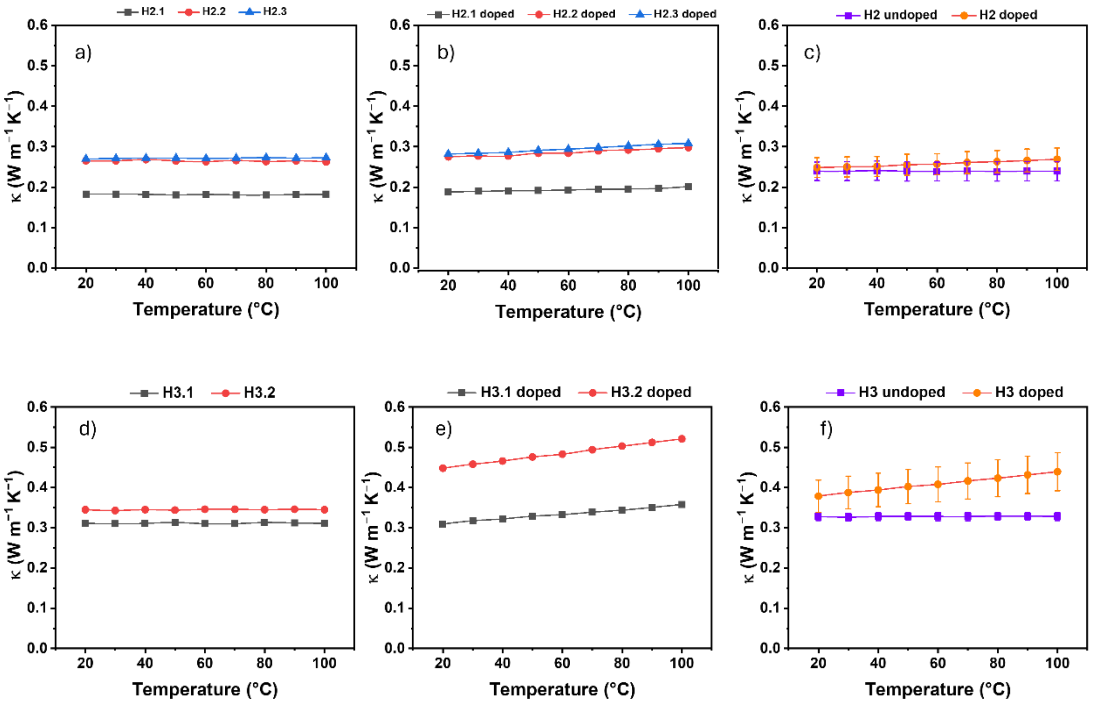

Figure C. Thermal conductivities of H2 and H3 samples (a & d) undoped (b & e) doped, (c & f) average undoped, and doped thermal conductivities.

Appendix D [Thermoelectric Properties of Conducting Polymers]

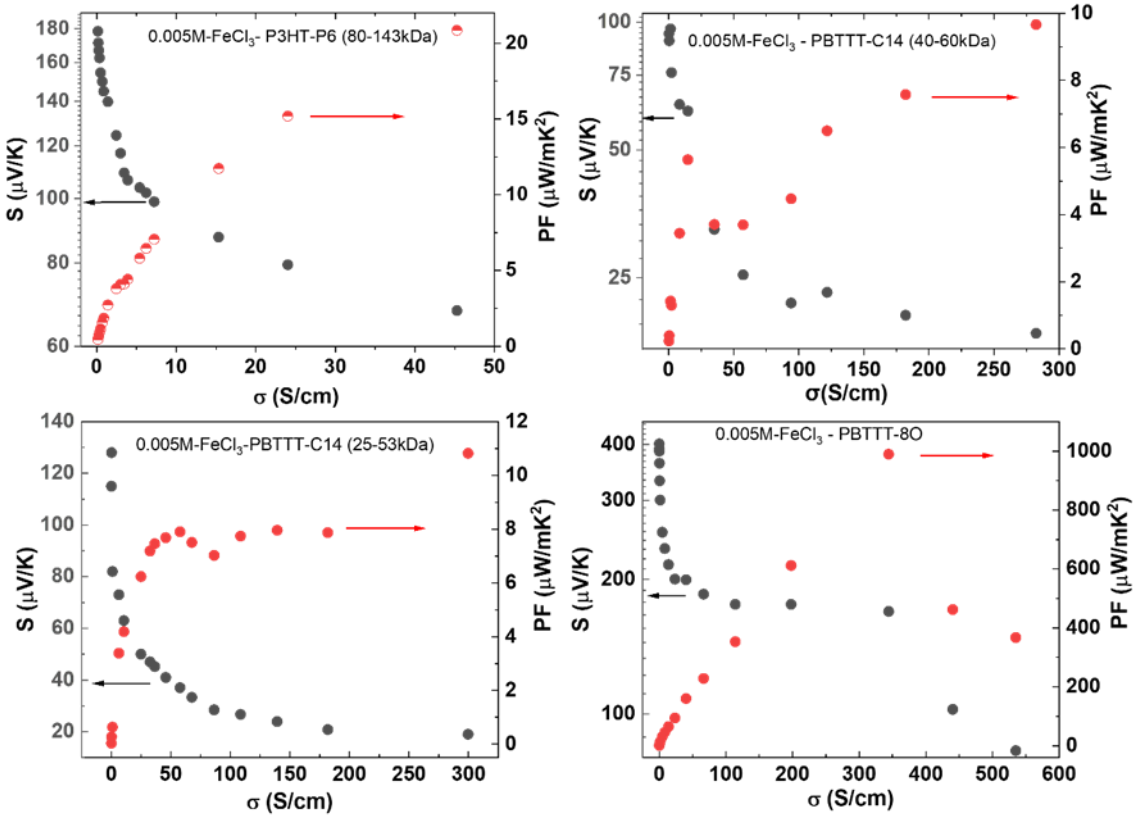

Figure D. 1. Thermoelectric properties of various conducting polymers doped in a 0.005M $FeCl_3$/acetonitrile solution. De-doping of each polymer film was conducted through heat treatment at 50°C, progressively removing dopants and reducing electrical conductivity.

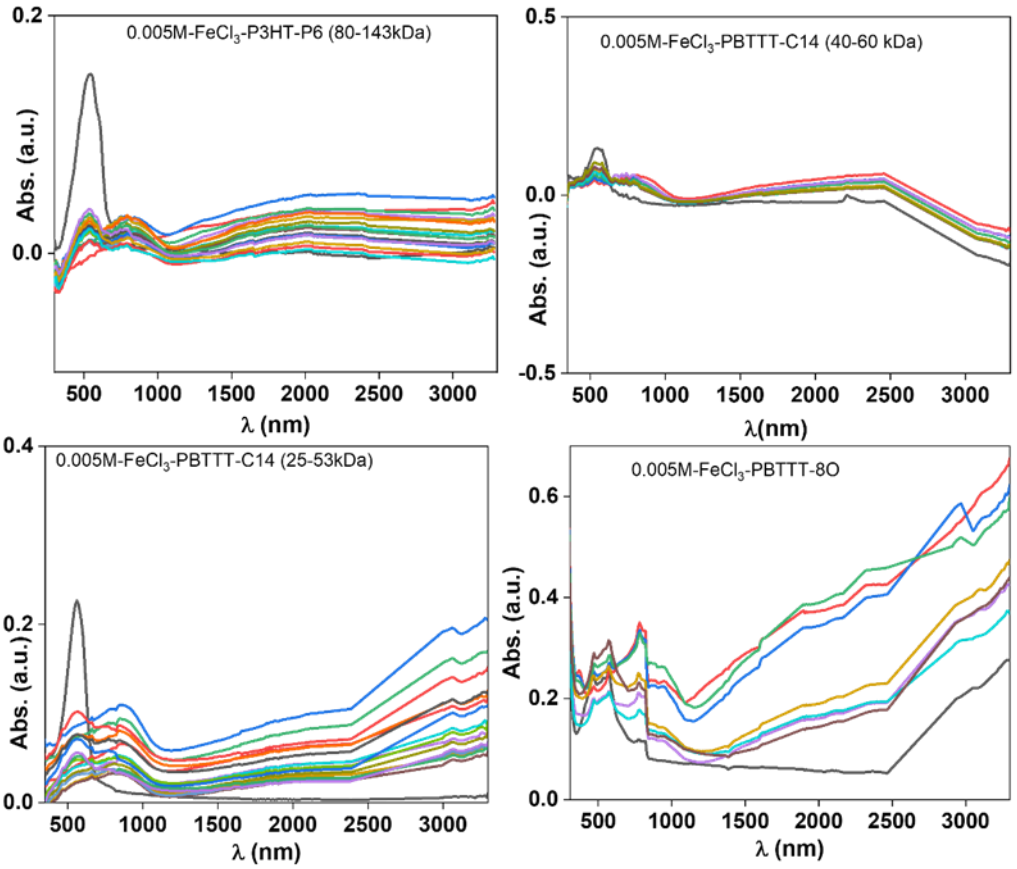

Figure D. 2. UV-Vis-NIR spectra of various conducting polymers, showing the polaron peaks. The spectra were recorded after each heating interval during the de-doping process of the conducting polymers.

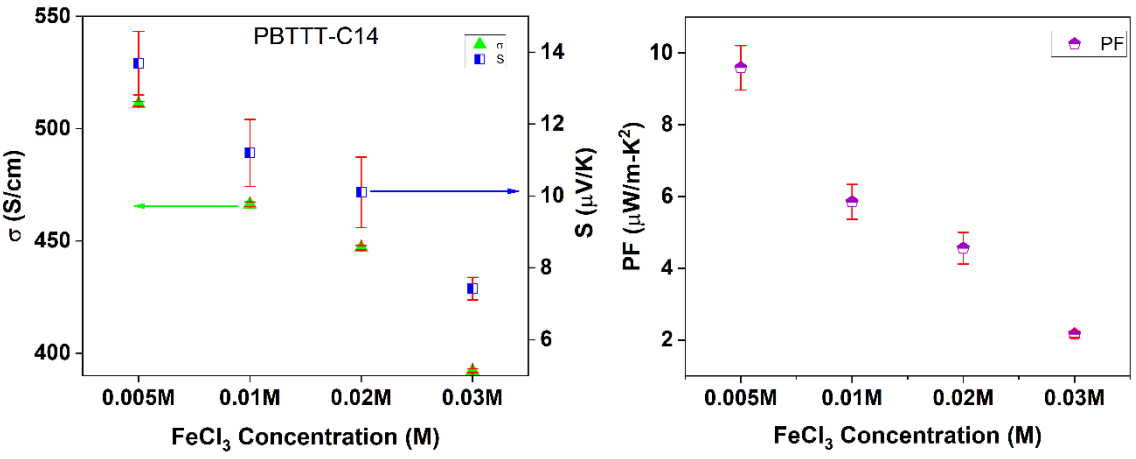

Figure D. 3. Doping level of the conducting polymer PBTTT-C14. Transport properties as a function of dopant concentration for PBTTT-C14 polymer films. The films of PBTTT-C14 exhibit optimum doping when treated with a low $FeCl_3$ concentration of 0.005 M. Vertical error bars (red colour) are standard deviation in measurements.

List of References

(1) Lockwood, M. The Political Sustainability of Climate Policy: The Case of the UK Climate Change Act. *Glob. Environ. Chang.* **2013**, *23* (5), 1339–1348. https://doi.org/10.1016/j.gloenvcha.2013.07.001.

(2) Freer, R.; Powell, A. V. Realising the Potential of Thermoelectric Technology: A Roadmap. *J. Mater. Chem. C* **2020**, *8* (2), 441–463. https://doi.org/10.1039/c9tc05710b.

(3) Wang, Y.; Yang, L.; Shi, X. L.; Shi, X.; Chen, L.; Dargusch, M. S.; Zou, J.; Chen, Z. G. Flexible Thermoelectric Materials and Generators: Challenges and Innovations. *Adv. Mater.* **2019**, *31* (29), 1–47. https://doi.org/10.1002/adma.201807916.

(4) Xu, S.; Shi, X. L.; Dargusch, M.; Di, C.; Zou, J.; Chen, Z. G. Conducting Polymer-Based Flexible Thermoelectric Materials and Devices: From Mechanisms to Applications. *Prog. Mater. Sci.* **2021**, *121* (December 2020), 100840. https://doi.org/10.1016/j.pmatsci.2021.100840.

(5) Cao, T.; Shi, X. L.; Zou, J.; Chen, Z. G. Advances in Conducting Polymer-Based Thermoelectric Materials and Devices. *Microstructures* **2021**, *1* (1). https://doi.org/10.20517/microstructures.2021.06.

(6) Toshima, N.; Oshima, K.; Anno, H.; Nishinaka, T.; Ichikawa, S.; Iwata, A.; Shiraishi, Y. Novel Hybrid Organic Thermoelectric Materials Three-Component Hybrid Films Consisting. *Adv. Mater.* **2015**, *27*, 2246–2251.

(7) Bharti, M.; Singh, A.; Samanta, S.; Aswal, D. K. Conductive Polymers for Thermoelectric Power Generation. *Prog. Mater. Sci.* **2018**, *93*, 270–310. https://doi.org/10.1016/j.pmatsci.2017.09.004.

(8) Hao, Y.; He, X.; Wang, L.; Qin, X.; Chen, G.; Yu, J. Stretchable Thermoelectrics: Strategies, Performances, and Applications. *Adv. Funct. Mater.* **2022**, *32* (13), 1–19. https://doi.org/10.1002/adfm.202109790.

(9) Liang, J.; Yin, S.; Wan, C. Hybrid Thermoelectrics. *Annu. Rev. Mater. Res.* **2020**, No. 50:319–44. https://doi.org/10.1146/annurev-matsci-082319.

(10) Riffat, S. B.; Ma, X. Thermoelectrics: A Review of Present and Potential Applications. *Appl. Therm. Eng.* **2003**, *23* (8), 913–935. https://doi.org/10.1016/S1359-4311(03)00012-7.

(11) Xiao Lei, S.; Jin, Z.; Zhi Gang, C. Advanced Thermoelectric Design: From Materials and Structures to Devices. *Chem. Rev.* **2020**, *120* (15), 7399–7515.

https://doi.org/10.1021/acs.chemrev.0c00026.

(12) Bell, L. E. Cooling, Heating, Generating Power, and Recovering Waste Heat with Thermoelectric Systems. *Science* **2008**, *321* (5895), 1457–1461. https://doi.org/10.1126/science.1158899.

(13) Elsheikh, M. H.; Shnawah, D. A.; Sabri, M. F.; Said, S. B.; Hassan, M. H.; Bashir, M. B.; Muhammad, M. A Review on Thermoelectric Renewable Energy: Principle Parameters That Affect Their Performance. *Renew. Sustain. Energy Rev.* **2014**, *30*, 337–355. https://doi.org/10.1016/j.rser.2013.10.027.

(14) Li. Jing-Feng; Wei-Shu, L.; Li-Dong, Z.; Min, Z. High-Performance Nanostructured Thermoelectric Materials. *NPG Asia Mater.* **2010**, *2* (4), 152.

(15) Snyder, G. J.; Toberer, E. S. Complex TE Meterials. *Nat. Mater.* **2008**, *7*, 105–114.

(16) Yang, L.; Chen, Z. G.; Dargusch, M. S.; Zou, J. High Performance Thermoelectric Materials: Progress and Their Applications. *Adv. Energy Mater.* **2018**, *8* (6), 1–28. https://doi.org/10.1002/aenm.201701797.

(17) Eom, Y.; Wijethunge, D.; Park, H.; Park, S. H.; Kim, W. Flexible Thermoelectric Power Generation System Based on Rigid Inorganic Bulk Materials. *Appl. Energy* **2017**, *206*, 649–656. https://doi.org/10.1016/j.apenergy.2017.08.231.

(18) Yang, C.; Kneib, M.; Lorenz, M.; Grundmann, M. Room-Temperature Synthesized Copper Iodide Thin Filmas Degenerate p-Type Transparent Conductor with a Boosted Figure of Merit. *Proc. Natl. Acad. Sci. U. S. A.* **2016**, *113* (46), 12929–12933. https://doi.org/10.1073/pnas.1613643113.

(19) Kim, C. S.; Lee, G. S.; Choi, H.; Kim, Y. J.; Yang, H. M.; Lim, S. H.; Lee, S. G.; Cho, B. J. Structural Design of a Flexible Thermoelectric Power Generator for Wearable Applications. *Appl. Energy* **2018**, *214*, 131–138. https://doi.org/10.1016/j.apenergy.2018.01.074.

(20) Chen, A.; Madan, D.; Wright, P. K.; Evans, J. W. Dispenser-Printed Planar Thick-Film Thermoelectric Energy Generators. *J. Micromechanics Microengineering* **2011**, *21* (10). https://doi.org/10.1088/0960-1317/21/10/104006.

(21) Roth, R.; Rostek, R.; Cobry, K.; Kohler, C.; Groh, M.; Woias, P. Design and Characterization of Micro Thermoelectric Cross-Plane Generators with Electroplated Bi_2Te_3, Sb_xTe_y, and Reflow Soldering. *J. Microelectromechanical Syst.* **2014**, *23* (4), 961–971. https://doi.org/10.1109/JMEMS.2014.2303198.

(22) Lu, Z.; Zhang, H.; Mao, C.; Li, C. M. Silk Fabric-Based Wearable Thermoelectric Generator for Energy Harvesting from the Human Body. *Appl. Energy* **2016**, *164*, 57–63. https://doi.org/10.1016/j.apenergy.2015.11.038.

(23) Shi, Y.; Wang, Y.; Mei, D.; Feng, B.; Chen, Z. Design and Fabrication of Wearable Thermoelectric Generator Device for Heat Harvesting. *IEEE Robot. Autom. Lett.* **2018**, *3* (1), 373–378. https://doi.org/10.1109/LRA.2017.2734241.

(24) Wang, Y.; Shi, Y.; Mei, D.; Chen, Z. Wearable Thermoelectric Generator to Harvest Body Heat for Powering a Miniaturized Accelerometer. *Appl. Energy* **2018**, *215*, 690–698. https://doi.org/10.1016/j.apenergy.2018.02.062.

(25) Wen, D. L.; Deng, H. T.; Liu, X.; Li, G. K.; Zhang, X. R.; Zhang, X. S. Wearable Multi-Sensing Double-Chain Thermoelectric Generator. *Microsystems Nanoeng.* **2020**, *6* (1). https://doi.org/10.1038/s41378-020-0179-6.

(26) Liu, D.; Zhao, Y.; Yan, Z.; Zhang, Z.; Zhang, Y.; Shi, P.; Xue, C. Screen-Printed Flexible Thermoelectric Device Based on Hybrid Silver Selenide/PVP Composite Films. *Nanomaterials* **2021**, *11* (8), 1–10. https://doi.org/10.3390/nano11082042.

(27) Park, D.; Kim, M.; Kim, J. High-Performance PANI-Coated Ag_2Se Nanowire and PVDF Thermoelectric Composite Film for Flexible Energy Harvesting. *J. Alloys Compd.* **2021**, *884*, 161098. https://doi.org/10.1016/j.jallcom.2021.161098.

(28) Wei, Q.; Mukaida, M.; Kirihara, K.; Naitoh, Y.; Ishida, T. Polymer Thermoelectric Modules Screen-Printed on Paper. *RSC Adv.* **2014**, *4* (54), 28802–28806. https://doi.org/10.1039/c4ra04946b.

(29) Fang, H.; Bhooshan C. Popere, E. M. T.; Mai, C.-K.; Chang, W. B.; Guillermo C. Bazan, Michael L. Chabinyc, R. A. S. Large-scale Integration of Flexible Materials into Rolled and Corrugated Thermoelectric Modules. *Appl. Polym. Sci.* **2017**, 1–7. https://doi.org/10.1002/APP.44208.

(30) Lee, W.; Kang, Y. H.; Lee, J. Y.; Jang, K. S.; Cho, S. Y. Hot-Pressing for Improving Performance of CNT/Conjugated Polymer Thermoelectric Films and Power Generators. *Mater. Today Commun.* **2017**, *10*, 41–45. https://doi.org/10.1016/j.mtcomm.2016.12.002.

(31) Bae, E. J.; Kang, Y. H.; Lee, C.; Cho, S. Y. Engineered Nanocarbon Mixing for Enhancing the Thermoelectric Properties of a Telluride-PEDOT:PSS Nanocomposite. *J. Mater. Chem. A* **2017**, *5* (34), 17867–17873. https://doi.org/10.1039/c7ta04280a.

(32) Song, H.; Qiu, Y.; Wang, Y.; Cai, K.; Li, D.; Deng, Y.; He, J. Polymer/Carbon Nanotube Composite Materials for Flexible Thermoelectric Power Generator. *Compos. Sci. Technol.* **2017**, *153*, 71–83. https://doi.org/10.1016/j.compscitech.2017.10.006.

(33) Bae, E. J.; Hun, Kang, Y. H.; Jang, K. S.; Cho, S. Y. Enhancement of Thermoelectric Properties of PEDOT:PSS and Tellurium-PEDOT:PSS Hybrid Composites by Simple Chemical Treatment. *Sci. Rep.* **2016**, *6*, 1–10. https://doi.org/10.1038/srep18805.

(34) Wang, X.; Meng, F.; Tang, H.; Gao, Z.; Li, S.; Jin, S.; Jiang, Q.; Jiang, F.; Xu, J. Design and Fabrication of Low Resistance Palm-Power Generator Based on Flexible Thermoelectric Composite Film. *Synth. Met.* **2018**, *235*, 42–48. https://doi.org/10.1016/j.synthmet.2017.11.010.

(35) Ferhat, S.; Domain, C.; Vidal, J.; Noël, D.; Ratier, B.; Lucas, B. Organic Thermoelectric Devices Based on a Stable N-Type Nanocomposite Printed on Paper. *Sustain. Energy Fuels* **2018**, *2* (1), 199–208. https://doi.org/10.1039/c7se00313g.

(36) Mei, J.; Diao, Y.; Appleton, A. L.; Fang, L.; Bao, Z. Integrated Materials Design of Organic Semiconductors for Field-Effect Transistors. *J. Am. Chem. Soc.* **2013**, *135* (18), 6724–6746. https://doi.org/10.1021/ja400881n.

(37) Bai, H.; Shi, G. Gas Sensors Based on Conducting Polymers. *Sensors* **2007**, *7*, 267–307. https://doi.org/10.4018/978-1-5225-1798-6.ch022.

(38) Forrest, S. R. The Path to Ubiquitous and Low-Cost Organic Electronic Appliances on Plastic. *Nature* **2004**, *428* (6986), 911–918.

(39) Murad, A. R.; Iraqi, A.; Aziz, S. B.; Abdullah, S. N.; Brza, M. A. Conducting Polymers for Optoelectronic Devices and Organic Solar Cells: A Review. *Polymers (Basel).* **2020**, *12* (11), 1–47. https://doi.org/10.3390/polym12112627.

(40) Russ, B.; Glaudell, A.; Urban, J. J.; Chabinyc, M. L.; Segalman, R. A. Organic Thermoelectric Materials for Energy Harvesting and Temperature Control. *Nat. Rev. Mater.* **2016**, *1* (10). https://doi.org/10.1038/natrevmats.2016.50.

(41) Glaudell, A. M.; Cochran, J. E.; Patel, S. N.; Chabinyc, M. L. Impact of the Doping Method on Conductivity and Thermopower in Semiconducting Polythiophenes. *Adv. Energy Mater.* **2015**, *5* (4). https://doi.org/10.1002/aenm.201401072.

(42) Gupta, S. K.; Jha, P.; Singh, A.; Chehimi, M. M.; Aswal, D. K. Flexible Organic Semiconductor Thin Films. *J. Mater. Chem. C* **2015**, *3* (33), 8468–8479.

https://doi.org/10.1039/c5tc00901d.

(43) Han, C.; Li, Z.; Dou, S. X. Recent Progress in Thermoelectric Materials. *Chinese Sci. Bull.* **2014**, *59* (18), 2073–2091.

(44) Bharti, M.; Jha, P.; Singh, A.; Chauhan, A. K.; Misra, S.; Yamazoe, M.; Debnath, A. K.; Marumoto, K.; Muthe, K. P.; Aswal, D. K. Scalable Free-Standing Polypyrrole Films for Wrist-Band Type Flexible Thermoelectric Power Generator. *Energy* **2019**, *176*, 853–860. https://doi.org/10.1016/j.energy.2019.04.013.

(45) Liu, S.; Li, H.; Li, P.; Liu, Y.; He, C. Recent Advances in Polyaniline-Based Thermoelectric Composites. *CCS Chem.* **2021**, *3* (10), 2547–2560. https://doi.org/10.31635/ccschem.021.202101066.

(46) Shengduo, X.; Min, H.; Xiao-Lei, S.; Yuan, W.; Lei, G.; Yang, B.; Lianzhou, W.; Matthew, D.; Jin, Z.; Zhi-Gang, C. High-Performance PEDOT:PSS Flexible Thermoelectric Materials and Their Devices by Triple Post-Treatments. *Chem. Mater.* **2019**, *31* (14), 5238–5244. https://doi.org/10.1021/acs.chemmater.9b01500.

(47) Xuan, Y.; Liu, X.; Desbief, S.; Leclère, P.; Fahlman, M.; Lazzaroni, R.; Berggren, M.; Cornil, J.; Emin, D.; Crispin, X. Thermoelectric Properties of Conducting Polymers : The Case of Poly (3-Hexylthiophene). *Phys. Rev.* **2010**, *B 82*, 1–9. https://doi.org/10.1103/PhysRevB.82.115454.

(48) Kim, G. H.; Shao, L.; Zhang, K.; Pipe, K. P. Engineered Doping of Organic Semiconductors for Enhanced Thermoelectric Efficiency. *Nat. Mater.* **2013**, *12* (8), 719–723. https://doi.org/10.1038/nmat3635.

(49) Jeong, M. H.; Sanger, A.; Kang, S. B.; Jung, Y. S.; Oh, I. S.; Yoo, J. W.; Kim, G. H.; Choi, K. J. Increasing the Thermoelectric Power Factor of Solvent-Treated PEDOT:PSS Thin Films on PDMS by Stretching. *J. Mater. Chem. A* **2018**, *6* (32), 15621–15629. https://doi.org/10.1039/c8ta03606c.

(50) Yemata, T. A.; Zheng, Y.; Kyaw, A. K. K.; Wang, X.; Song, J.; Chin, W. S.; Xu, J. Modulation of the Doping Level of PEDOT:PSS Film by Treatment with Hydrazine to Improve the Seebeck Coefficient. *RSC Adv.* **2020**, *10* (3), 1786–1792. https://doi.org/10.1039/c9ra07648d.

(51) Untilova, V.; Zeng, H.; Durand, P.; Herrmann, L.; Leclerc, N.; Brinkmann, M. Intercalation and Ordering of F_6TCNNQ and F_4TCNQ Dopants in Regioregular Poly(3-Hexylthiophene) Crystals: Impact on Anisotropic Thermoelectric Properties of Oriented Thin Films.

Macromolecules **2021**, *54* (13), 6073–6084. https://doi.org/10.1021/acs.macromol.1c00554.

(52) Wu, L.; Li, H.; Chai, H.; Xu, Q.; Chen, Y.; Chen, L. Anion-Dependent Molecular Doping and Charge Transport in Ferric Salt-Doped P3HT for Thermoelectric Application. *ACS Appl. Electron. Mater.* **2021**, *3* (3), 1252–1259. https://doi.org/10.1021/acsaelm.0c01067.

(53) Untilova, V.; Biskup, T.; Biniek, L.; Vijayakumar, V.; Brinkmann, M. Control of Chain Alignment and Crystallization Helps Enhance Charge Conductivities and Thermoelectric Power Factors in Sequentially Doped P3HT:F_4TCNQ Films. *Macromolecules* **2020**, *53* (7), 2441–2453. https://doi.org/10.1021/acs.macromol.9b02389.

(54) Hynynen, J.; Kiefer, D.; Müller, C. Influence of Crystallinity on the Thermoelectric Power Factor of P3HT Vapour-Doped with F_4TCNQ. *RSC Adv.* **2018**, *8* (3), 1593–1599. https://doi.org/10.1039/c7ra11912g.

(55) Qu, S.; Yao, Q.; Wang, L.; Chen, Z.; Xu, K.; Zeng, H.; Shi, W.; Zhang, T.; Uher, C.; Chen, L. Highly Anisotropic P3HT Films with Enhanced Thermoelectric Performance via Organic Small Molecule Epitaxy. *NPG Asia Mater.* **2016**, *8* (7). https://doi.org/10.1038/am.2016.97.

(56) Lee, H. J.; Anoop, G.; Lee, H. J.; Kim, C.; Park, J. W.; Choi, J.; Kim, H.; Kim, Y. J.; Lee, E.; Lee, S. G.; Kim, Y. M.; Lee, J. H.; Jo, J. Y. Enhanced Thermoelectric Performance of PEDOT:PSS/PANI-CSA Polymer Multilayer Structures. *Energy Environ. Sci.* **2016**, *9* (9), 2806–2811. https://doi.org/10.1039/c5ee03063c.

(57) He, M.; Ge, J.; Lin, Z.; Feng, X.; Wang, X.; Lu, H.; Yang, Y.; Qiu, F. Thermopower Enhancement in Conducting Polymer Nanocomposites via Carrier Energy Scattering at the Organic-Inorganic Semiconductor Interface. *Energy Environ. Sci.* **2012**, *5* (8), 8351–8358. https://doi.org/10.1039/c2ee21803h.

(58) McCullough, R. D. The Chemistry of Conducting Polythiophenes. *Adv. Mater.* **1998**, *10* (2), 93–116. https://doi.org/10.1002/(SICI)1521-4095(199801)10:2<93::AID-ADMA93>3.0.CO;2-F.

(59) Abad, B.; Rull-Bravo, M.; Hodson, S.L.; Xu, X.; Martin-Gonzalez, M. Thermoelectric Properties of Electrodeposited Tellurium Films and the Sodium Lignosulfonate Effect. *Electrochim. Acta* **2015**, *169*, 37–45. https://doi.org/10.1016/j.electacta.2015.04.063.

(60) Oliveira, J.F.; Enderlein, C.; Fontes, M.B.; Baggio-Saitovitch, E. The Pressure-Dependence of the Band Gap of Tellurium. *J. Phys. Conf. Ser.* **2020**, *1609* (1).https://doi.org/10.1088/1742-

6596/1609/1/012013.

(61) He, Z.; Yang, Y.; Liu, J. W.; Yu, S. H. Emerging Tellurium Nanostructures: Controllable Synthesis and Their Applications. *Chem. Soc. Rev.* **2017**, *46* (10), 2732–2753. https://doi.org/10.1039/c7cs00013h.

(62) Yang, M.; Su, T.; Li, S.; Li, S.; Hu, M.; Liu, X. Facile Synthesis and High Thermoelectric Performance of Tellurium with Antimony Doping. *J. Alloys Compd.* **2021**, *887*, 161342. https://doi.org/10.1016/j.jallcom.2021.161342.

(63) Wang, Y.; Liu, S.; Wu, Z.; Liu, G.; Yang, X.; Wei, T.; Wang, Q.; Ye, Y.; Li, D.; Zhu, J. Enhanced Thermoelectric Performance of van Der Waals Tellurium via Vacancy Engineering. *Mater. Today Phys.* **2021**, *18*. https://doi.org/10.1016/j.mtphys.2021.100379.

(64) Jiang, Q.; Yang, J.; Hing, P.; Ye, H. Recent Advances, Design Guidelines, and Prospects of Flexible Organic/Inorganic Thermoelectric Composites. *Mater. Adv.* **2020**, *1* (5), 1038–1054. https://doi.org/10.1039/d0ma00278j.

(65) Yang, L.; Gordon, M. P.; Menon, A. K.; Bruefach, A.; Haas, K.; Scott, M. C.; Prasher, R. S.; Urban, J. J. Decoupling Electron and Phonon Transport in Single-Nanowire Hybrid Materials for High-Performance Thermoelectrics. *Sci. Adv.* **2021**, *7* (20), 18–20. https://doi.org/10.1126/sciadv.abe6000.

(66) Coates, N. E.; Yee, S. K.; McCulloch, B.; See, K. C.; Majumdar, A.; Segalman, R. A.; Urban, J. J. Effect of Interfacial Properties on Polymer-Nanocrystal Thermoelectric Transport. *Adv. Mater.* **2013**, *25* (11), 1629–1633.

(67) Kim, W. S.; Anoop, G.; Jeong, I. S.; Lee, H. J.; Kim, H. Bin; Kim, S. H.; Goo, G. W.; Lee, H.; Lee, H. J.; Kim, C.; Lee, J. H.; Mun, B. S.; Park, J. W.; Lee, E.; Jo, J. Y. Feasible Tuning of Barrier Energy in PEDOT:PSS/Bi_2Te_3 Nanowires-Based Thermoelectric Nanocomposite Thin Films through Polar Solvent Vapor Annealing. *Nano Energy* **2020**, *67*, 104207. https://doi.org/10.1016/j.nanoen.2019.104207.

(68) Wang, Y.; Zhang, S. M.; Deng, Y. Flexible Low-Grade Energy Utilization Devices Based on High-Performance Thermoelectric Polyaniline/Tellurium Nanorod Hybrid Films. *J. Mater. Chem. A* **2016**, *4* (9), 3554–3559.

(69) Wang, Y.; Liu, G.; Sheng, M.; Yu, C.; Deng, Y. Flexible Thermopower Generation over Broad Temperature Range by PANI/Nanorod Hybrid-Based p-n Couples. *J. Mater. Chem. A* **2019**, *7* (4), 1718–1724. https://doi.org/10.1039/c8ta11008e.

(70) Li, Y.; Gao, C. Y.; Fan, X. H.; Yang, L. M. Full-Electrochemical Construction of High-Performance Polypyrrole/Tellurium Thermoelectrical Nanocomposites. *ACS Appl. Mater. Interfaces* **2022**, *14* (8), 10815–10824. https://doi.org/10.1021/acsami.1c22731.

(71) Dresselhaus, M.S.; Chen, G.; Tang, M.Y.; Yang, R.G.; Lee, H.; Wang, D.Z.; Ren, Z.F.; Fleurial, J.P.; Gogna, P. New Directions for Low-Dimensional Thermoelectric Materials. *Adv. Mater.* **2007**, *19* (8), 1043–1053. https://doi.org/10.1002/adma.200600527.

(72) Zuev, Y.M.; Lee, J.S.; Galloy, C.; Park, H.; Kim, P. Diameter Dependence of the Transport Properties of Antimony Telluride Nanowires. *Nano Lett.* **2010**, *10* (8), 3037–3040. https://doi.org/10.1021/nl101505q.

(73) Tian, Y.; Sakr, M.R.; Kinder, J.M.; Liang, D.; MacDonald, M.J.; Qiu, R.L.; Gao, H.J.; Gao, X.P. One-Dimensional Quantum Confinement Effect Modulated Thermoelectric Properties in InAs Nanowires. *Nano Lett.* **2012**, *12* (12), 6492–6497. https://doi.org/10.1021/nl304194c.

(74) Kim, J.; Lee, S.; Brovman, Y. M.; Kim, P.; Lee, W. Diameter-Dependent Thermoelectric Figure of Merit in Single-Crystalline Bi Nanowires. *Nanoscale* **2015**, *7* (11), 5053–5059. https://doi.org/10.1039/c4nr06412g.

(75) Boukai, A. I.; Bunimovich, Y.; Kheli, J. T.; Yu, J. K.; Goddard, W. A.; Heath, J. R. Silicon Nanowires as Efficient Thermoelectric Materials. *Nature* **2008**, *451* (7175), 168–171. https://doi.org/10.1038/nature06458.

(76) Ali, A.; Chen, Y.; Vasiraju, V.; Vaddiraju, S. Nanowire-Based Thermoelectrics. *Nanotechnology* **2017**, *28* (28), 282001. https://doi.org/10.1088/1361-6528/aa75ae.

(77) Agarwal, R.; Lieber, C. M. Semiconductor Nanowires: Optics and Optoelectronics. *Appl. Phys. A Mater. Sci. Process.* **2006**, *85* (3), 209–215. https://doi.org/10.1007/s00339-006-3720-z.

(78) Mikolajick, T.; Heinzig, A.; Trommer, J.; Pregl, S.; Grube, M.; Cuniberti, G.; Weber, W. M. Silicon Nanowires - A Versatile Technology Platform. *Phys. Status Solidi - Rapid Res. Lett.* **2013**, *7* (10), 793–799. https://doi.org/10.1002/pssr.201307247.

(79) Baxter, J. B.; Aydil, E. S. Nanowire-Based Dye-Sensitized Solar Cells. *Appl. Phys. Lett.* **2005**, *86* (5), 1–3. https://doi.org/10.1063/1.1861510.

(80) Peng, K. Q.; Wang, X.; Li, L.; Hu, Y.; Lee, S. T. Silicon Nanowires for Advanced Energy Conversion and Storage. *Nano Today* **2013**, *8* (1), 75–97. https://doi.org/10.1016/j.nantod.2012.12.009.

(81) Wang, W.; Li, C.; Li, X.; Jia, Y.; Jiang, F.; Liu, C.; Tan, R.; Xu, J. Fabrication of Freestanding Tellurium Nanofilm and its Thermoelectric Performance. *Thin Solid Films* **2018**, *654*, 23–29. https://doi.org/10.1016/j.tsf.2018.03.073.

(82) Xiu, F.; He, L.; Wang, Y.; Cheng, L.; Chang, L. Te; Lang, M.; Huang, G.; Kou, X.; Zhou, Y.; Jiang, X.; Chen, Z.; Zou, J.; Shailos, A.; Wang, K. L. Manipulating Surface States in Topological Insulator Nanoribbons. *Nat. Nanotechnol.* **2011**, *6* (4), 216–221. https://doi.org/10.1038/nnano.2011.19.

(83) Zhang, G.; Kirk, B.; Jauregui, L. A.; Yang, H.; Xu, X.; Chen, Y. P.; Wu, Y. Rational Synthesis of Ultrathin n-Type Bi_2Te_3 Nanowires with Enhanced Thermoelectric Properties. *Nano Lett.* **2012**, *12* (1), 56–60. https://doi.org/10.1021/nl202935k.

(84) Dong, G. H.; Zhu, Y. J.; Chen, L. D. Sb_2Te_3 Nanostructures with Various Morphologies: Rapid Microwave Solvothermal Synthesis and Seebeck Coefficients. *CrystEngComm* **2011**, *13* (22), 6811–6816. https://doi.org/10.1039/c1ce05591g.

(85) Lee, S.; In, J.; Yoo, Y.; Jo, Y.; Park, Y. C.; Kim, H. J.; Koo, H. C.; Kim, B.; Wang, K. L. Single Crystalline β-Ag_2Te Nanowire as a New Topological Insulator. *Nano Lett.* **2012**, *12*, 4191–4199.

(86) Qiu, P.; Shi, X.; Chen, L. Cu-Based Thermoelectric Materials. *Energy Storage Mater.* **2016**, *3*, 85–97. https://doi.org/10.1016/j.ensm.2016.01.009.

(87) Xie, X.; Kwok, S. Y.; Lu, Z.; Liu, Y.; Cao, Y.; Luo, L.; Zapien, J. A.; Bello, I.; Lee, C. S.; Lee, S. T.; Zhang, W. Visible-NIR Photodetectors Based on CdTe Nanoribbons. *Nanoscale* **2012**, *4* (9), 2914–2919. https://doi.org/10.1039/c2nr30277b.

(88) Lee, S. H.; Shim, W.; Jang, S. Y.; Roh, J. W.; Kim, P.; Park, J.; Lee, W. Thermoelectric Properties of Individual Single-Crystalline PbTe Nanowires Grown by a Vapor Transport Method. *Nanotechnology* **2011**, *22* (29). https://doi.org/10.1088/0957-4484/22/29/295707.

(89) Peng, H.; Kioussis, N.; Snyder, G. J. Elemental Tellurium as a Chiral p -Type Thermoelectric Material. *Phys. Rev. B - Condens. Matter Mater. Phys.* **2014**, *89* (19), 1–7. https://doi.org/10.1103/PhysRevB.89.195206.

(90) Lin, S.; Li, W.; Chen, Z.; Shen, J.; Ge, B.; Pei, Y. Tellurium as a High-Performance Elemental Thermoelectric. *Nat. Commun.* **2016**, *7*, 1–6. https://doi.org/10.1038/ncomms10287.

(91) Duan, X.; Huang, Y.; Cui, Y.; Wang, J.; Lieber, C. M. Indium Phosphide Nanowires as Building

Blocks for Nanoscale Electronic and Optoelectronic Devices. *Nature* **2001**, *409* (6816), 66–69. https://doi.org/10.1038/35051047.

(92) Huynh, W. U.; Dittmer, J. J.; Alivisatos, A. P. Hybrid Nanorod-Polymer Solar Cells. *Science* **2002**, *295* (March), 2425–2427.

(93) Park, H.; Son, W.; Lee, S. H.; Kim, S.; Lee, J. J.; Cho, W.; Choi, H. H.; Kim, J. H. Aqueous Chemical Synthesis of Tellurium Nanowires Using a Polymeric Template for Thermoelectric Materials. *CrystEngComm* **2015**, *17* (5), 1092.

(94) Mayers, B.; Xia, Y. One-Dimensional Nanostructures of Trigonal Tellurium with Various Morphologies can be Synthesized using a Solution-Phase Approach. *J. Mater. Chem.* **2002**, *12* (6), 1875–1881. https://doi.org/10.1039/b201058e.

(95) Mo, M.; Zeng, J.; Liu, X.; Yu, W.; Zhang, S.; Qian, Y. Controlled Hydrothermal Synthesis of Thin Single-Crystal Tellurium Nanobelts and Nanotubes. *Adv. Mater.* **2002**, *14* (22), 1658–1662.

(96) Liu, Z.; Li, S.; Yang, Y.; Hu, Z.; Peng, S.; Liang, J.; Qian, Y. Shape-Controlled Synthesis and Growth Mechanism of One-Dimensional Nanostructures of Trigonal Tellurium. *New J. Chem.* **2003**, *27* (12), 1748–1752. https://doi.org/10.1039/b306782c.

(97) Lu, Q.; Gao, F.; Komarneni, S. Biomolecule-Assisted Reduction in the Synthesis of Single-Crystalline Tellurium Nanowires. *Adv. Mater.* **2004**, *16* (18), 1629–1632. https://doi.org/10.1002/adma.200400319.

(98) Zhu, Y.; Wang, W.; Qi, R.; Hu, X. Microwave-Assisted Synthesis of Single-Crystalline Tellurium Nanorods and Nanowires in Ionic Liquids. *Angew. Chemie* **2004**, *116* (11), 1434–1438. https://doi.org/10.1002/ange.200353101.

(99) Mohanty, P.; Park, J.; Lee, G.; Kim, B. Fabrication of Single Crystalline Cadmium Nanowires by a Facile Low Temperature Vapor Phase Method. *J. Nanosci. Nanotechnol.* **2006**, *6* (11), 3376–3379. https://doi.org/10.1166/jnn.2006.014.

(100) Silva, R. R.; Mejia, H. A. G.; Ribeiro, S. J. L.; Shrestha, L. K.; Ariga, K.; Oliveira Jr., O. N.; Camargo,V. R.; Maia, L. J. Q.; Araujo C. B. Facile Synthesis of Tellurium Nanowires and Study of Their Third-Order Nonlinear Optical Properties. *J. Braz. Chem. Soc.* **2017**, *28* (1), 58–67.

(101) Stavila, V.; Robinson, D. B.; Hekmaty, M. A.; Nishimoto, R.; Medlin, D. L.; Zhu, S.; Tritt, T. M.; Sharma, P. A. Wet-Chemical Synthesis and Consolidation of Stoichiometric Bismuth

Telluride Nanoparticles for Improving the Thermoelectric Figure-of-Merit. *ACS Appl. Mater. Interfaces* **2013**, *5* (14), 6678–6686. https://doi.org/10.1021/am401444w.

(102) Zhang, B.; Hou, W.; Ye, X.; Fu, S.; Xie, Y. 1D Tellurium Nanostructures Photothermally Assisted Morphology-Controlled Synthesis AND Application in Preparing Functional Nanoscale Materials. *Adv. Funct. Mater.* **2007**, *17*, 486–492.

(103) Wang, T.; Liu, C.; Xu, J.; Zhu, Z.; Liu, E.; Hu, Y.; Li, C.; Jiang, F. Thermoelectric Performance of Restacked MoS_2 Nanosheets Thin-Film. *Nanotechnology* **2016**, *27* (28). https://doi.org/10.1088/0957-4484/27/28/285703.

(104) Yee, S. K.; Coates, N. E.; Majumdar, A.; Urban, J. J.; Segalman, R. A. Thermoelectric Power Factor Optimization in PEDOT:PSS Tellurium Nanowire Hybrid Composites. *Phys. Chem. Chem. Phys.* **2013**, *15* (11), 4024–4032. https://doi.org/10.1039/c3cp44558e.

(105) See, K. C.; Feser, J. P.; Chen, C. E.; Majumdar, A.; Urban, J. J.; Segalman, R. A. Water-Processable Polymer-Nanocrystal Hybrids for Thermoelectrics. *Nano Lett.* **2010**, *10* (11), 4664–4667. https://doi.org/10.1021/nl102880k.

(106) Faleev, S. V.; Léonard, F. Theory of Enhancement of Thermoelectric Properties of Materials with Nanoinclusions. *Phys. Rev. B - Condens. Matter Mater. Phys.* **2008**, *77* (21), 1–9. https://doi.org/10.1103/PhysRevB.77.214304.

(107) Narducci, D.; Selezneva, E.; Cerofolini, G.; Frabboni, S.; Ottaviani, G. Impact of Energy Filtering and Carrier Localization on the Thermoelectric Properties of Granular Semiconductors. *J. Solid State Chem.* **2012**, *193*, 19–25. https://doi.org/10.1016/j.jssc.2012.03.032.

(108) Zhang, Y.; Stucky, G. D. Heterostructured Approaches to Efficient Thermoelectric Materials. *Chem. Mater.* **2014**, *26* (1), 837–848. https://doi.org/10.1021/cm402150j.

(109) Ting, Z.; Li, K.; Li, C.; Ma, S.; Hng, H. H.; Lei, W. Mechanically Durable and Flexible Thermoelectric Films from PEDOT:PSS/PVA/$Bi_{0.5}Sb_{1.5}Te_3$ Nanocomposites. *Adv. Electron. Mater.* **2017**, *3* (4), 1–9. https://doi.org/10.1002/aelm.201600554.

(110) Zhang, Y.; Snedaker, M. L.; Birkel, C. S.; Mubeen, S.; Ji, X.; Shi, Y.; Liu, D.; Liu, X.; Moskovits, M.; Stucky, G. D. Silver-Based Intermetallic Heterostructures in Sb_2Te_3 Thick Films with Enhanced Thermoelectric Power Factors. *Nano Lett.* **2012**, *12* (2), 1075–1080. https://doi.org/10.1021/nl204346g.

(111) Gayner, C.; Amouyal, Y. Energy Filtering of Charge Carriers: Current Trends, Challenges,

and Prospects for Thermoelectric Materials. *Adv. Funct. Mater.* **2020**, *30* (18), 1–17. https://doi.org/10.1002/adfm.201901789.

(112) He, J.; Girard, S. N.; Kanatzidis, M. G.; Dravid, V. P. Microstructure-Lattice Thermal Conductivity Correlation in Nanostructured $PbTe_{0.7}S_{0.3}$ Thermoelectric Materials. *Adv. Funct. Mater.* **2010**, *20*, 764–772.

(113) Zhiming, L.; Mathias, J. B.; Kamal, B.; Douglas, R. S.; Kenneth, R. G. Increased Power Factors of Organic-Inorganic Nanocomposite Thermoelectric Materials and the Role of Energy Filtering. *J. Mater. Chem. A* **2017**, *5* (30), 15891.

(114) Bredas, J. L.; Street, G. B. Polarons, Bipolarons, and Solitons in Conducting Polymers. *Acc. Chem. Res.* **1985**, *18* (10), 309–315. https://doi.org/10.1021/ar00118a005.

(115) Dubey, N.; Leclerc, M. Conducting Polymers: Efficient Thermoelectric Materials. *J. Polym. Sci. Part B Polym. Phys.* **2011**, *49* (7), 467–475. https://doi.org/10.1002/polb.22206.

(116) Scaccabarozzi, A. D.; Basu, A.; Aniés, F.; Liu, J.; Zapata-Arteaga, O.; Warren, R.; Firdaus, Y.; Nugraha, M. I.; Lin, Y.; Campoy-Quiles, M.; Koch, N.; Müller, C.; Tsetseris, L.; Heeney, M.; Anthopoulos, T. D. Doping Approaches for Organic Semiconductors. *Chem. Rev.* **2022**, *122* (4), 4420–4492. https://doi.org/10.1021/acs.chemrev.1c00581.

(117) Neusser, D.; Malacrida, C.; Kern, M.; Gross, Y. M.; Van Slageren, J.; Ludwigs, S. High Conductivities of Disordered P3HT Films by an Electrochemical Doping Strategy. *Chem. Mater.* **2020**, *32* (14), 6003–6013. https://doi.org/10.1021/acs.chemmater.0c01293.

(118) Zhong, Y.; Untilova, V.; Muller, D.; Guchait, S.; Kiefer, C.; Herrmann, L.; Zimmermann, N.; Brosset, M.; Heiser, T.; Brinkmann, M. Preferential Location of Dopants in the Amorphous Phase of Oriented Regioregular Poly(3-Hexylthiophene-2,5-Diyl) Films Helps Reach Charge Conductivities of 3000 Scm^{-1}. *Adv. Funct. Mater.* **2022**, *32* (30). https://doi.org/10.1002/adfm.202202075.

(119) Untilova, V.; Hynynen, J.; Hofmann, A. I.; Scheunemann, D.; Zhang, Y.; Barlow, S.; Kemerink, M.; Marder, S. R.; Biniek, L.; Müller, C.; Brinkmann, M. High Thermoelectric Power Factor of Poly(3-Hexylthiophene) through In-Plane Alignment and Doping with a Molybdenum Dithiolene Complex. *Macromolecules* **2020**, *53* (15), 6314–6321. https://doi.org/10.1021/acs.macromol.0c01223.

(120) Bounioux, C.; Díaz-Chao, P.; Campoy-Quiles, M.; Martín-González, M.; Goni, A.; Yerushalmi-Rozen, R.; Müller, C. Thermoelectric Composites of Poly(3-Hexylthiophene) and Carbon

Nanotubes with a Large Power Factor. *Energy Environ. Sci.* **2013**, *6*, 918–925. https://doi.org/10.1039/c2ee23406h.

(121) Qin, Y.; Qun, W.; Liming, W.; Lidong, C. Environmental Science Abnormally Enhanced Thermoelectric Transport Properties of SWNT / PANI Hybrid Films by the Strengthened PANI Molecular Ordering. *Energy Environ. Sci.* **2014**, *7*, 3801–3807. https://doi.org/10.1039/c4ee01905a.

(122) Hong, C.T.; Lee, W.; Kang, Y.H.; Yoo, Y.; Ryu, J.; Cho, S. Y. .; Jang, K. S. . Effective Doping by Spin-Coating and Enhanced Thermoelectric Power Factors in SWCNT/P3HT Hybrid Films. *J. Mater. Chem. A* **2015**, *3* (23), 12314–12319.

(123) Yao, Q.; Chen, L.; Zhang, W.; Liufu, S.; Chen, X. Enhanced Thermoelectric Performance of Single-Walled Carbon Nanotubes/Polyaniline Hybrid Nanocomposites. *ACS Nano* **2010**, *4.4*, 2445–2451.

(124) Sainz, R.; Benito, A. M.; Martinez, M. T.; Galindo, J. F.; Sotres, J.; Baro, A. M.; Corraze, B.; Chauvet, O.; Maser, W. K. Soluble Self-Aligned Carbon Nanotube Polyaniline Composites. *Adv. Mater.* **2005**, *17*, 278–281. https://doi.org/10.1002/adma.200400921.

(125) Wang, Q.; Yao, Q.; Chang, J.; Chen, L. Enhanced Thermoelectric Properties of CNT/PANI Composite Nanofibers by Highly Orienting the Arrangement of Polymer Chains. *J. Mater. Chem.* **2012**, *22* (34), 17612–17618. https://doi.org/10.1039/c2jm32750c.

(126) Yao, Q.; Wang, Q,; Wang, L.; Wang, Y.; Sun, J.; Zeng, H.; Jin, Z.; Huang, X.; Chen. L. The Synergic Regulation of Conductivity and Seebeck Coefficient in Pure Polyaniline by Chemically Changing the Ordered Degree of Molecular Chains. *J. Mater. Chem. A* **2014**, *2* (207890), 2634–2640.

(127) Kang, S. D.; Snyder, G. J. Charge-Transport Model for Conducting Polymers. *Nat. Mater.* **2017**, *16* (2), 252–257.

(128) Kumar, P.; Zaia, E. W.; Yildirim, E.; Repaka, D. V. M.; Yang, S.-W.; Urban, J. J.; Kedar Hippalgaonkar. Polymer Morphology and Interfacial Charge Transfer Dominate over Energy-Dependent Scattering in Organic-Inorganic Thermoelectrics. *Nat. Commun.* **2018**, *9* (1), 1–10. https://doi.org/10.1038/s41467-018-07435-z.

(129) Bash, D.; Cai, Y.; Chellappan, V.; Wong, S. L.; Yang, X.; Kumar, P.; Tan, J. D.; Abutaha, A.; Cheng, J. J. W.; et. al. Multi-Fidelity High-Throughput Optimization of Electrical Conductivity in P3HT-CNT Composites. *Adv. Funct. Mater.* **2021**, *31*, 2102606.

(130) Han, G.; Popuri, S. R.; Greer, H. F.; Llin, L. F.; Bos, J. W. G.; Zhou, W.; Paul, D. J.; et al. Chlorine-Enabled Electron Doping in Solution-Synthesized SnSe Thermoelectric Nanomaterials. *Adv. Energy Mater.* **2017**, *7* (13), 1–7. https://doi.org/10.1002/aenm.201602328.

(131) Zhang, G.; Kirk, B.; Jauregui, L. A.; Yang, H.; Xu, X.; Chen, Y. P.; Wu, Y. Rational Synthesis of Ultrathin n-Type Bi_2Te_3 Nanowires with Enhanced Thermoelectric Properties. *Nano Lett.* **2012**, *12* (1), 56–60. https://doi.org/10.1021/nl202935k.

(132) Yang, T. H.; Shi, Y.; Janssen, A.; Xia, Y. Surface Capping Agents and Their Roles in Shape-Controlled Synthesis of Colloidal Metal Nanocrystals. *Angew. Chem. Int. Ed.* **2020**, *59*, 15378 –15401.

(133) Niu, Z.; Li, Y. Removal and Utilization of Capping Agents in Nanocatalysis. *Chem. Mater.* **2014**, *26* (1), 72–83. https://doi.org/10.1021/cm4022479.

(134) Sahu, A.; Russ, B.; Liu, M.; Yang, F.; Zaia, E.W.; Gordon, M.P.; Forster, J.D.; Zhang, Y.Q.; Scott, M.C.; Persson, K.A.; Coates, N.E. In-Situ Resonant Band Engineering of Solution-Processed Semiconductors Generates High Performance n-Type Thermoelectric Nano-Inks. *Nat. Commun.* **2020**, *11* (1).

(135) Jin, L.; Hao, Y.; Tareen, A. K.; Khan, K.; Wageh, S.; Al-Hartomy, O. A.; Al-Sehemi, A. G.; Zhang, H.; Zhang, Y. Tellurium/Polymers for Flexible Thermoelectrics: Status and Challenges. *J. Mater. Chem. A* **2023**, *11* (8), 3771–3788. https://doi.org/10.1039/d2ta09517c.

(136) Patterson, A. L. The Scherrer Formula for X-Ray Particle Size Determination. *Phys. Rev.* **1939**, *56* (10), 978–982. https://doi.org/10.1103/PhysRev.56.978.

(137) Shah, F. A.; Ruscsák, K.; Anders Palmquist. 50 Years of Scanning Electron Microscopy of Bone—a Comprehensive Overview of the Important Discoveries Made and Insights Gained Into Bone Material Properties in Health, Disease, and Taphonomy. *Bone Res.* **2019**, *7* (1), 1–15. https://doi.org/10.1038/s41413-019-0053-z.

(138) Watt, I. M. *The Principles and Practice of Electron Microscopy*, 2nd edition.; Cambridge University Press: Cambridge, **1997**.

(139) Goldstein, J. I.; Newbury, D. E.; Michael, J. R.; Ritchie, N. W.; Scott, J. H.; Joy, D. C. *Scanning Electron Microscopy and X-Ray Microanalysis*,4th edition.; Springer: New York, **2017**.

(140) Reimer, L. Scanning Electron Microscopy: Physics of Image Formation and Microanalysis.

Meas. Sci. Technol. **2000**, *11*, 1826–1826.

(141) Mokobi, F. *Transmission Electron Microscope (TEM)- Definition, Principle.* [online] https://microbenotes.com/transmission-electron-microscope-tem/ (accessed 2024 -09 -17).

(142) Burton, M. R. Soft-Templating of Nanostructured Materials for Thermoelectric Power Harvesting and Catalysis, *Doctoral dissertation*, University of Southampton **2017**.

(143) Nellist, P. D. *Scanning Transmission Electron Microscopy*; Springer Handbooks, **2019,** 49-99. https://doi.org/10.1007/978-3-030-00069-1_2.

(144) Simon, P.; Baldovino-Medrano, V. G.; Wojcieszak, R. X-Ray Photoelectron Spectroscopy (XPS): Principles and Application for the Analysis of Photoactive Materials. *Springer Handbook of Inorganic Photochemistry*; Cham: Springer International Publishing: Switzerland, **2022**; 249–271. https://doi.org/10.1007/978-3-030-63713-2_2.

(145) Pan, T.; Sun, L. Sub-Microscopic Phenomena of Metallic Corrosion Studied by a Combined Photoelectron Spectroscopy in Air (PESA) and Scanning Kelvin Probe Force Microscopy (SKPFM) Approach. *Int. J. Electrochem. Sci.* **2012**, *7* (10), 9325–9344. https://doi.org/10.1016/s1452-3981(23)16200-6.

(146) AC-2S Photoemission Yield Spectroscopy in Air. [online] https://www.rkiinstruments.com/product/ac-2s-photoemission-spectroscopy/.

(147) Nagashima, S.; Tsunekawa, T.; Shiroguchi, N.; Zenba, H.; Uda, M. Double Cylindrical Open Counter of Pocket Size. *Nucl. Instruments Methods Phys. Res. Sect. A Accel. Spectrometers, Detect. Assoc. Equip.* **1996**, *373* (1), 148–152. https://doi.org/10.1016/0168-9002(95)01491-8.

(148) Narchi, P. Investigation of Crystalline Silicon Solar Cells at the Nano-Scale Using Scanning Probe Microscopy Techniques, **2017**.

(149) Baikie, I. D.; Petermann, U.; Speakman, A.; Dirscherl, K. M.; Estrup, P. J. Work Function Study of Rhenium Oxidation Using an Ultra High Vacuum Scanning Kelvin Probe. *J. Appl. Phys.* **2000**, *4375*, 4371–4375.

(150) Akash, M. S. H.; Kanwal Rehman. *Essentials of Pharmaceutical Analysis*; Springer Nature Singapore Pte Ltd, **2020**. https://doi.org/https://doi.org/10.1007/978-981-15-1547-7.

(151) Rocha, F. S.; Gomes, A. J.; Lunardi, C. N.; Kaliaguine, S.; Patience, G. S. Experimental

Methods in Chemical Engineering Ultraviolet Visible Spectroscopy -UV-Vis. *Can. J. Chem. Eng.* **2018**, *96*, 2512–2517.

(152) Smits, F. M. Measurement of Sheet Resistivities with the Four-Point Probe. *Bell Syst. Tech. J.* **1958**, *37* (3), 711–718. https://doi.org/10.1002/j.1538-7305.1958.tb03883.x.

(153) Kumar, P.; Repaka, D.V.; Hippalgaonkar, K. Lithography-Free Resistance Thermometry Based Technique to Accurately Measure Seebeck Coefficient and Electrical Conductivity for Organic and Inorganic Thin Films. *Rev. Sci. Instrum.* **2017**, *88* (125112).

(154) Gripshover, R. J.; VanZytveld, J. B.; Bass, J. Thermopower of Pure Aluminium. *Phys. Rev.* **1967**, *163*, 598.

(155) Linseis, V.; Völklein, F.; Reith, H.; Nielsch, K.; Woias, P. Advanced Platform for the In-Plane ZT Measurement of Thin Films. *Rev. Sci. Instrum.* **2018**, *89* (1). https://doi.org/10.1063/1.5005807.

(156) Shah, S. Z. H.; Zhenyu, D.; Aabdin, Z.; Tjiu, W.W.; Recatala,G. J.; Dai, H.; Xiaoping, Y.; Maheswar, R. D. V.; Wu, G.; Kumar, P.; Hippalgaonkar, K.; Nandhakumar, I. Oxidation Control to Augment Interfacial Charge Transport in Te-P3HT Hybrid Materials for High Thermoelectric Performance. *Adv. Sci.* **2024**, 2400802.

(157) Kemp, N. T.; Kaiser, A. B.; Liu, C. J.; Chapman, B.; Mercier, O.; Carr, A. M.; Trodahl, H. J.; Buckley, R. G.; Partridge, A. C.; Lee, J. Y.; Kim, C. Y.; Bartl, A.; Dunsch, L.; Smith, W. T.; Shapiro, J. S. Thermoelectric Power and Conductivity of Different Types of Polypyrrole. *J. Polym. Sci. Part B Polym. Phys.* **1999**, *37* (9), 953–960.

(158) Ju, H.; Kim, J. Fabrication of Conductive Polymer/Inorganic Nanoparticles Composite Films: PEDOT:PSS with Exfoliated Tin Selenide Nanosheets for Polymer-Based Thermoelectric Devices. *Chem. Eng. J.* **2016**, *297*, 66–73. https://doi.org/10.1016/j.cej.2016.03.137.

(159) Ma, S.; Anderson, K.; Guo, L.; Yousuf, A.; Ellingsworth, E.C.; Vajner, C.; Wang, H.T.; Szulczewski, G. Temperature Dependent Thermopower and Electrical Conductivity of Te Nanowire/Poly(3,4-Ethylenedioxythiophene):Poly(4-Styrene Sulfonate) Microribbons. *Appl. Phys. Lett.* **2014**, *105* (7). https://doi.org/10.1063/1.4893740.

(160) Yusupov, K.; Vomiero, A. Polymer-Based Low-Temperature Thermoelectric Composites. *Adv. Funct. Mater.* **2020**, *30*, 2002015. https://doi.org/10.1002/adfm.202002015.

(161) Chatterjee, K.; Mitra, M.; Kargupta, K.; Ganguly, S.; Banerjee, D. Synthesis, Characterization and Enhanced Thermoelectric Performance of Structurally Ordered Cable-like Novel

Polyaniline-Bismuth Telluride Nanocomposite. *Nanotechnology* **2013**, *24* (21). https://doi.org/10.1088/0957-4484/24/21/215703.

(162) Zaia, E. W.; Sahu, A.; Zhou, P.; Gordon, M. P.; Forster, J. D.; Aloni, S.; Liu, Y. S.; Guo, J.; Urban, J. J. Carrier Scattering at Alloy Nanointerfaces Enhances Power Factor in PEDOT:PSS Hybrid Thermoelectrics. *Nano Lett.* **2016**, *16* (5), 3352–3359. https://doi.org/10.1021/acs.nanolett.6b01009.

(163) Hu, X.; Zhang, K.; Zhang, J.; Wang, S.; Qiu, Y. Thermoelectric Properties of Conducting Polymer Nanowire-Tellurium Nanowire Composites. *ACS Appl. Energy Mater.* **2018**, *1* (9), 4883–4890. https://doi.org/10.1021/acsaem.8b00909.

(164) Meng, Q.; Jiang, Q.; Cai, K.; Chen, L. Preparation and Thermoelectric Properties of PEDOT:PSS Coated Te Nanorod/PEDOT:PSS Composite Films. *Org. Electron.* **2019**, *64*, 79–85. https://doi.org/10.1016/j.orgel.2018.10.010.

(165) Karalis, G.; Tzounis, L.; Mytafides, C. K.; Tsirka, K.; Formanek, P.; Stylianakis, M.; Kymakis, E.; Paipetis, A. S. A High Performance Flexible and Robust Printed Thermoelectric Generator Based on Hybridized Te Nanowires with PEDOT:PSS. *Appl. Energy* **2021**, *294*, 117004. https://doi.org/10.1016/j.apenergy.2021.117004.

(166) Sahu, A.; Russ, B.; Su, N.C.; Forster, J.D.; Zhou, P.; Cho, E.S.; Ercius, P.; Coates, N.E.; Segalman, R.A.; Urban, J.J. Bottom-up Design of de Novo Thermoelectric Hybrid Materials Using Chalcogenide Resurfacing. *J. Mater. Chem. A* **2017**, *5* (7), 3346.

(167) Mitra, M., Kulsi, C., Kargupta, K., Ganguly, S., Banerjee, D. Composite of Polyaniline-bismuth Selenide with Enhanced Thermoelectric Performance. *Appl. Polym. Sci.* **2018**, *135(48)*, 46887. https://doi.org/10.1002/APP.46887.

(168) Choi, J.; Lee, J. Y.; Lee, S.-S.; Park, C. R.; Kim, H. High-Performance Thermoelectric Paper Based on Double Carrier-Filtering Processes. *Adv. Energy Mater.* **2016**, *6(9)* (1502181).

(169) Semaltianos, N. G.; Logothetidis, S.; Hastas, N.; Perrie, W.; Romani, S.; Potter, R. J.; Dearden, G.; Watkins, K. G.; French, P.; Sharp, M. Modification of the Electrical Properties of PEDOT:PSS by the Incorporation of ZnO Nanoparticles Synthesized by Laser Ablation. *Chem. Phys. Lett.* **2010**, *484* (4–6), 283–289. https://doi.org/10.1016/j.cplett.2009.11.054.

(170) Bubnova, O.; Crispin, X. Towards Polymer-Based Organic Thermoelectric Generators. *Energy Environ. Sci.* **2012**, *5* (11), 9345–9362. https://doi.org/10.1039/c2ee22777k.

(171) Zavabeti, A.; Patjaree Aukarasereenont, H. T.; Syed, N.; Jannat, A.; Elbourne, A.; Messalea,

K. A.; Zhang, B. Y.; Murdoch, B. J.; Partridge, J. G.; Wurdack, M.; Creedon, D. L.; Embden, J. van; Kourosh Kalantar-Zadeh, S. P. R.; McConville, C. F.; Daeneke, T. High-Mobility p-Type Semiconducting Two-Dimensional β-TeO_2. *Nat. Electron.* **2021**, *4* (4), 277–283.

(172) Liu, S.; Peng, N.; Bai, Y.; Ma, D.; Ma, F.; Xu, K. Self-Formation of Thickness Tunable Bi_2Te_3 Nanoplates on Thin Films with Enhanced Thermoelectric Performance. *RSC Adv.* **2016**, *6* (38), 31668–31674.

(173) Han, M.K.; Kim, S.; Kim, H.Y.; Kim, S.J. An alternative strategy to construct Interfaces in Bulk Thermoelectric Material: Nanostructured Heterophase Bi_2Te_3/Bi_2S_3. *RSC Adv.* **2013**, *3* (14), 4673–4679.

(174) Bhopale, S. R.; More, M. A. Systematic Field Electron Emission Investigations of Vapor-Phase-Grown Sb_2Te_3 Nanosheets. *Phys. Status Solidi Appl. Mater. Sci.* **2022**, *219* (18). https://doi.org/10.1002/pssa.202200126.

(175) Chen, G.; Shakouri, A. Heat Transfer in Nanostructures for Solid-State Energy Conversion. *J. Heat Transfer* **2002**, *124* (2), 242–252. https://doi.org/10.1115/1.1448331.

(176) Gelbstein, Y. Thermoelectric Power and Structural Properties in Two-Phase Sn/SnTe Alloys. *J. Appl. Phys.* **2009**, *105* (2). https://doi.org/10.1063/1.3068463.

(177) Shah, S. Z. H.; Aabdin, Z.; Tjiu, W. W.; Nong, W.; Recatala-Gomez, J.; Chellappan, V.; Zhai, W.; Repaka, D. V. M.; Wu, G.; Hippalgaonkar, K.; Nandhakumar, I.; Kumar, P. Thermoelectric Property Enhancement of Tellurium Nanowires by Surface Passivation. *ACS Appl. Mater. Interfaces* **2024**, *16* (35), 46191–46199. https://doi.org/10.1021/acsami.4c02469.

(178) Ansar, S. M.; Ameer, F. S.; Hu, W.; Zou, S.; Pittman, C. U.; Zhang, D. Removal of Molecular Adsorbates on Gold Nanoparticles Using Sodium Borohydride in Water. *Nano Lett.* **2013**, *13* (3), 1226–1229. https://doi.org/10.1021/nl304703w.

(179) Luo, M.; Hong, Y.; YAO, W.; Huang, C.; Xu, Q.; Wu, Q. Facile Removal of Polyvinylpyrrolidone (PVP) Adsorbates from Pt Alloy Nanoparticles. *J. Mater. Chem. A* **2013**, *1*, 7584–7591.

(180) Amato, M.; Rurali, R. Surface Physics of Semiconducting Nanowires. *Prog. Surf. Sci.* **2016**, *91* (1), 1–28. https://doi.org/10.1016/j.progsurf.2015.11.001.

(181) Nicollian, E. H. Surface Passivation of Semiconductors. *J. Vac. Sci. Technol.* **1971**, *8* (5), 39–49. https://doi.org/10.1116/1.1316388.

(182) Thongkham, W.; Lertsatitthanakorn, C.; Jiramitmongkon, K.; Tantisantisom, K.; Boonkoom, T.; Jitpukdee, M.; Sinthiptharakoon, K.; Klamchuen, A.; Liangruksa, M.; Khanchaitit, P. Self-Assembled Three-Dimensional Bi_2Te_3 Nanowire - PEDOT:PSS Hybrid Nano Film Network for Ubiquitous Thermoelectrics. *ACS Appl. Mater. Interfaces* **2019**, *11*, 6624–6633. https://doi.org/10.1021/acsami.8b19767.

(183) Volker, S.; V., W. J.; Stephan, S.; Ulrich, G. Silicon Nanowires: A Review on Aspects of Their Growth and Their Electrical Properties. *Adv. Mater.* **2009**, *21* (25–26), 2681–2702. https://doi.org/10.1002/adma.200803754.

(184) Fukuroi, T.; Tanuma, S.; Tobisawa, S. Electrical Properties of Antimony-Doped Tellurium Crystals. *Sci. Rep. Res. Inst. Ser. A.* **1952**, *4*, 283–297.

(185) Zhang, B.; Sun, J.; Katz, H. E.; Fang, F.; Opila, R. L. Promising Thermoelectric Properties of Commercial PEDOT:PSS Materials and Their Bi_2Te_3 Powder Composites. *ACS Appl. Mater. Interfaces* **2010**, *2* (11), 3170–3178.

(186) Yong, D.; K. F., C.; Song, C.; Pavel, C.; Tong, L. Facile Preparation and Thermoelectric Properties of Bi_2Te_3 Based Alloy Nanosheet/PEDOT:PSS Composite Films. *ACS Appl. Mater. Interfaces* **2014**, *6* (8), 5735.

(187) Zhang, B.; Sun, J.; Katz, H. E.; Fang, F.; Opila, R. L. Promising Thermoelectric Properties of Commercial PEDOT:PSS Materials and Their Bi_2Te_3 Powder Composites. *ACS Appl. Mater. Interfaces* **2010**, *2* (11), 3170–3178. https://doi.org/10.1021/am100654p.

(188) Chen, Y.; He, M.; Liu, B.; Bazan, G. C.; Zhou, J.; Liang, Z. Bendable n-Type Metallic Nanocomposites with Large Thermoelectric Power Factor. *Adv. Mater.* **2017**, *29* (4). https://doi.org/10.1002/adma.201604752.

(189) Liu, C.; Jiang, F.; Huang, M.; Lu, B.; Yue, R.; Xu, J. Free-Standing PEDOT-PSS/$Ca_3Co_4O_9$ Composite Films as Novel Thermoelectric Materials. *J. Electron. Mater.* **2011**, *40* (5), 948–952. https://doi.org/10.1007/s11664-010-1465-0.

(190) Zaia, E. W.; Gordon, M. P.; Yuan, P.; Urban, J. J. Progress and Perspective: Soft Thermoelectric Materials for Wearable and Internet-of-Things Applications. *Adv. Electron. Mater.* **2019**, *5* (11), 1–20. https://doi.org/10.1002/aelm.201800823.

(191) Patidar, D.; Saxena, N. S. Influence of CdS Nano Additives on the Thermal Conductivity of Poly(Vinyl Chloride)/CdS Nanocomposites. *Adv. Nanoparticles* **2013**, *02* (01), 11–15. https://doi.org/10.4236/anp.2013.21003.

(192) Zaia, E. W.; Gordon, M. P.; Niemann, V.; Choi, J.; Chatterjee, R.; Hsu, C.-H.; Yano, J.; Russ, B.; Sahu, A.; Urban, J. J. Molecular Level Insight into Enhanced N-Type Transport in Solution-Printed Hybrid Thermoelectrics. *Adv. Energy Mater.* **2019**, *9*, 1803469.

(193) Gordon, M. P.; Haas, K.; Zaia, E.; Menon, A. K.; Yang, L.; Bruefach, A.; Galluzzo, M. D.; Scott, M. C.; Prasher, R. S.; Sahu, A.; Urban, J. J. Understanding Diameter and Length Effects in a Solution-Processable Tellurium-Pedot-Pss Hybrid. *Adv. Electron. Mater.* **2021**, *7* (3), 2000904.

(194) We, J. H.; Kim, S. J.; Cho, B. J. Hybrid Composite of Screen-Printed Inorganic Thermoelectric Film and Organic Conducting Polymer for Flexible Thermoelectric Power Generator. *Energy* **2014**, *73*, 506–512. https://doi.org/10.1016/j.energy.2014.06.047.

(195) Lu, Y.; Ding, Y.; Qiu, Y.; Cai, K.; Yao, Q.; Song, H.; Tong, L.; He, J.; Chen, L. Good Performance and Flexible PEDOT : PSS / Cu_2Se Nanowire Thermoelectric Composite Films. *ACS Appl. Mater. Interfaces* **2019**, *11*, 12819-29. https://doi.org/10.1021/acsami.9b01718.

(196) Xiong, J.; Wang, L.; Xu, J.; Liu, C.; Zhou, W.; Shi, H.; Jiang, Q.; Jiang, F. Thermoelectric Performance of PEDOT:PSS/Bi_2Te_3-Nanowires: A Comparison of Hybrid Types. *J. Mater. Sci. Mater. Electron.* **2016**, *27* (2), 1769–1776. https://doi.org/10.1007/s10854-015-3952-9.

(197) Yoon, S. E.; Kim, B.; Chun, S. Y.; Lee, S. Y.; Jeon, D.; Kim, M.; Lee, S.; Seo, B. E.; Choi, K. S.; Kim, F. S.; Kim, T.; Seo, H.; Kwak, K.; Kim, J. H.; Kim, B. S. Impact of Molecular Weight on Molecular Doping Efficiency of Conjugated Polymers and Resulting Thermoelectric Performances. *Adv. Funct. Mater.* **2022**, *32* (32), 1–13. https://doi.org/10.1002/adfm.202202929.

(198) Mardi, S.; Pea, M.; Notargiacomo, A.; Nia, N. Y.; Di Carlo, A.; Reale, A. The Molecular Weight Dependence of Thermoelectric Properties of P3HT. *Materials (Basel).* **2020**, *13*, 1–10.

(199) Qu, S.; Yao, Q.; Yu, B.; Zeng, K.; Shi, W.; Chen, Y.; Chen, L. Optimizing the Thermoelectric Performance of Poly 3-hexylthiophene through Molecular Weight Engineering. *Chem. Asian J.* **2018**, *13*, 3246–53.

(200) Wang, L.; Liu, Y.; Zhang, Z.; Wang, B.; Qiu, J.; Hui, D.; Wang, S. Polymer Composites-Based Thermoelectric Materials and Devices. *Compos. Part B Eng.* **2017**, *122*, 145–155. https://doi.org/10.1016/j.compositesb.2017.04.019.

(201) Liu, S.; Peng, N.; Bai, Y.; Ma, D.; Ma, F.; Xu, K. Self-Formation of Thickness Tunable Bi_2Te_3

Nanoplates on Thin Films with Enhanced Thermoelectric Performance. *RSC Adv.* **2016**, *6* (38), 31668–31674. https://doi.org/10.1039/c5ra26835d.

(202) Han, M. K.; Kim, S.; Kim, H. Y.; Kim, S. J. An Alternative Strategy to Construct Interfaces in Bulk Thermoelectric Material: Nanostructured Heterophase Bi_2Te_3/Bi_2S_3. *RSC Adv.* **2013**, *3* (14), 4673–4679. https://doi.org/10.1039/c3ra23197f.

(203) Degousée, T.; Untilova, V.; Vijayakumar, V.; Xu, X.; Sun, Y.; Palma, M.; Brinkmann, M.; Biniek, L.; Fenwick, O. High Thermal Conductivity States and Enhanced Figure of Merit in Aligned Polymer Thermoelectric Materials. *J. Mater. Chem. A* **2021**, *9* (29), 16065–16075. https://doi.org/10.1039/x0xx00000x.